Strojniški vestnik

Journal of Mechanical Engineering

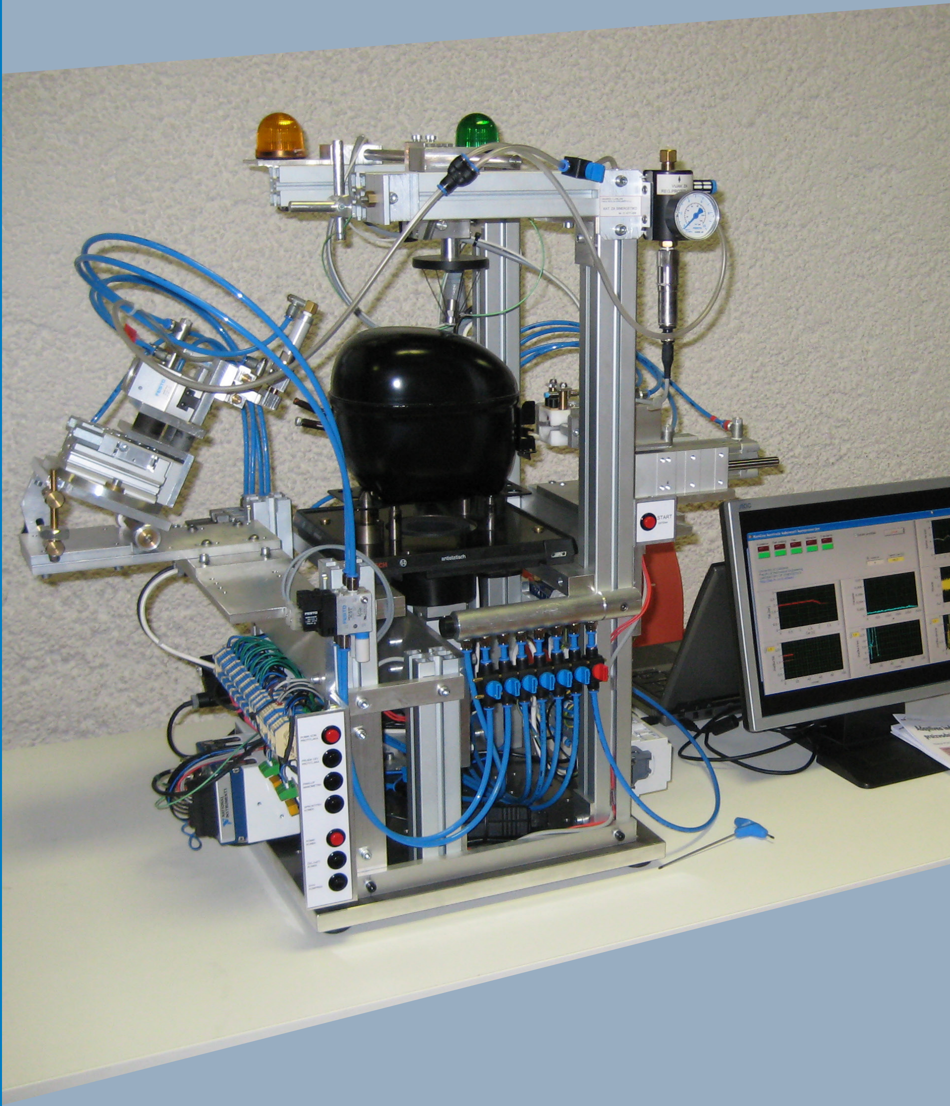

no. 5
year 2017
volume 63

Strojniški vestnik – Journal of Mechanical Engineering (SV-JME)

Aim and Scope

The international journal publishes original and (mini)review articles covering the concepts of materials science, mechanics, kinematics, thermodynamics, energy and environment, mechatronics and robotics, fluid mechanics, tribology, cybernetics, industrial engineering and structural analysis.

The journal follows new trends and progress proven practice in the mechanical engineering and also in the closely related sciences as are electrical, civil and process engineering, medicine, microbiology, ecology, agriculture, transport systems, aviation, and others, thus creating a unique forum for interdisciplinary or multidisciplinary dialogue.

The international conferences selected papers are welcome for publishing as a special issue of SV-JME with invited co-editor(s).

Editor in Chief
Vincenc Butala
University of Ljubljana, Faculty of Mechanical Engineering, Slovenia

Technical Editor
Pika Škraba
University of Ljubljana, Faculty of Mechanical Engineering, Slovenia

Founding Editor
Bojan Kraut
University of Ljubljana, Faculty of Mechanical Engineering, Slovenia

Editorial Office
University of Ljubljana, Faculty of Mechanical Engineering
SV-JME, Aškerčeva 6, SI-1000 Ljubljana, Slovenia
Phone: 386 (0)1 4771 137
Fax: 386 (0)1 2518 567
info@sv-jme.eu, http://www.sv-jme.eu

Print: Papirografika Bori, printed in 300 copies

Founders and Publishers
University of Ljubljana, Faculty of Mechanical Engineering, Slovenia
University of Maribor, Faculty of Mechanical Engineering, Slovenia
Association of Mechanical Engineers of Slovenia
Chamber of Commerce and Industry of Slovenia, Metal Processing Industry Association

President of Publishing Council
Branko Širok
University of Ljubljana, Faculty of Mechanical Engineering, Slovenia

Vice-President of Publishing Council
Jože Balič
University of Maribor, Faculty of Mechanical Engineering, Slovenia

Cover:
The cover shows demo version of the mechatronic system for vibration-based diagnostic of compressors. The system was developed in Laboratory of Synergetics in cooperation with Danfoss Compressors company in order to improve the final quality control of manufactured compressors.

Image Courtesy:
Laboratory of Synergetics
University of Ljubljana
Fakulty of Mechanical Engineering
http://lab.fs.uni-lj.si/lasin/

ISSN 0039-2480

General information

Strojniški vestnik – Journal of Mechanical Engineering is published in 11 issues per year (July and August is a double issue).

Institutional prices include print & online access: institutional subscription price and foreign subscription €100,00 (the price of a single issue is €10,00); general public subscription and student subscription €50,00 (the price of a single issue is €5,00). Prices are exclusive of tax. Delivery is included in the price. The recipient is responsible for paying any import duties or taxes. Legal title passes to the customer on dispatch by our distributor.

Single issues from current and recent volumes are available at the current single-issue price. To order the journal, please complete the form on our website. For submissions, subscriptions and all other information please visit: *http://en.sv-jme.eu/*.

You can advertise on the inner and outer side of the back cover of the journal. The authors of the published papers are invited to send photos or pictures with short explanation for cover content.

We would like to thank the reviewers who have taken part in the peer-review process.

SV-JME is indexed / abstracted in: SCI-Expanded, Compendex, Inspec, ProQuest-CSA, SCOPUS, TEMA. The list of the remaining bases, in which SV-JME is indexed, is available on the website.

The journal is subsidized by Slovenian Research Agency.

Strojniški vestnik - Journal of Mechanical Engineering is available on http://www.sv-jme.eu, where you access also to papers' supplements, such as simulations, etc.

Contents

Strojniški vestnik - Journal of Mechanical Engineering
volume 63, (2017), number 5
Ljubljana, May 2017
ISSN 0039-2480

Published monthly

Papers

Strojniški vestnik - Journal of Mechanical Engineering 63(2017)5, 287-299

DOI:10.5545/sv-jme.2016.4188
Original Scientific Paper
Received for review: 2016-11-13
Received revised form: 2017-01-22
Accepted for publication: 2017-02-20

Critical Failure Analysis of Superheater Tubes of Coal-Based Boiler

Gagan Kumar Gupta* – Somnath Chattopadhyaya
[1] Indian Institute of Technology (Indian School of Mines), Department of Mechanical Engineering, India

This paper highlights a methodology for failure investigation of superheater tubes made of the material T-22 of a coal-based boiler. The process includes visual observation, the identification of sampling locations, the determination of the bulk chemical composition of the base alloy, microstructural investigation using optical microscopy, the exploration of finer structural details using a scanning electron microscope (SEM), the evaluation of hardness over samples obtained from different locations, the fractographic analysis of different failed locations, the X-ray diffraction (XRD) study of corrosion products adhered to inner surfaces, and the determination of the nature of the failure. Within a span of four months, three successive failures of superheater tubes were reported. The tubes were observed to have undergone significant wall thinning. Microscopic examinations using SEM on the failed region and a region some distance away on the as-received tubes were conducted in order to determine the failure mechanism. Layer-wise oxidation corrosion (exfoliation) in the inner surface was observed. Apart from major cracking, a number of nearly straight line crackings were observed in the longitudinal direction of both tubes. Close to cracking/bulging, void formation/de-cohesion of grain boundary indicated creep deformation under service exploitation. The failure mechanism was identified to be a result of excessive oxidation corrosion along the inside wall to reduce thickness, the spheroidization of alloy carbides and the coarsening of precipitate as well as creep void formation along grain boundary leading to inter-granular cracking with material flow near regions covered with thick scales. Moreover, there was a drastic reduction in bulk hardness of alloy and finally 'thin lip fish mouth' fractures.

Keywords: coal based boiler, corrosion, creep, fractographic analysis, SEM, superheater tube

Highlights
- *Bulk chemical composition of base alloy has been determined.*
- *Optical microscopy has been applied for microstructural investigation.*
- *Details of finer structural have been explored by applying scanning electron microscope (SEM).*
- *Hardness of samples obtained from different locations of failed tubes has been evaluated.*
- *Fractographic & X-ray diffraction XRD analysis has been performed at different failure locations.*
- *Nature/type of failure to highlight the cause of failure ae has been examined.*

0 INTRODUCTION

A boiler is a vital element in power plants with regards to running cost and performance. A boiler generates steam via the optimized combustion of fuels (coal, gas & oil, etc.). It consists of several components of rotary equipment and pressure parts. The efficient and trouble-free operation of a boiler is difficult to maintain because the characteristics of input fuel vary over time. Deteriorated performance and repetitive failures of pressure parts of boiler is a very common issue. One of the critical components of pressure parts is the superheater, the failure of which leads to the forced outage of the working of a boiler, resulting in huge losses. A superheater is basically a heat exchanger in which heat is transferred from furnace gas to steam. Improper heat transfer between steam and furnace gas creates problems of localized heating. Uneven heat transfer is a result of non-uniform gas flow or non-uniform steam distribution in the superheater. Significant causes of failure in superheaters are localized prolonged heating, creep damage, thermal fatigue, excessive thermal stresses, water and fireside corrosion, erosion, etc. General modes of failures observed in superheaters are wall thinning, reduced thickness, fish-mouth opening type bursting, creep cracks on tube surfaces and puncturing. Tube failure in the superheater is sufficiently hazardous to lead to the forced evacuation of the whole plant. Therefore, it is important to take remedial actions to prevent technical as well as economic losses. It is highly necessary not only to critically identify areas of failures but also to critically determine the root cause of failures. Prolonged localized heating, which is considered a root cause of tube failures, is a result of improper operating procedures. Concentrated gas flow pattern over superheater and non-uniform steam distribution overheats localized portions of tubes. Proper distribution of furnace gas among the entire superheater tubes and uniform steam flow in each tube are advocated for the trouble-free operation of superheaters. A pictorial view of a boiler is presented in Fig. 1 with location of superheater. Dennies [1], Wulpi [2] and Brooks and Choudhury [3] has presented

---

*Corr. Author's Address: Indian Institute of Technology (Indian School of Mines), Department of Mechanical Engineering, India, gagan_k_gupta@rediffmail.com

guidelines and methods of failure analysis. Graham [4] and Ryder et al. [5] have described strategies and general practices for conducting failure analysis. Vander Voort [6] has presented failure analysis practices. Port and Herro [7] have suggested a reference guide for boiler failure analysis. Approximately 35 % of common failures in boilers are caused by long term overheating (creep) in superheater, reheaters, and wall tubes as per Rahmana et al. [8] and Xu et al. [9]. Manufacturing properties of materials and surface roughness have also been described as factors influencing the running conditions as per Krolczyk et al. [10] and Nieslony et al. [11]. Krolczyk and Legutko [12] have described the experimental analysis of surface roughness of duplex stainless steel. Jones [13] also reported the failure of four internally pressurized tubes involving a superheater that was failed by creep. Srikanth et al. [14] reported of failures of boiler tubes due to fireside corrosion in a waste heat recovery boiler utilizing exhaust gas. High corrosion propensity and consequent failures in the low-temperature sections of the boiler were found to be directly related to the formation of hydrated ferric sulphate in these regions. Chaudhuri [15] analysed tube failure and concluded that the failure takes place due to short-term overheating in the final superheater tubes. It is also reported that the non-failed re-heater tubes exhibit higher tensile properties than that of platen superheater tubes. Ranjbar [16] analysed the tube failure by chemical analysis of boiler cold and hot re-heater tubes. It was concluded that the improper maintenance and feed water quality/chemistry are the main causes of such failures. These observations have led to the development of various types of corrosion mechanisms.

Ahmad et al. [17] established excessive hoop stresses to be the cause of failure in a super alloy Inconel-800 superheater tube. The possibility of creep damage was checked using Larson-Miller parameter related to primary superheater tubes of a power plant by Ahmad et al. [18].Begum et al. [19] made an analysis of end crack in boiler tube. Rao and Sankara Narayanan [20] and Hanke [21] investigated causes of failure in boiler bank tubes and water wall tubes, respectively. Abbasfard et al. [22] also made a case study of failed superheater tubes of a waste heat boiler. Othman et al. [23] and Purbolaksono [24] have identified the failure of superheater tubes by performing finite element method (FEM) and by using an empirical formula in addition to visual inspections and metallurgical examinations. Botha and Hindley [25] have described the modelling methodology for boiler tube failure. Ahmad et al. [26] discussed the failure investigation of the rear water wall tube of a boiler using a method of calculating the hoop stress. It must be kept in mind that a failure of a tube is generally a sign of another problem, and it needs complete evaluations and investigations. Begum et al. [27] also conducted analysis to find failed boiler tube due to creep damage and optimization of operating conditions.

Kumarand Sapra [28] and Luo and Zhang [29] discussed the leakage failure analysis of boiler tubes in a power plant. Hasseand Hanke [30] concentrated on the analysis of economiser tube failure. Šeruga et al. [31] and Saha and Shukla [32] have developed a particular methodology for the investigation of

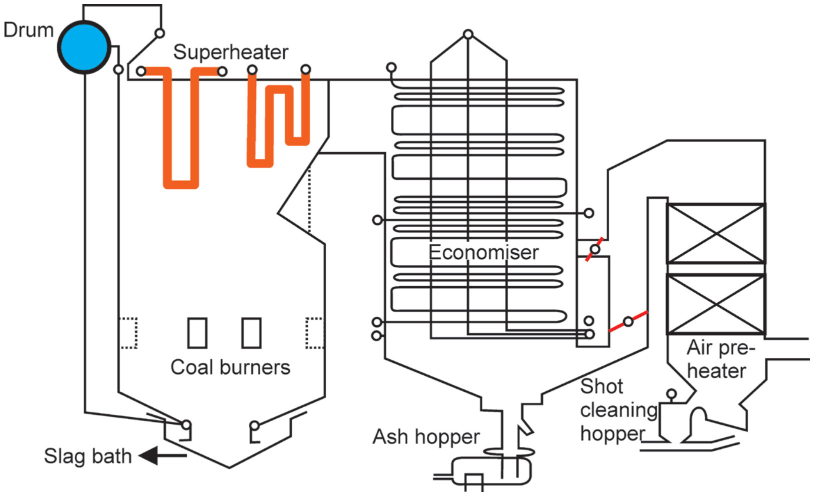

Fig. 1. *Typical Boiler (OPG 260 TPH) in which failure of superheater tubes observed*

failed superheater tube subjected to either long service life or short service life by using modelling and several failure analysis methods. Shokouhmand [33] has described the failure analysis retrofitting of superheater tubes in utility boilers. Movahedi-Rad et al. [34] and Saha et al. [35] have described the failure analysis of superheater tubes. The failure analysis of boiler tubes and boiler re-heater tubes due to fatigue has also been conducted by Hu et al. [36]. Javidi et al. [37] has described the failure analysis of steel piping in a power plant. Liang et al. [38] has employed SEM and EDS for investigating overheating of the final super-heater in a 660 MW power plant. Bettge et al. [39] has investigated the breakdown of a heat recovery steam generator during the initial operation run. Duda et al. [40] has measured hardness and tube thickness for a study of failed superheater tubes.

The present study has developed a generalized methodology for investigation of failed superheater tubes by considering feasible influential factors with suggestions for remedial actions. The tube material of the superheater in the present investigation was Cr-Mo low alloy steel of polish specification 'Steel 10H2M' with the intended operating temperature of 540 °C, applied continuously with steam pressure around 88 bar. The present methodology was applied on failed superheater tubes of boiler of Bokaro Power Supply Co. Ltd (A Joint Venture Company of SAIL & DVC), Bokaro (India). This boiler was commissioned in 1988 and last overhauled in December 2014. The

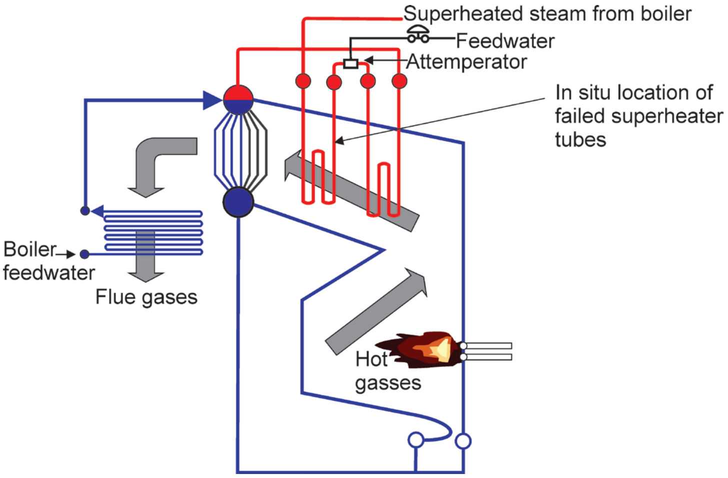

Fig.2. *Arrangement of superheater tube with frequent failure zone in one panel*

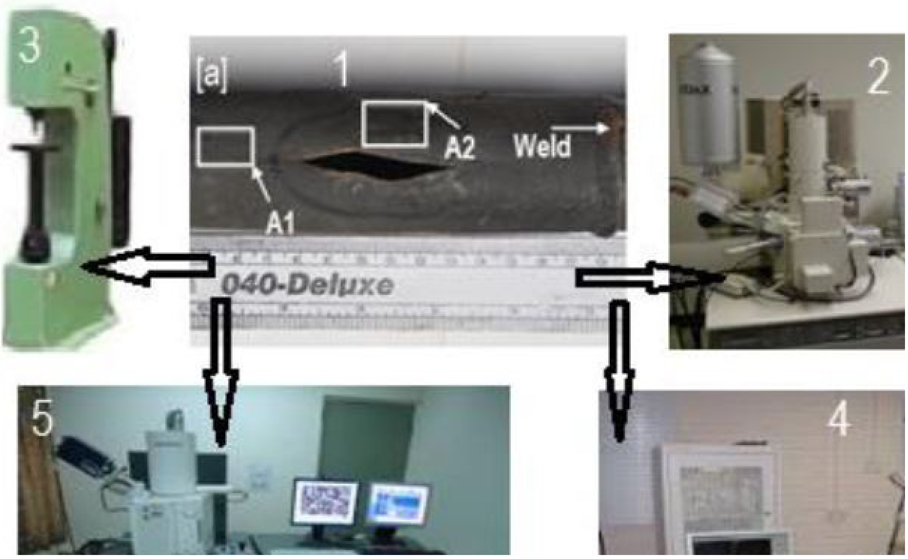

Fig. 3. *Setup for methodology (1) collection of tubes, (2) EDS analysis, (3) hardness measurement, (4) SEM, (5) XRD analysis*

first failure of a superheater tube occurred on 2 April 2015. Subsequently, a second failure was reported on 12 April 2015, and third one took place in May to June 2015.

1 DESCRIPTION OF SUPERHEATER

The superheater is located in the radiation zone of a boiler where heat is transferred from flue gas to dry steam, flowing into superheater tubes. The temperature of flue gas in this zone is around 700 °C and the temperature of steam coming out of the superheater tubes (final superheated steam) is around 540 ± 5 °C. Fig. 2 shows one panel of superheater tubes, and several numbers of such panels are arranged parallelly inside the boiler. It shows how the hot gases (flue gases) move inside the boiler. The superheater tubes are of varying thickness and material compositions with uniform outer diameters of Ø 38 mm.

2 SUMMARIES OF FAILURES AND GENERALIZED METHODOLOGY

The failed boiler tubes were made of Cr-Mo low alloy steel of polish specification ‘Steel 10H2M’. The outer diameter of tube was Ø 38 mm and thickness was 5.6 mm. As per the onsite condition, some tubes were found punctured and some were deformed. Considering all aspects of operational and influential parameters, a generalized methodology was developed, which is illustrated as a graphical set up in Fig. 3 and as a flow diagram consisting of steps for testing of failed tubes in Fig. 4.

3 EXPERIMENT RESULTS AND DISCUSSION

The broken boiler tubes were visually observed to reveal the nature of the fracture. The tube was cut along the cross- section to examine the appearance of the inner wall after the incident of fracture. Samples were collected from different locations for investigation and the nomenclature is given in Table 1.

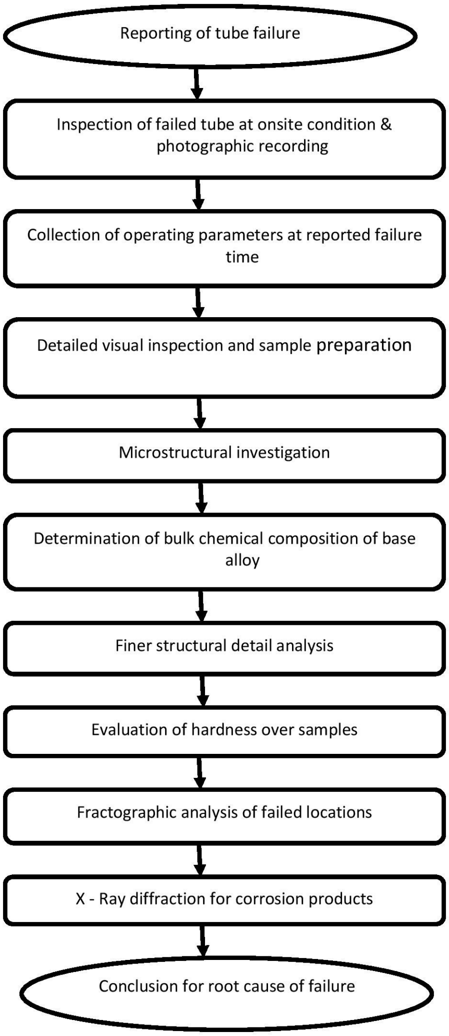

Fig. 4. *Generalized methodology for failure analysis of tube*

Table 1. *Sampling location from fracture component and its nomenclature*

Tube ID	Sample ID	Location
Sample-A (P-14_T-6)	Sample-A1	Away from fracture
	Sample-A2	Sub-surface of fracture
	Sample-A3	Near bulging
	Sample-A4	Near Fracture (Across thickness)
Sample-B (P-14_T-5)	Sample-B1	Away from fracture
	Sample-B2	Sub-surface of fracture
	Sample-B3	Near Fracture (Across thickness)

Samples A1 to A4 and B1 to B3 were considered for metallographic examination. They were mounted and polished with a conventional technique, etched with 3 % Nital and examined by optical (Leica) and scanning electron (JEOL JSM 840A) microscopes. Fractured surfaces (near A2 and B2) were cleaned using dilute EDTA solution followed by kerosene oil and finally by ultrasonic cleaning with acetone. The samples were studied with SEM. Bulk composition of alloy was determined in inductive coupled plasma (ICP) and LECO using chips, obtained from cleaned surfaces. The chemical composition for major alloying elements was also examined by using energy dispersive spectroscopy to re-confirm the result of wet chemical analysis. Bulk hardness was evaluated near fracture and bulging zone in Brinell scale using steel ball as indenter. Certain amounts of adhered corrosion products were collected and examined with an X-ray diffraction technique to identify their nature. The investigation and corresponding inferences are described in the following sub-sections.

3.1 Visual Examination

Failed tubes were observed in reflected light with naked eyes (Figs. 5 and 6). Two tubes were designated as Sample-A (P-14_T-6) and Sample-B (P-14_T-5). Both tubes were supposed to have been exposed to temperatures of 540 °C with stress level at 100 bar during operation. Sample-A exhibited fish mouth cracking on one side (Fig. 5a) and bulging at the opposite side of the weld (Fig. 5b). The cut length of the tube was ~400 mm, and the wall thickness of non-deformed region was ~5.80 mm with ~36.8 mm outer diameter. From the weld seam, the distance of cracking was ~40 mm and the total crack length was ~50 mm with ~6.7 mm maximum opening. Layer-wise corrosion was observed near the open end of the crack, and the remaining wall thickness was reduced drastically (≤ 1 mm). Inner surface consisted of multiple crack formations along the longitudinal direction (Fig. 5c). However, crack formation was completely absent on the outer surface. The latter was blackened owing to thermal effect (Fig. 5a) and the inside surface was deep brown with numerous reddish spots (Fig. 5c). As pointed out already, bulging was observed on the lower half of the same tube. After bulging, the outer diameter became ~42.0 mm with the distance of deformation at ~12 cm from the weld

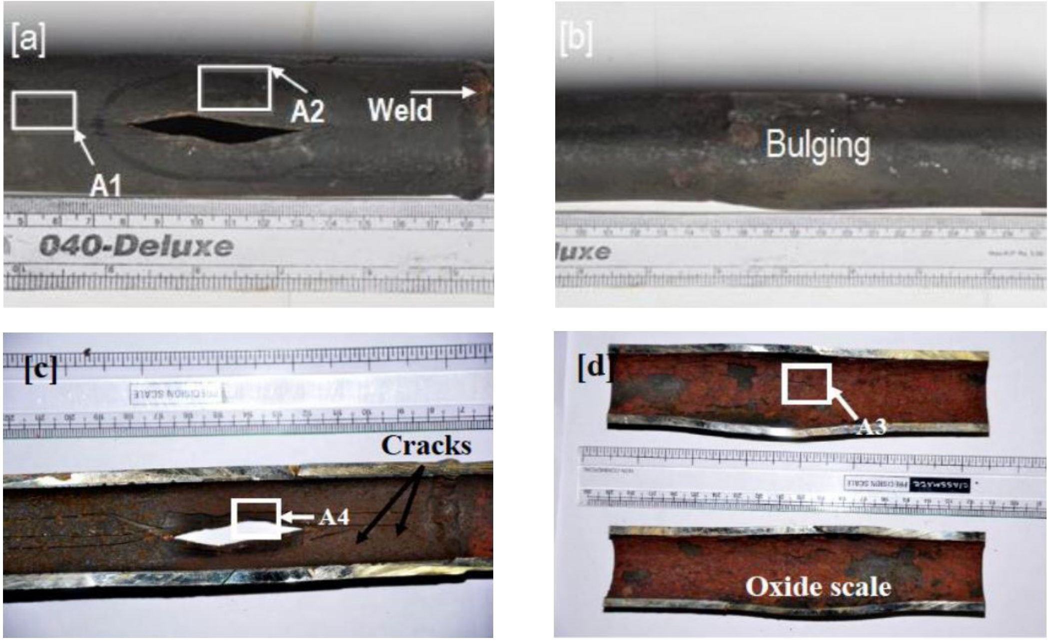

Fig. 5. *Macro image and sampling location from damaged tube A: a) cracking over surface, b) bulged region, c) inner surface of tube, and d) inner surface of bulged region*

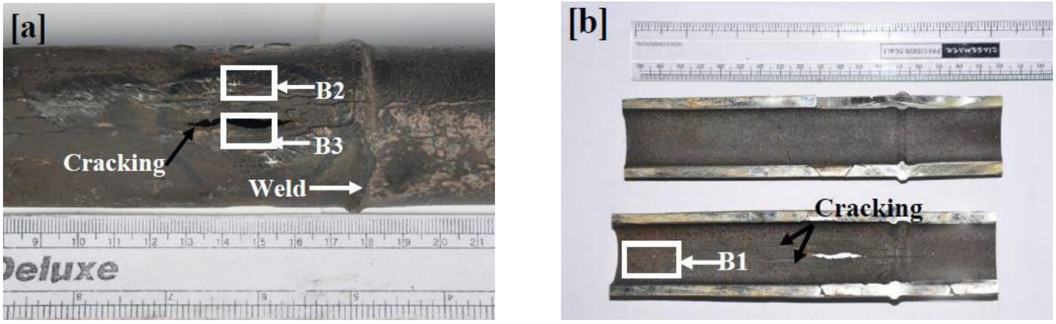

Fig. 6. *Macro image and sampling location from damaged tube B: a) cracking over surface, and b) appearance of inner surface*

Table 2. *Bulk chemical composition of component*

Alloy	Element in wt%								
	C	Si	Mn	Cr	Mo	S (max)	P (max)	Fe	Ni /Cu (max)
Steel 10H2M	0.08 to 0.15	0.15 to 0.30	0.3 to 0.6	2.0 to 2.5	0.9 to 1.1	0.30	0.30	bal	0.30
Din 10CrMo9-10	0.08 to 0.14	0.5 max	0.4 to 0.8	2.0 to 2.5	0.9 to 1.1	0.01	0.02	bal	0.30
T22	0.05 to 0.15	0.5 max	0.3 to 0.6	1.9 to 2.6	0.87 to 1.13	0.025	0.025	bal	NI
EDS analysis of sample A	NA	0.27	0.41	2.25	0.99	NA	NA	bal	N/F
ICP + LECO analysis of A	0.093	0.39	0.53	2.25	0.95	0.006	0.011	bal	0.05 / 0.016
EDS analysis of sample B	NA	0.32	0.47	2.10	1.03	NA	NA	bal	N/F
ICP + LECO analysis of B	0.108	0.39	0.54	2.26	0.95	0.006	0.011	bal	0.05 /0.017

*NA – Not analysed, N/F – not found, NI- not indicated

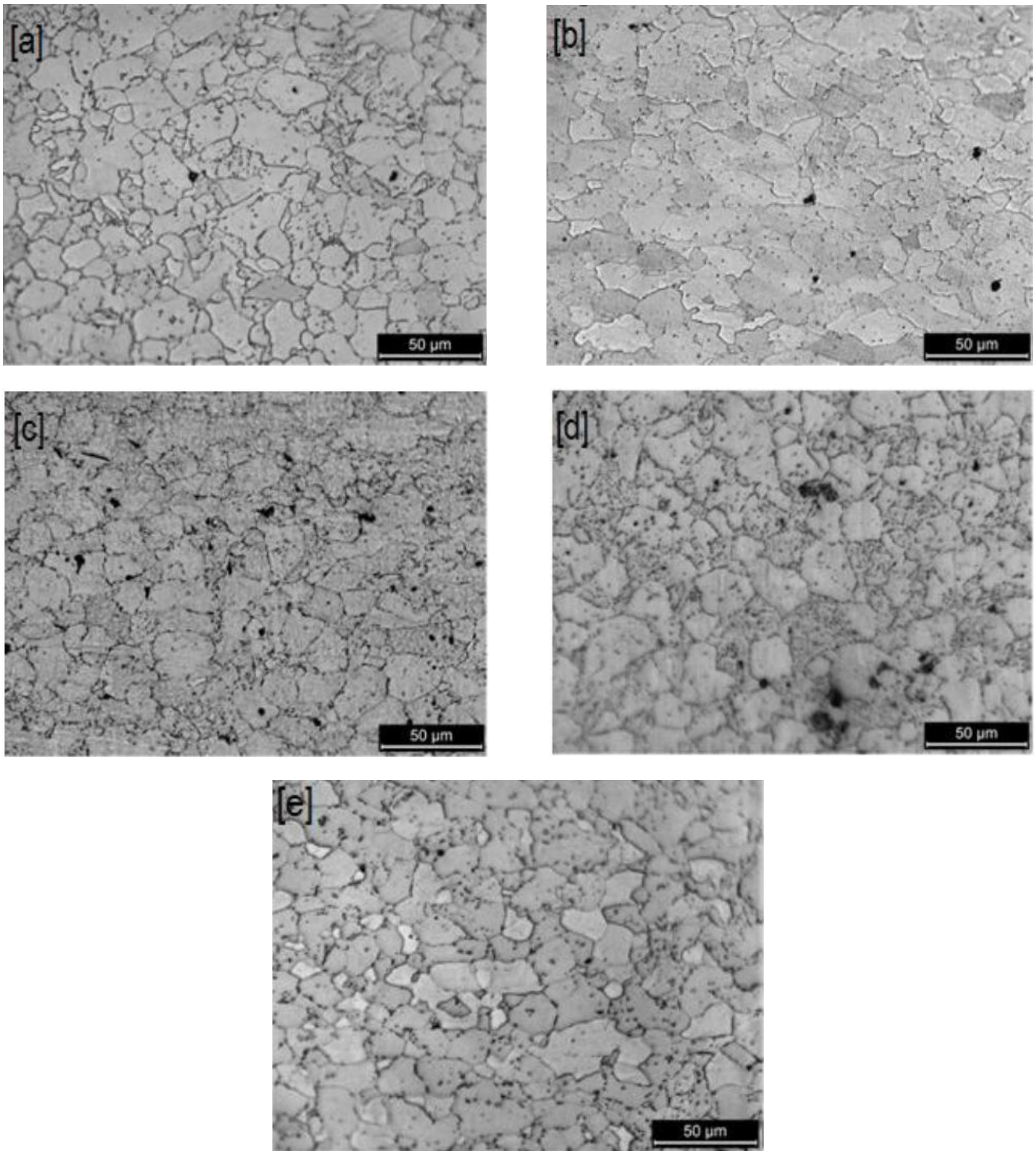

Fig. 7. *Optical microstructure of transverse section of damaged tubes:*
a) sample A1, b) sample A2, c) sample A3, d) sample B1 and e) sample B2; all samples exhibited ferrite matrices containing large voids, spheroidization& coalescence of carbides preferably along the grain boundary

seam. Thick scale (42 mg/cm²) of oxide products were loosely stuck to the inner surface near the bulging (Fig. 5d). No significant layer of oxide products was found on the outer surface.

Sample-B also contained fish mouth cracking on one part of the tube, and the other part exhibited no such degeneration. The total length of the cut portion of the tube was ~250 mm, wall thickness was ~6.2 mm while the outer diameter was ~39.0 mm. A crack developed adjacent to the weld seam with a length of ~30 mm and a maximum crack opening of ~2.8 mm. Both the inner and outer surface contained longitudinal cracking of variable length (Fig. 6). The interior of the tube was loosely covered with fine brown whiskers, which were generated from oxidation corrosion (28 mg/cm²) (Fig. 6b). However, no scale formation was observed on the outer surface of the tube. The fractured surface was dull in appearance and comprised a layered brown structure due to oxidation corrosion (Fig. 6a). Excessive thinning was found in the close vicinity of the failure. Thin lip fish mouth cracking with the presence of oxide scales at both the failed locations indicated two operating mechanisms of degeneration, i.e. oxidation corrosion followed by overload failure.

3.2 Chemical Composition

Details of the concentration of alloying elements have been collated in Table 2. The chemical composition of the bulk specimen refers to the polish composition of Steel 10H2M. The equivalent specification was close to DIN 10CrMo9-10 / T22. No remarkable variation can be observed in the chemical composition of the failed tubes. Therefore, damage owing to faulty chemistry of the alloy can be ruled out.

3.3 Microstructural Examination

The optical microstructures of the damaged components are shown in Fig. 7, which predominantly consists of polygonal ferrite. All parts of Fig. 7showing the dark voids were observed close to the grain boundary. This is an indication of creep deformation. A few globular/elliptical/near-globular diffused shaded islands of variable size can also be found. These are perhaps globular carbide present due to spheroidization under high-temperature exposure (over the operating temperature i.e. ~540 °C). With respect to the non-deformed grain shape (Figs. 7a and d), the grain shape near the fracture (Figs. 7b and e) exhibits slight increment in aspect ratio with a loss of angularity. This is an indication of material flow under stress at elevated temperature leading to further wall thinning after the initial reduction of thickness due to exfoliation.

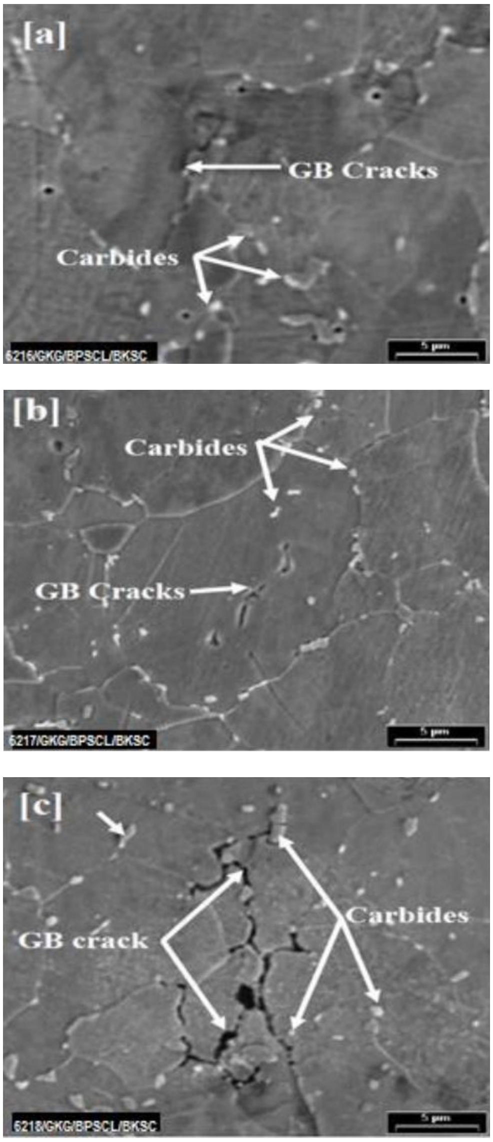

Fig. 8. *SEM micrographs of transverse section of damaged tubes: a) sample A2, b) sample A3, and c) sample B2; g.b. voids / cracks and alloy carbides were visible along grain boundary*

SEM micrographs confirmed the inferences drawn from optical imaging (Fig. 8). Along the grain boundary, bright islands indicated the spheroidization of carbides (indicated by arrows). Fig. 8 shows the void coalescence along the grain boundary, resulting in crack formation. The region close to bulging also revealed that interconnected voids that were generated during service exploitation. These voids area signature of creep damage developing at elevated temperature

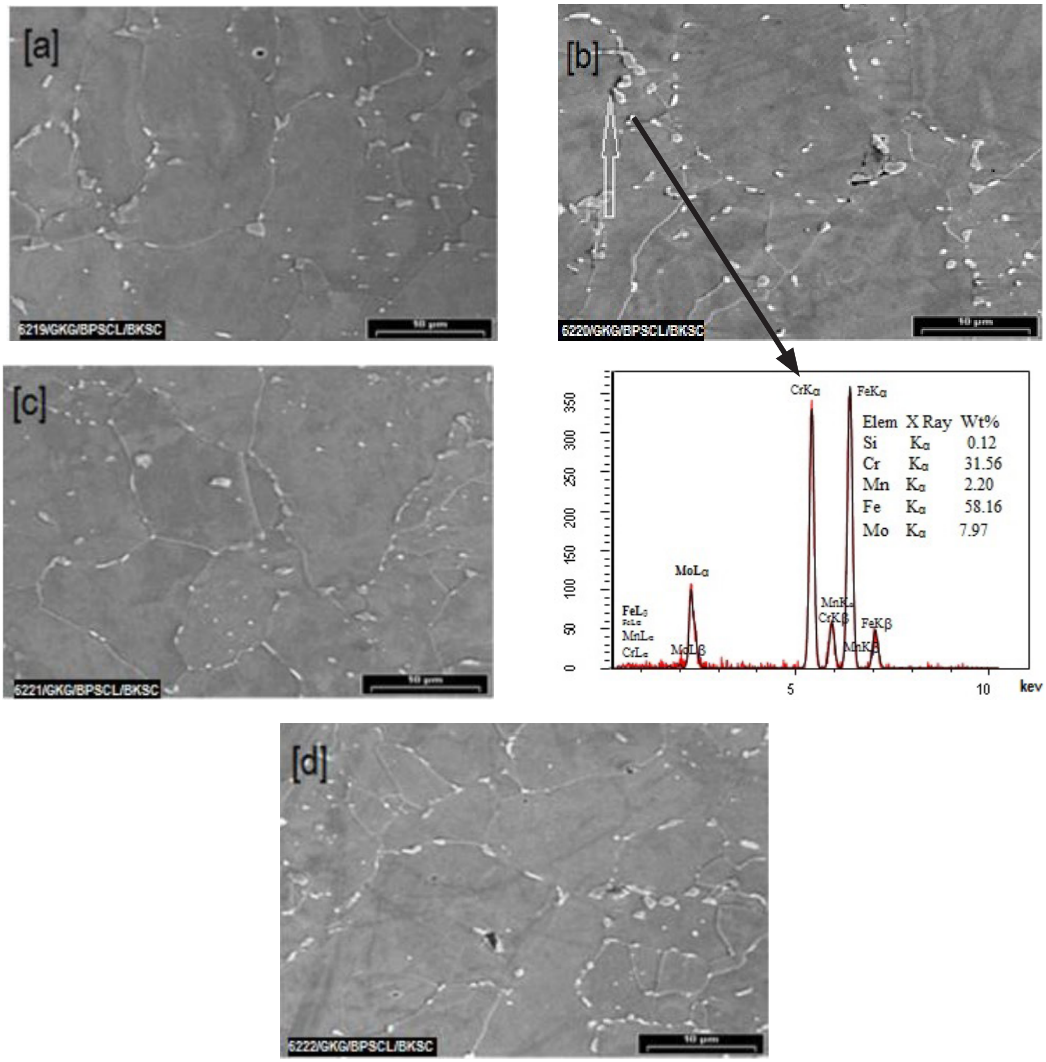

Elem	X Ray	Wt%
Si	Kα	0.12
Cr	Kα	31.56
Mn	Kα	2.20
Fe	Kα	58.16
Mo	Kα	7.97

Fig. 9. *SEM micrographs across inner to outer region of damaged tubes: a) inner - sample A4, b) outer – sample A4 with EDS spectrum from precipitate as shown in Figure 10b with quantification indicating Cr-Mo rich alloy carbide, c) inner - sample B3, and d) outer – sample B3*

under stress. The rise of local temperature beyond the designated/recommended limit over time, led to grain boundary sliding. The sliding generated decohesion/voids at the boundary. Overtime, the voids grew and became inter connected. This weakened the grain boundary strength, ultimately reducing the load bearing capability of the component. Hence, severe spheroidization of carbide and void generation are indications of local temperature rise. Therefore, temperature rises at high-stress levels cause three phenomena i.e. carbide spheroidization, creep damage to create voids, and material flow resulting in wall thinning.

SEM investigation was also carried out from inner to the outer surface to find pre-dominant structural changes, if any, in tubes near the fracture (Fig. 9). Practically, neither the inner nor outer region close to the fracture exhibit any significant change with respect to Fig. 8. The EDS spectrum was obtained from one of the precipitates along the grain boundary. Semi-quantitative analysis revealed that the precipitates were complex mixed-alloy carbides with Cr and Mo as major constituents.

3.4 Hardness Measurement

The measurement of bulk hardness at different locations of the failed component is given in Table 4. Bulk hardness near the fracture in the failed tube confirms the softening of the microstructure. Judging on the basis of the material hardness of ~200 BHN as indicated in published literature/standards for this grade of Cr-Mo steel, the hardness was found to reduce drastically near the fracture, indicating materials softening during service. The bulged area exhibited slightly more hardness assuming that the damage might be slightly less in the fractured location during the same time span. With a longer time, the hardness of bulged area might reach the hardness level of the failure location.

Table 3. *Bulk hardness of failed tubes at different location*

	Sample A2	Sample B2	Sample B3
Hardness (BHN)	114 ± 1.5	114 ± 0.5	126 ± 1

3.5 X-Ray Diffraction Study

X-ray diffraction analysis revealed the presence of different Fe-oxides and hydroxides as products of corrosion. The bulk composition of such deposits was also examined in EDS to qualitatively determine the constituents (Fig.10). Major peaks in illustration indicate the presence of iron and oxygen. Corrosion products mainly comprise iron oxide in association with small amounts of other chemical species of steel.

3.6 Fractography

SEM fractographs of both tubes are displayed in Fig. 12. Large micro-voids/dimples can be observed indicating softening of the tube material (Fig.11). The softening of the alloy was established with the reduction in bulk hardness (which is lower than 200 HB) as indicated in Table4. Ductile fracture signifies micro-void coalescence resulting in overload failure. For Sample A, the fractured surface is mostly covered with oxides, and it is difficult to explore specific features underneath, apart from the ductility failure

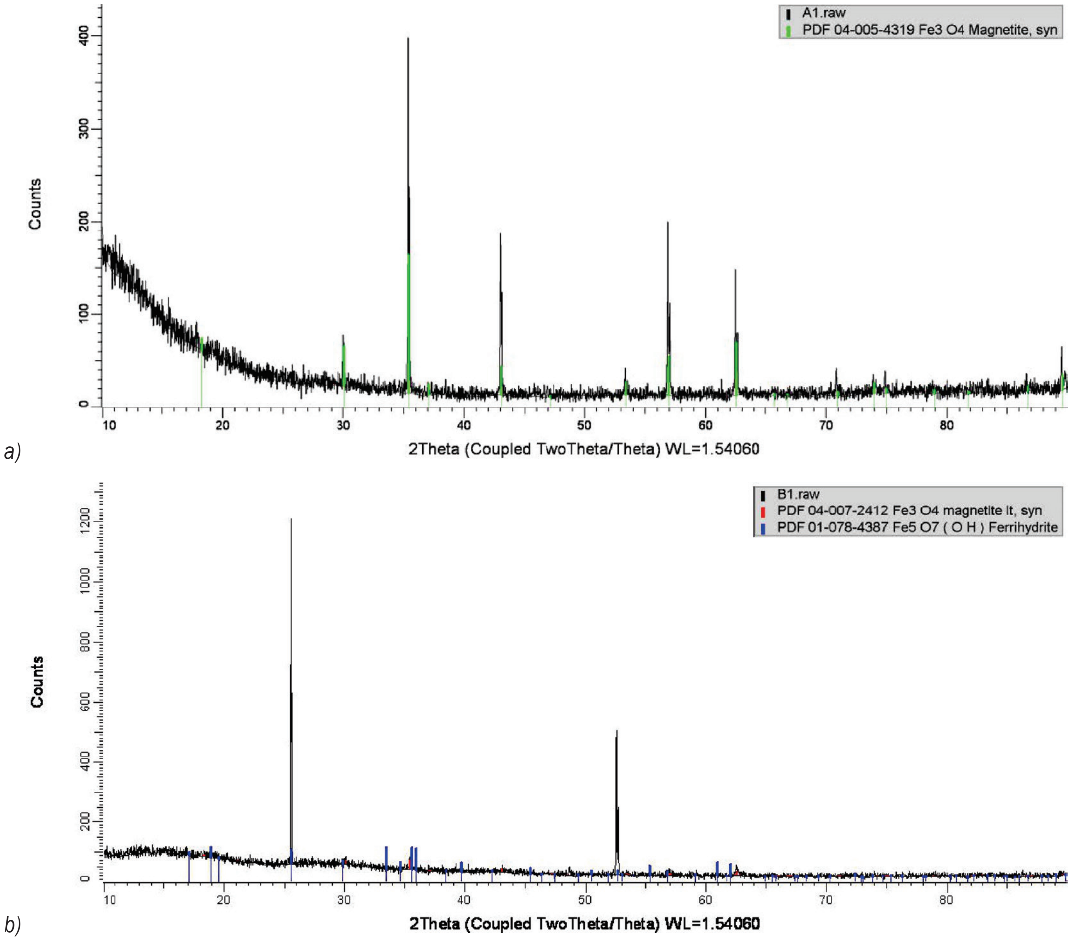

Fig. 10. *X-ray characteristic spectrum from the deposits of oxidation corrosion; a) Tube – A, and b) Tube-B; corrosion products were mostly iron oxides and hydroxides of different grades*

(Fig. 11a). However, most of the area of the fractured surface indicated ductile dimple fracture (Fig. 11b).

In certain regions, a cracked thick skin of oxide layer can be found (Fig. 12a). In case of Sample B2, inter-granular failure can be observed (arrows in Fig. 12b) at localized regions. This inter-granular cracking originated from voids adjacent to the grain boundary due to creep deformation (Fig. 8). Thus, thin lip fish mouth openings of fractured surfaces on both tubes A and B is the signature of mixed mode failure. In such case, creep deformation is accompanied by wall thinning through necking. It reduces the strength of alloy, resulting in dimple rupture. If creep happens to be the only operating mechanism, then it turns into thick lip fish mouth failure as there would be no scope for material flow/deformation to reduce wall thickness.

3.7 Evaluation of Hoop Stress

In a straight tube, any force applied over circumference/cylindrical wall (a normal stress

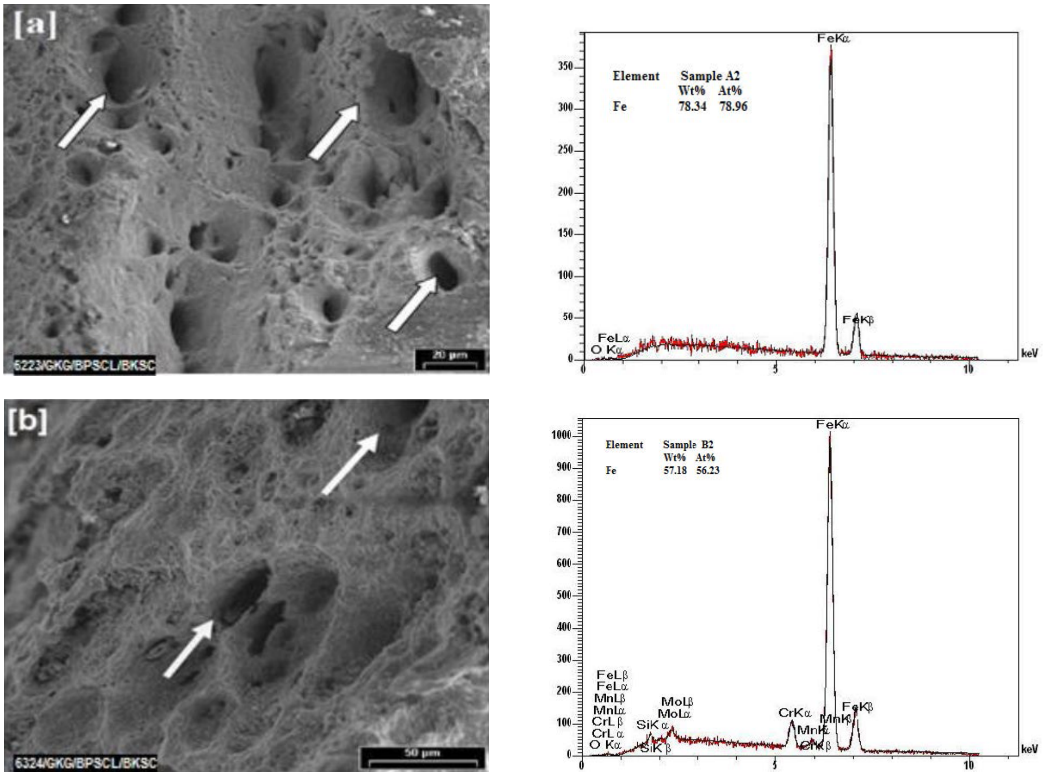

Fig. 11. *SEM fractographs of damaged tubes near sample with qualitative EDS analysis of scales formed inside a) the sampleA2, and b) the sample B2*

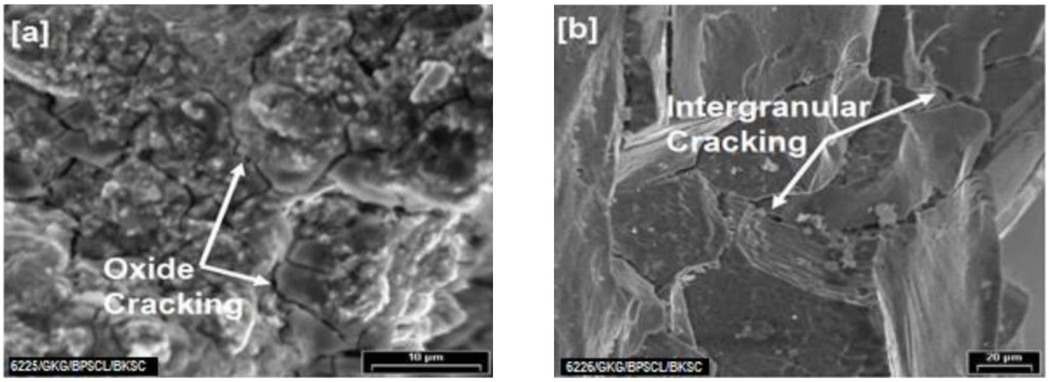

Fig. 12. *SEM fractographs of Cracks near damaged tubes; a) near sample A2 and b) near sample B2*

along tangential/azimuth direction) is termed as circumferential stress or hoop stress. Hoop stress is tensile in nature. In case of thin-walled tube, it has been assumed that wall thickness becomes no more than one-tenth of its radius. This allows the wall to be considered as a surface and subsequently applying the Young–Laplace equation for assessing the hoop stress. The thickness of thin lip at burst area of sample A & B is variable. The minimum thickness of thin lip is given in Table 4.

Table 4. *Minimum thickness of thin lip at burst area*

Thickness [mm]	Sample A	Sample B
	0.55	0.37

Fracture is governed by hoop stress in the absence of other external loads, since it is the principal stress factor. One important point to note is that the greatest stress is generated inside tubes. Hence, cracks in tubes should theoretically develop from inside the tube. Yielding is governed by an equivalent stress that includes hoop stress and longitudinal or radial stress when present. Hoop stress is expressed as:

$$\sigma = P \times d\left(2t\right)^{-1}, \qquad (1)$$

where, P is the stress in MPa, d is the internal diameter of tube in mm and t is the wall thickness in mm. By considering the inside operating pressure of tube at 100 bar, the hoop stress in non-deformed and deformed regions of tubes A and B was calculated and given in Table 5. These values have been compared with room temperature tensile properties of annealed T22 alloy.

Table 5. *Hoop stress distribution in failed tubes*

Sample ID	Hoop stress σ [MPa]		YS [MPa]	UTS [MPa]
	Non-deformed	Deformed		
Sample-A	21.3	224.7		
Sample-B	21.0	352.6		
T22 alloy			220.0	415.0

From Table 5, it is evident that in comparison with non-deformed regions, the deformed region has undergone excessive normal stress during service exploitation due to oxidation corrosion-assisted wall thinning, which is greater than the yield strength of the tube material. Considering T22 alloy, this category of Cr-Mo steel is able to retain its strength up to ~520 °C and then reduces drastically and may reach ~30 MPa (0.25 off-set yield) at ~600 °C. Therefore, apart from oxide scales, local heating beyond operating temperature propels material flow and softens to further thin the tube wall. This thin wall is unable to withstand high hoop stress, and this fails due to overloading.

4 CONCLUSIONS

In the present study, the failure mechanism in superheater tubes has been investigated. Superheater tubes were made of Cr-Mo low alloy steel, the composition of which is close to the polish specification of ‘Steel 10H2M’. Its equivalent specification is DIN 10CrMo910 / T22. The concentration of major chemical species of failed tubes was within the specified limit. Therefore, failure due to discrepancy in composition can be ruled out. As the received microstructure of steel consisted of polygonal fine grain, ferrite can be assumed to contain some amount of pearlite and complex alloy carbides. During service exposure, initially oxide scales were formed inside the tube. Thus, exfoliation inside the tube reduced the effective wall thickness. When the scale grew substantially, it hindered heat flow across the tube wall. Localized heating took place. Heating coarsened the carbides and propelled precipitation of new brittle phases along the grain boundary. At elevated temperatures, the grain boundary also lost its angularity. Moreover, due to internal deposits and partial choking, tubes are subjected to long-term overheating. The reason for long term overheating of the tube is the fact that tubes are subjected to temperatures so high that it causes their instantaneous bulging to a failure point. During this period, the outer of tubes surface develops bulging as well, resulting in elongated fissures along their axis. These two simultaneous phenomena, i.e. reduction of wall thickness of tube and its softening due to structural degeneration, come into play.

To summarize, the failure mechanism includes excessive oxidation corrosion inside the tube wall, reducing thickness, the spheroidization of alloy carbides, and the coarsening of precipitate along grain boundary. There is also loss of angularity and creep void formation along the grain boundary leading to inter-granular cracking with material flow near regions covered with thick scales. Further, there is a drastic reduction in bulk hardness (lower than 200 HB) of the tubes and, finally, thin lip fish mouth fracture develops at both the failed locations, leading to failure.

5 REFERENCES

[1] Dennies, D.P. (2005). *How to Organize a Failure Investigation.* ASM International, Ohio.

[2] Wulpi, D.J. (2000). Techniques of failure analysis. Miller, B. (ed.) *Understanding How Components Fail*. ASM International, Ohio.

[3] Brooks, C.R, Choudhury, A. (1993). *Metallurgical Failure Analysis*. McGraw-Hill, New York.

[4] Graham, R. (2004). Strategies for failure analysis. *ASM Advanced Materials & Processes*, vol. 172, no. 11, p. 45-50.

[5] Ryder, D.A., Davies, T.J., Brough, I., Hutchings, F.R. (1986). General practice in failure analysis. *Failure analysis and prevention.* Metals handbook, American Society for Metal, Ohio.

[6] Vander Voort, G.F. (2002). *Conducting the Failure Examination Practice*. ASM Handbook, ASM International, Ohio.

[7] Port, R.D., Herro, H.M. (1991). *The NALCO Guide to Boiler Failure Analysis*. Nalco Chemical Company, McGraw-Hill, New York.

[8] Rahmana, M. M., Purbolaksono, J., Ahmad, J. (2010). Root cause failure analysis of a division wall superheater tube of a coal-fired power station. *Engineering Failure Analysis*, vol. 17, no. 6, p. 1490-1494, **DOI:10.1016/j.engfailanal.2010.05.005**.

[9] Xu, L., Khan, J. A., Chen, Z. (2000). Thermal load deviation model for superheater and reheater of a utility boiler. *Applied Thermal Engineering*, vol. 20, no. 6, p. 545-558, **DOI:10.1016/S1359-4311(99)00049-6**.

[10] Krolczyk, G., Legutko, S., Stoic, A. (2013). Influence of cutting parameters and conditions onto surface hardness of duplex stainless steel after turning process. *Tehnički vjesnik - Technical Gazette*, vol. 6, no. 1, p. 1077-1080.

[11] Nieslony, P., Cichosz, P., Krolczyk, G.M., Legutko, S., Smyczek, D., Kolodziej, M. (2016). Experimental studies of the cutting force and surface morphology of explosively clad Ti–steel plates. *Measurement*, vol. 78, p. 129-137, **DOI:10.1016/j.measurement.2015.10.005**.

[12] Krolczyk, G.M., Legutko, S. (2014). Experimental analysis by measurement of surface roughness variations in turning process of duplex stainless steel. *Metrology and Measurement Systems*, vol. 21, no. 4, p. 759-770, **DOI:10.2478/mms-2014-0060**.

[13] Jones, D.R.H. (2004). Creep failures of overheated boiler, superheater and reformer tubes. *Engineering Failure Analysis*, vol. 11, no. 6, p. 873-893, **DOI:10.1016/j.engfailanal.2004.03.001**.

[14] Srikanth, S., Ravikumar, B., Das, S.K., Gopalakrishna, K., Nandakumar, K., Vijayan, P. (2003). Analysis of failures in boiler tubes due to fireside corrosion in a waste heat recovery boiler. *Engineering Failure Analysis*, vol. 10, no. 1, p. 59-66, **DOI:10.1016/S1350-6307(02)00030-4**.

[15] Chaudhuri, S. (2006). Some aspects of metallurgical assessment of boiler tubes-Basic principles and case studies. *Journal of Material Science and Engineering: A*, vol. 432, no. 1-2, p. 90-99, **DOI:10.1016/S1350-6307(02)00030-4**.

[16] Ranjbar, K. (2007). Failure analysis of boiler cold and hot reheater tubes. *Engineering Failure Analysis*, vol. 14, no. 4, p. 620-625, **DOI:10.1016/j.engfailanal.2006.03.007**.

[17] Ahmad, A., Purbolaksono, J., Beng, L. C. (2010). Failure analysis on high temperature superheater Inconel®800 tube. *Engineering Failure Analysis*, vol. 17, no. 1, p. 328-333, **DOI:10.1016/j.engfailanal.2009.06.013**.

[18] Ahmad, J., Rahman, M., Zuhairi, M.H.A., Ramesh, S., Hassan, M.A., Purbolaksono, J. (2012). High operating steam pressure and localized overheating of a primary super heater tube. *Engineering Failure Analysis*, vol. 26, p. 344-348, **DOI:10.1016/j.engfailanal.2012.08.012**.

[19] Begum, S., Karim, A.N.M., Nainar, M.A.M., Sevah, S. (2012). Analysis of end crack in boiler tube. *Advanced Materials Research*, vol. 576, p. 749-752, **DOI:10.4028/www.scientific.net/AMR.576.749**.

[20] Ananda Rao, M., Sankara Narayanan, T.S.N. (2012). Failure investigation of a boiler bank tube from a 77 × 2 MW coal based thermal power plant in the northwest region of India. *Engineering Failure Analysis*, vol. 26, p. 325-331, **DOI:10.1016/j.engfailanal.2012.04.013**.

[21] Hanke, N. (2012). Evaluation of a failed water wall boiler tube. *Journal of Failure Analysis and Prevention*, vol. 12, no. 1, p. 11-15, **DOI:10.1007/s11668-011-9522-4**.

[22] Abbasfard, H., Ghanbari, M., Ghasemi, A., Ghader, S., Rafsanjani, H.H., Moradi, A. (2012). Failure analysis and modelling of super heater tubes of a waste heat boiler thermally coupled in ammonia oxidation reactor. *Engineering Failure Analysis*, vol. 26, p. 285-292, **DOI:10.1016/j.engfailanal.2012.06.012**.

[23] Othman, H., Purbolaksono, J., Ahmad, B. (2009). Failure investigation on deformed superheater tubes. *Engineering Failure Analysis*, vol. 16, no. 1, p. 329-339, **DOI:10.1016/j.engfailanal.2008.05.023**.

[24] Purbolaksono, J., Ahmad, J., Beng, L. C., Rashid, A.Z., Khinani, A., Ali, A.A. (2010). Failure analysis on a primary superheater tube of a power plant. Engineering Failure Analysis, vol. 17, no. 1, p. 158-167, **DOI:10.1016/j.engfailanal.2009.04.017**.

[25] Botha, M., Hindley, M. P. (2015). One-way fluid structure interaction modelling methodology for boiler tube fatigue failure. *Engineering Failure Analysis*, vol. 48, p. 1-10, **DOI:10.1016/j.engfailanal.2014.10.012**.

[26] Ahmad, J., Purbolaksono, J., Beng, L.C., Rashid, A.Z., Khinani, A., Ali, A.A. (2009). Failure investigation on rear water wall tube of boiler. *Engineering Failure Analysis*, vol.16, no. 7, p.2325-2332, **DOI:10.1016/j.engfailanal.2009.03.012**.

[27] Begum, S., Karim, A.N.M., Zamani, A.S.M., Shafii, M.A. (2013). Wall thinning and creep damage analysis in boiler tube and optimization of operating conditions. *Journal of Mechatronics*, vol. 1, p. 1-6.

[28] Kumar, A., Sapra, P.K. (2013). Boiler tubes failure: Causes and remedies a case study of a fertilizer plant. *International Journal on Emerging Technologies*,vol. 4, no. 2, p. 132-135.

[29] Luo, X., Zhang, Z. (2013). Leakage failure analysis in a power plant boiler. *IERI Procedia*, vol. 5, p. 107-111, **DOI:10.1016/j.ieri.2013.11.078**.

[30] Haase, R. J., Hanke, L. D. (2013). Boiler stack economizer tube failure. *Journal of Failure Analysis and Prevention*, vol. 13, no. 5, p. 513-520, **DOI:10.1007/s11668-013-9717-y**.

[31] Šeruga, D., Fajdiga, M., Nagode, M. (2011). Creep damage calculation for thermo mechanical fatigue. *Strojniški vestnik -*

Journal of Mechanical Engineering, vol. 57, no. 5, p. 371-378, **DOI:10.5545/sv-jme.2010.108**.

[32] Saha, A., Shukla, A.K. (2014). Failure of a secondary superheater tube in a 140-MW thermal power plant. *Journal of Failure Analysis and Prevention*, vol. 14, no. 1, p. 10-12, **DOI:10.1007/s11668-013-9773-3**.

[33] Shokouhmand, H., Ghadimi,B., Espanani, R. (2015). Failure analysis and retrofitting of superheater tubes in utility boiler. *Engineering Failure Analysis*, vol. 50, p. 20-28, **DOI:10.1016/j.engfailanal.2015.01.003**.

[34] Movahedi-Rad, A., Plasseyed, S.S., Attarian, M. (2015). Failure analysis of superheater tube. *Engineering Failure Analysis*, vol. 48, p. 94-104, **DOI:10.1016/j.engfailanal.2014.11.012**.

[35] Saha, A., Roy, H., Shukla, A.K. (2015). Failure investigation of a final super heater tube in a 140 MW thermal power plant. *Journal of Failure Analysis and Prevention*, vol. 15, no. 2, p. 184-189, **DOI:10.1007/s11668-015-9928-5**.

[36] Hu, Z.F., He, D.H., Wu, X.M. (2014). Failure analysis of T12 boiler re-heater tubes during short-term service. *Journal of Failure Analysis and Prevention*, vol. 14, no.5, p.637-644, **DOI:10.1007/s11668-014-9859-6**.

[37] Javidi, M., Nematollahi, M. R., Lalehparvar, M.M., Ghassemi, A. (2016). Failure analysis of AISI 321 austenitic stainless steel water piping in a power plant. *Journal of Failure Analysis and Prevention*, vol. 16, no. 2, p. 209-215, **DOI:10.1007/s11668-016-0070-9**.

[38] Liang, Z., Jin, X., Zhao, Q.(2014). Investigation of overheating of the final super-heater in a 660 MW power plant. *Engineering Failure Analysis*, vol. 45, p. 59-64, **DOI:10.1016/j.engfailanal.2014.06.022**.

[39] Bettge, D., Klinger, C., Klingbeil, D., Eberle, A. (2014). Investigations on the breakdown of a heat recovery steam generator during the initial operation run. *Engineering Failure Analysis*, vol. 43, p. 253-270, **DOI:10.1016/j.engfailanal.2013.12.005**.

[40] Duda, P., Felkowski, L., Dobrzański, J. (2015). An analysis of an incident during the renovation work of a power boiler superheater. *Engineering Failure Analysis*, vol. 57, p. 248-253, **DOI:10.1016/j.engfailanal.2015.07.011**.

Strojniški vestnik - Journal of Mechanical Engineering 63(2017)5, 300-313
© 2017 Journal of Mechanical Engineering. All rights reserved.
DOI:10.5545/sv-jme.2016.4224
Original Scientific Paper
Received for review: 2016-11-25
Received revised form: 2017-03-03
Accepted for publication: 2017-03-27

Influence of Quasi-Steady Wind Loads on the Fatigue Damage of Wind Turbine Gearboxes

Dong Xiang* – Li Jiang – Mengxing You – Yinhua Shen
Tsinghua University, Department of Mechanical Engineering, China

Quasi-steady wind varies both in time and space and has a great influence on a wind turbine gearbox's fatigue life. Quasi-steady wind fields are described by mean wind speed and turbulence intensity, and the influence of these two parameters on wind turbine gearbox's fatigue life is studied. Based on the two-step decoupled method (the first step is global analysis and the second is gearbox dynamic analysis), a model which can calculate the complex gearbox's fatigue damage from gear's dynamic force and SN parameters is established. The fatigue damage of every gear calculated from the established model is then analysed. The fatigue damage result under certain wind loads is first analysed, and the vulnerable gears among each stage are found. Then, how mean wind speed and turbulence intensity influences fatigue damage is studied, and the damage comparison factors are calculated, which finds the 3rd stage pinion to be the gear most sensitive to wind loads, and it requires more attention when designing gearboxes. Finally, the gears' fatigue damage sensitivities to mean wind speed and turbulence intensity are analysed and the condition in which fatigue damage is more sensitive to wind loads is found, this is meaningful when designing pitch control systems.

Keywords: quasi-steady wind load, fatigue life, wind turbine gearbox, LDD, FAST, ADAMS

Highlights

- *A model that is able to calculate gears' fatigue damage under different wind loads was established, and the influence of both mean wind speed and turbulence intensity on a gearbox's fatigue life was studied.*
- *The most vulnerable gears among each stage were found based on their pitting and bending fatigue damage.*
- *Damage comparison factors were calculated to find the gear most sensitive to wind loads.*
- *The gear's sensitivity to mean wind speed and turbulence intensity was studied to find the condition in which the gear is more sensitive to these two parameters.*

0 INTRODUCTION

Wind turbines translate wind energy into electrical energy, but because wind speed varies both in time and space and over a wide variety of ranges, wind energy has more variability compared to other energy source, such as solar energy. Wind turbines frequently experience premature gearbox failures, and they are responsible for the majority of wind turbine operational downtime [1]. At the same time, the wind speed's fluctuation has a great impact on gearbox's dynamic loads. Thus, it is paramount to know how wind loads influence wind turbine gearbox's fatigue damage, especially when designing a wind turbine gearbox.

Quasi-steady wind is wind turbine's input and has a great impact on its behaviour, and the influence has been studied by many scholars. Rosen and Sheinman [2] studied turbulence's effects on wind turbine's mean power, and exhibits the great influence of wind turbulent dynamic effects on wind turbine's mean output power. Sheinman and Rosen [3] presented a new method to predict the influence of wind turbulence on the energy produced by a wind turbine and concluded that power may be over predicted by 10 % if the influence of turbulence is neglected.

The gearbox's dynamic load is a main factor influencing its fatigue life and it has been studied by many researchers. To acquire a gearbox's operational condition, a wind turbine global analysis should be done first. Jin et al. [4] proposed a blade-cabin-tower-foundation-coupled model to study the influence of seismic load on wind turbine dynamic responses. Nejad et al. [5] uses an aero-servo-hydrodynamic analysis tool to obtain forces, moments and angular velocities of the gearbox for wind turbines with different platforms. Many other researchers [5] to [11] use FAST code to acquire a gearbox's operational condition.

To obtain gearbox dynamic response under certain operational conditions, gearbox dynamic modelling should be conducted. Xu et al. [12] developed a dynamic model that integrates the gearbox body flexible supporting stiffness to study the effect of gearbox body flexibility on dynamic responses, and the result shows that dynamic transmission error and mesh force is lowered by considering body flexibility. Ajmi and Velex [13] proposed a dynamic model aimed at simulating the quasi-static and dynamic behaviour

---

*Corr. Author's Address: Tsinghua University, Beijing, China, xd@mail.tsinghua.edu.cn

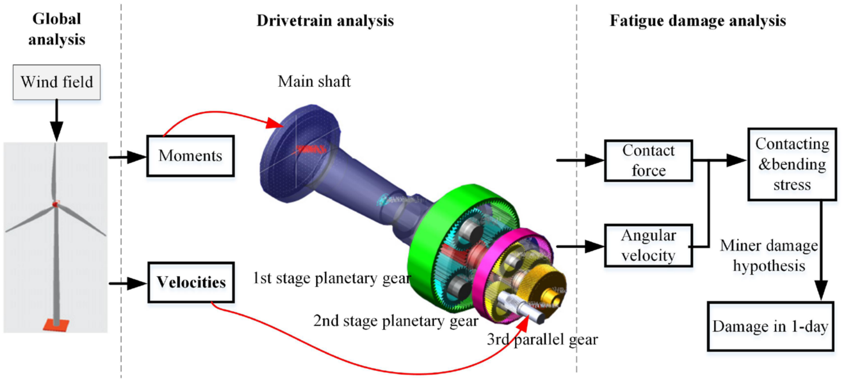

Fig. 1. *Process of calculating gearbox's fatigue damage*

of solid wide-faced gears. Osman and Velex [14] studied the interactions between contact fatigue damage and dynamic tooth loads, and the result shows that gear's contact fatigue clearly depends on dynamic phenomena. Oyague [6] introduced a two-step decoupled method to obtain gearbox's dynamic response which use FAST to get global response and SIMPACK to obtaining gearbox's dynamic response. Micallef and Sant [7] used SIMPACK to model wind turbine gearbox and used the model to study the load effects on a floating offshore horizontal axis wind turbine on surge motion. Nejad et al. [8] used both numerical and experimental methods to study the effects of floating sun gear and concluded that for errorless gears, the non-floating sun gear design performs better, while for gearbox with planet misalignment, the floating sun gear design performs better. Nejad et al. [9] established a gearbox model in SIMPACK to study the influence of mean wind speed on a wind turbine gearbox's fatigue life.

None of the above researchers studied the joint influence of mean wind speed and turbulence on a wind turbine gearbox's fatigue damage. In this paper, both the effect of these two parameters are analysed by calculating every gear's pitting and bending fatigue damage under different quasi-steady wind fields. The quasi-steady wind field is separated into two groups: NTM (normal turbulence model) and ETM (extreme turbulence model), and the fatigue damage is calculated for both these two groups using the fatigue damage calculation model established in this paper.

1 METHODS

Fig. 1 shows the details of the process of analysing wind turbine gearbox's fatigue damage, and three analysis steps are used. The first step is a global analysis which takes the quasi-steady wind field as the input and calculates gearbox's inputs and outputs. The Second step is drivetrain analysis, in which the moments and velocities acquired from the global analysis are applied to the dynamic model in ADAMS so that the dynamic loads and speeds of each gear can be obtained. The first two steps are called the "decoupled analysis method", which is also used in reference [5], [8] to [11]. The third step is fatigue damage analysis; in this step, the dynamic loads are first translated into stress bins based on the load duration distribution (LDD) method [9], and then fatigue damage is calculated from stress bins and the gear's SN parameters. The details are described as follows.

1.1 Global Analysis

Global analysis is intended to obtain the gearbox's inputs and outputs under different quasi-steady wind fields, and mean wind speed and turbulence intensity are the two chosen parameters influencing gearbox's fatigue damage. In this study, the quasi-steady wind field, which is the input to the global analysis, was generated according to the Kaimal spectrum [15] by TurbSim [16], using 20×20 points in the rotor plane with time step 0.02 s. Both the normal turbulence model (NTM) and extreme turbulence model (ETM) [17] were used to generate different wind fields. The range of mean wind speed is 5 m/s to 20 m/s with an increment of 2 m/s, and the turbulence intensity ranges from 9 % to 24 % with an increment of 2 %, the global responses of each wind speed with different turbulence intensities were obtained.

Wind turbine global simulations were conducted using the FAST code provided by NREL, which can model the dynamic responses of horizontal-axis wind turbines (HAWTs) under aerodynamic load effects [7]. The wind turbine in this study is designed by a company in China; the general description of the turbine is listed in Table 1. The main characteristics of the global analysis model are described as follows. The wind turbine is fixed to the ground, and the blade and tower are modelled as two-degree-freedom bodies. The main shaft is modelled as a torsional spring and damper, and the main parameters of the drivetrain is listed in Table 2. The blade pitch control is modified using a PI gain scheduling controller [18], and constant torque strategy is used. The integral coefficient KI and proportional coefficient KP are listed in Table 3. The outputs of global analysis, including torque on the main shaft and angular speed of the generator shaft, are shown in Fig. 2 when the mean wind speed is 11.5 m/s and turbulence is 14 %.

Table 1. *General description of the wind turbine*

Type	Three blade up wind
Power rating	1.5 MW
Rotor diameter	70 m
Rated rotor speed	17.5 rpm
Tower	Welded tabular steel
Hub height	80 m
Cut-in wind speed	3 m/s
Cut-out wind speed	25 m/s
Rated wind speed	11.5 m/s
Design wind class	IEC III
Design life	20 years

Table 2. *Drivetrain's main parameters*

parameter	value
main shaft stiffness	5e9 N·m/rad
main shaft damping ratio	1e7 N·m/s
rotor inertial	3.0854e6 kg·m^2
generator inertial	53.036 kg·m^2
Gearbox ratio	100.75

Table 3. *Pitch control system's parameters*

coefficient	KP	KI
value	0.033498	0.0089128

The rotor's torque and power determine the gearbox's behaviour, and their mean values and standard deviations under different wind fields are shown in Figs. 3 and 4, respectively. As presented in Fig. 3, the mean power is almost equal for different turbulence intensities. The mean power increases very fast when the wind speed is lower than the rated wind speed and stays constant (almost 1650 kW) when wind speed is higher. The power's standard deviation rises with the turbulence intensity, which is easy to understand. The rotor's mean torque curve, shown in Fig. 4, follows almost the same trend as the power curve, as does the standard torque deviation. All the results above which show the same regularity with the previously published result [11] can ensure the normal operation of global analysis. Since global analysis results are the inputs and outputs of drivetrain analysis, the normal operation of the global analysis can make the drivetrain analysis more reliable.

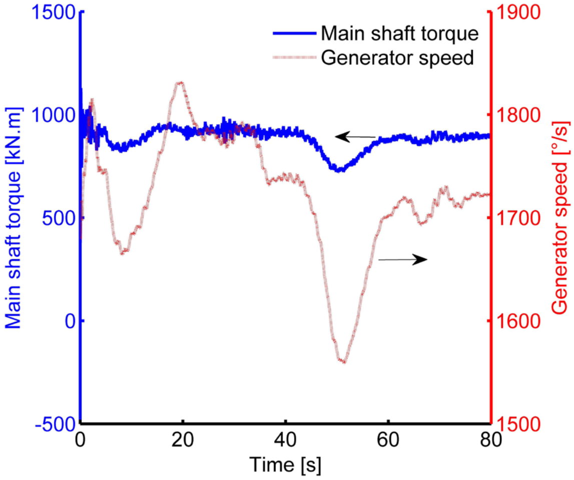

Fig. 2. *Outputs of global analysis*

1.2 Gearbox Drivetrain Analysis

To calculate every gear's fatigue damage, the dynamic loads and speeds of each gear should be obtained. Multi-body dynamic analysis software is used to calculate every gear's dynamic loads and speeds. The reference gearbox that is used in a 1.5 MW wind turbine was modelled in ADAMS, as shown in Fig. 1. The reference gearbox's schematic layout is shown in Fig. 5, it consists of three stages; the first two stages are planetary gears (3 planets), and the third stage is a parallel gear. All the components in the gearbox were modelled as rigid bodies, which are interconnected by joints and force elements. The topology diagram of the model is shown in Fig. 6. The contact force element was used to model the gear contact force. In ADAMS, the contact force is calculated using the impact function [19]. For the gearbox used in this study, whose parameter is shown in Table 4, the stiffness of each contact force element is calculated according to the Hertz theory, the force exponent is chosen to be 1.5, and the damping term is 0.1 percent of the stiffness [19], the main parameters of all contact force elements are shown in Table 5.

As shown in Fig. 1, the moment obtained from the global analysis was loaded on the main shaft, and the speed of the high-speed shaft was controlled to follow the speed obtained from the global analysis.

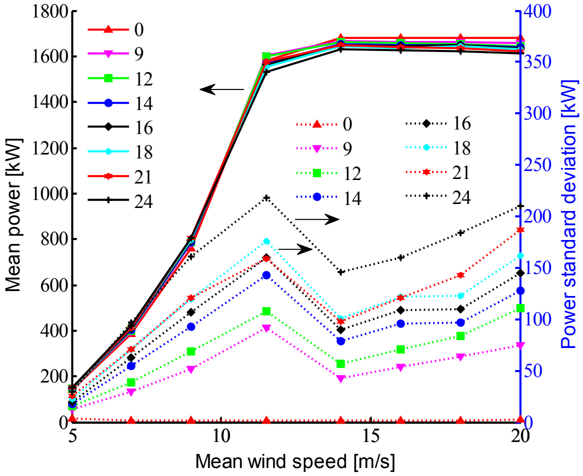

Fig. 3. *Mean and standard deviation of rotor's power*

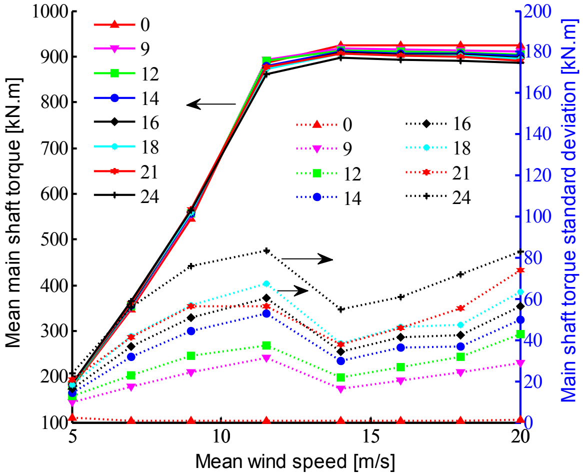

Fig. 4. *Mean and standard deviation of rotor's torque*

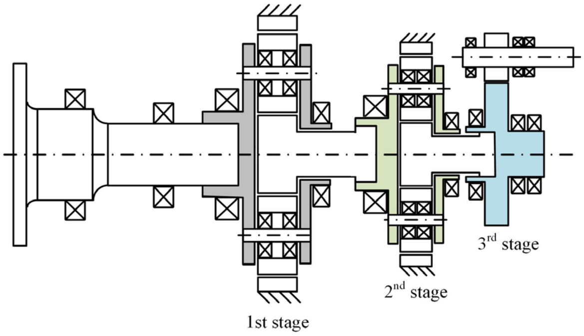

Fig. 5. *Reference gearbox schematic layout*

The simulation is carried out for 80 s with time step size to be 0.001 s, and GSTIFF-SI2 was used as the dynamics integration solver. The first 20 s of the results were discarded to avoid numerical convergence uncertainties, and the effect of the unsteady response when the wind turbine starts up. The contact force of each meshing gear was collected from the simulation result which is used in the next fatigue damage analysis part. The first stage of the sun gear's contact force, when mean wind speed is 11.5 m/s and turbulence intensity is 14 %, is shown in Fig. 7 as an example.

Table 4. *Gear parameters*

		z	M [mm]	α_n [°]	β [°]	x	b [mm]
1st	s	23	14	20	0	0.46	380
	p	34				0.48	380
	r	91				–1.42	370
2nd	s	25	9	20	0	0.28	180
	p	45				0.31	180
	r	116				–0.36	170
3rd	p	28	6	20	12	0.08	190
	G	101				0.15	180

z = number of teeth; M = normal module; β = helix angle;
x = modification coefficient; b = face width

Table 5. *Parameters of contact force elements*

	1st		2nd		3rd
	s-p	p-r	s-p	p-r	
Stiffness [kN/m]	9.6e5	1.3e6	8e5	1.1e6	8e5
Force exponent	1.5	1.5	1.5	1.5	1.5
Damping [kN·s/m]	900	1200	800	1100	800
Penetration depth [mm]	0.1	0.1	0.1	0.1	0.1

s-p = contact force element between sun and planet gear
p-r = contact force element between planet and ring gear

1.3 Fatigue Damage Analysis

The purpose of fatigue damage analysis is to calculate gears' pitting and bending fatigue damage from the obtained contact force. To calculate the gears' fatigue damage, two things need to be done: one is to translate the time-domain contact force into stress bins and another is every gear's pitting and bending SN curves (SN curve is given as $N \cdot \sigma m = K$, where σ is the maximum stress, K and m are defined as SN parameters).

The acquired contacting forces were first separated into a number of bins using the LDD method and the cycles for each force bin were calculated using Eq. (1) [9]. Next, the bending and contacting stress bins can be obtained using root bending [20] and flank contacting [21] stress calculation equations, Eqs. (2)and (3), respectively. From stress bins, the

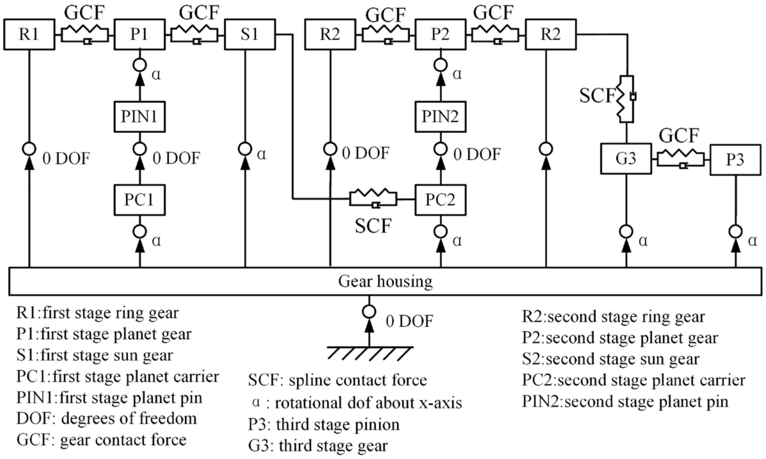

Fig. 6. *Topology diagram of ADAMS' gearbox model*

bending and contacting stress cycle at each stress level is known which is used to calculate gear's fatigue damage.

$$n_i = \sum \frac{t_j \omega_j}{2\pi}, \tag{1}$$

where n_i is the number of stress cycles of force bin i; t_j is one part of the time duration of force bin i; ω_j is the mean angular velocity of gear during t_j in rad/s.

$$\sigma_F = \frac{F_t}{bm_n} Y_F Y_S Y_\beta Y_B Y_{DT}, \tag{2}$$

where F_t is the gear contact force; b is the gear face width; m_n is the normal module; Y_F, Y_S, Y_β, Y_B and Y_{DT} are the factors considering the influence of tooth form, load application, helix angle, rim thickness and contact ratio, respectively.

$$\sigma_H = Z_H Z_E Z_\varepsilon Z_\beta \sqrt{\frac{F_t}{bd_1} \frac{u+1}{u}}, \tag{3}$$

where d_1 is the reference diameter; u is the gear ratio; Z_H, Z_E, Z_ε and Z_β are the zone factor, elasticity factor, contact ratio factor, and helix angle factor, respectively.

The SN parameters were calculated from ISO 6336-2 **[21]**, ISO 6336-3 **[20]** and ISO 6336-5 **[22]** whose fatigue data is obtained from endurance fatigue tests of reference gears. Material and heat treatment are two factors influencing gear's SN parameters, and for the studied gearbox, all gears' material is case carburized 18CrNiMo7-6 except the first and second stage's ring gear whose material is through hardened 34CrNiMo6 (note that every gear has different SN parameters). To calculate fatigue damage more precisely, a two-slope SN curve is used with the second slope to be 1/(2m–1).

After acquiring stress bins and SN parameters, the bending and pitting fatigue damages were calculated according to the Palgren-Miner linear damage hypothesis:

$$D_c = \sum_{i=1}^{N_b} \frac{n_i}{N_{ci}}, \tag{4}$$

where N_b is the total number of stress bins; n_i is the stress cycles of stress bin i; N_{ci} is the number of stress cycles leading to fatigue failure which is calculated from the SN curve; D_c is the cumulative fatigue damage.

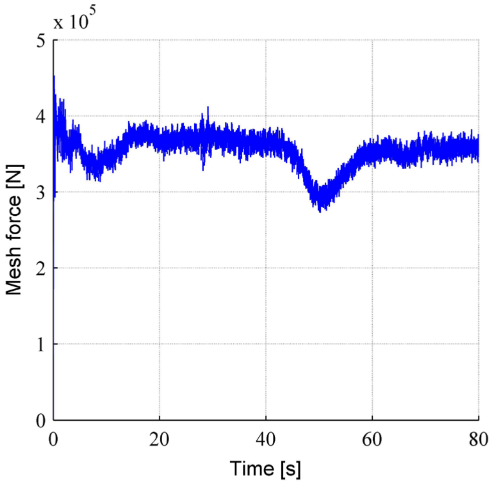

Fig. 7. *First stage sun gear's contact force*

The pitting and bending fatigue damage of each gear within one day were calculated (assuming that every minute's damage in one day is the same). A gear tooth goes in and out in every rotation so that the bending and contacting stress ranges from zero to the peak value, or in other words, the stress ratio $R = 0$. While the planetary gear is special since its forward- and back-flank are all loaded when meshing so that the planetary gear's bending stress ranges from minus peak value to peak value which means $R \approx -1$ [20]. Since there are three planets in every planetary gear train, the sun and ring gear's load cycle numbers should be multiplied by 3. From the description above, it is clear that using stress bins and SN parameters to calculate gear's fatigue damage is easy and the cumulative effect of meshing force on gear is quantified, which can be used to analyse the influence of quasi-steady wind loads or other factors on gearbox's fatigue behaviour. The calculated fatigue damage cannot only be used to compute gear's fatigue life, but also be used to compare every gear's fatigue behaviour.

Fig. 8 shows the comparison between the first stage of the sun gear's bending fatigue damage caused by NTM and ETM wind model with the mean wind speed ranges from 5 m/s to 20 m/s and turbulence intensity ranges from 12 % to 16 %. It can be observed that the damages caused by these two wind models are almost the same. Based on this conclusion, we can know that it is reasonable to only use the NTM wind model to study the effect of wind loads on gearbox's fatigue life. This phenomenon may be caused by the wind turbine's pitch control, since when the speed is beyond rated, the pitch angle is controlled so that constant input torque is acquired.

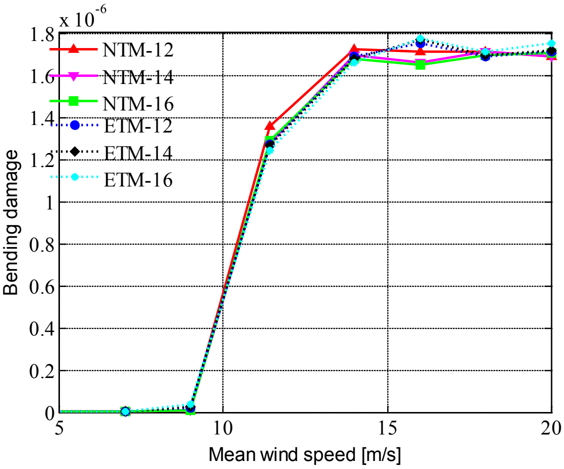

Fig. 8. *Comparison of first stage sun gear's bending fatigue damage between ETM & NTM*

2 RESULTS AND DISCUSSION

The bending and pitting fatigue damages of every gear under different quasi-steady wind loads are calculated using the above method; in this part, the fatigue damage results are presented and analysed to determine how mean wind speed and turbulence intensity influence gears' fatigue damage. The results are provided in the following order:

- To find the most vulnerable gears among each stage, fatigue damage under certain wind load is analysed.
- The fatigue damage analysis result under different wind loads section is dedicated to study the influence of quasi-steady wind loads on the fatigue damage of each gear.

2.1 Fatigue Damage Analysis Result under Certain Wind Loads

From the fatigue damage results under one or two certain wind loads, it is found that a most vulnerable component exists among each stage which has the highest fatigue damage, and the component with higher fatigue damage has a higher probability of fatigue failure. It is very useful to find the components with a higher probability of fatigue failure among each stage, which can be used in the following analysis and give the advantage of detecting the source of failure.

Table 6. *1-day tooth bending & flank pitting fatigue damage*

	gear	11.5 m/s		18 m/s	
		D_b ($\times 10^{-6}$)	D_p ($\times 10^{-6}$)	D_b ($\times 10^{-6}$)	D_p ($\times 10^{-6}$)
1st	sun	1.28	483	1.71	603.0
	planet-forward[a]	88.2	109	113.0	136.1
	planet-back[a]		0.003		0.003
	ring	437.6	0. 2	548.3	0.269
2nd	sun	0.051	38.5	0.072	48.42
	planet-forward[a]	77.0	7.13	97.6	8.97
	planet-back[a]		-		-
	ring	155.7	-	193.3	-
3rd	gear	0.596	0.010	1.023	0.014
	pinion	9.20	0.035	14.7	0.048

[a] Planet gear contacts with sun gear in the forward flank and ring gear in the back, so pitting fatigues are separated into forward- and back-pitting damage; "-" value is too small to display; D_b = bending damage; D_p = pitting damage.

The 1-day tooth bending fatigue damage at wind speed 11.5 m/s (rated wind speed) and 18 m/s with turbulence intensity to be 14 % is shown in Fig. 9 and

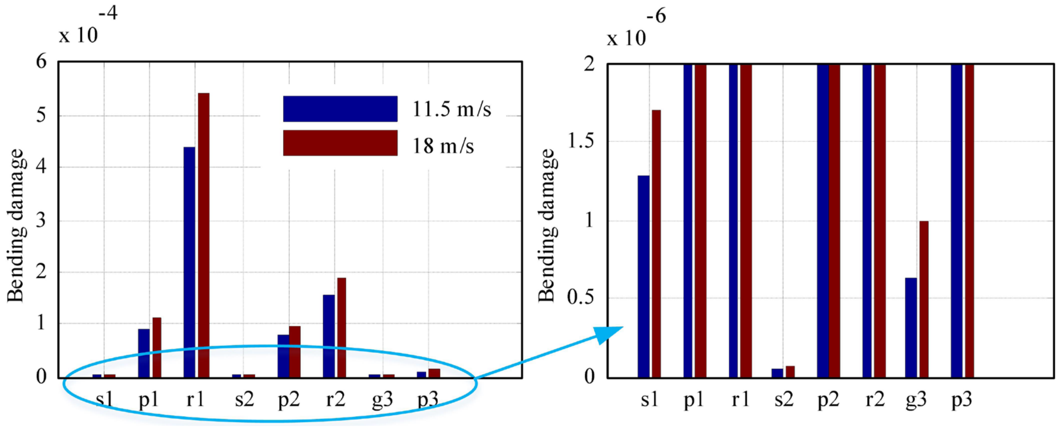

Fig. 9. *1-day gear tooth bending fatigue damage (s1 = first stage sun; p1 = first stage planet; r1 = first stage ring; s2 = second stage sun; p2 = second stage planet; r2 = second stage ring; p3 = third stage pinion; g3 = third stage gear)*

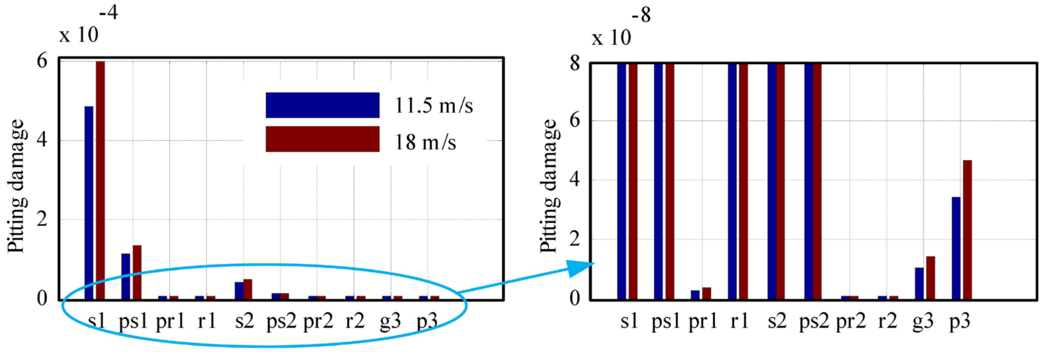

Fig. 10. 1-day gear tooth pitting fatigue damage *(s1 = first stage sun; r1 = first stage ring; ps1 = first stage planet's pitting damage caused by s1; pr1 = first stage planet's pitting damage caused by r1; s2 = second stage sun; r2 = second stage ring; ps2 = second stage planet's pitting damage caused by s2; pr2 = second stage planet's pitting damage caused by r2; p3 = third stage pinion; g3 = third stage gear)*

Table 6. The first and second stage's ring gear and third stage's pinion are found to be the components with the highest bending fatigue damage. The reason for the first and second stages' ring gear lies in the material properties since 18CrNiMo7-6 has higher nominal bending stress values (σ_{Flim}). The fatigue damage result in [23] shows sun gear to be the most vulnerable gear among the first stage, which is caused by the higher number of load cycles, while every gear has its own SN parameters considering its material, heat treatment, tooth shape, etc., so that the number of load cycles cannot determine fatigue damage. The material for ring and sun gears are through hardened 34CrNiMo6 and carburized 18CrNiMo7-6, respectively. The gear made of through hardened 34CrNiMo6 shows a lower life limit compared with 18CrNiMo7-6 at the same bending stress level, so that the ring gear would result higher bending fatigue damage even with lower number of load cycles. In contrast, for the third stage, [23] also claim that pinion is more vulnerable, this is because pinion and gear share the same material and manufacturing which result almost the same SN parameters so that higher number of cycles would result higher fatigue damage.

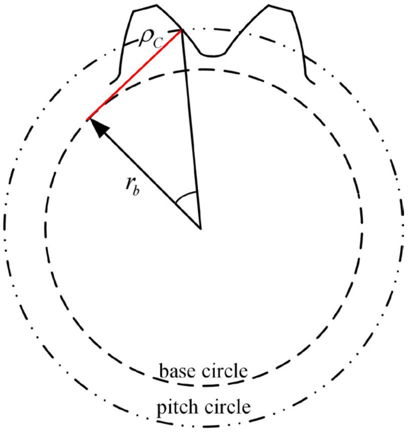

Fig. 11. *Definition of radius of relative curvature at the pitch surface*

Table 6 and Fig. 10 show the calculated 1-day flank pitting fatigue damage. The first and second stages' sun gear and third stage's pinion show higher pitting fatigue damage among each stage. The smaller radius of relative curvature at the pitch surface (ρ_C, see Fig. 11 for the definition) of the sun gear and a higher number of cycles cause the higher pitting fatigue damage of the first and second stage's sun gear. Third stage's pinion shows higher pitting fatigue damage than gear because of its higher number of cycles. The large radius of relative curvature at the pitch surface of ring gears caused small contacting stress which results in small pitting fatigue damage. From the result, the planet-backward pitting fatigue damage is much lower

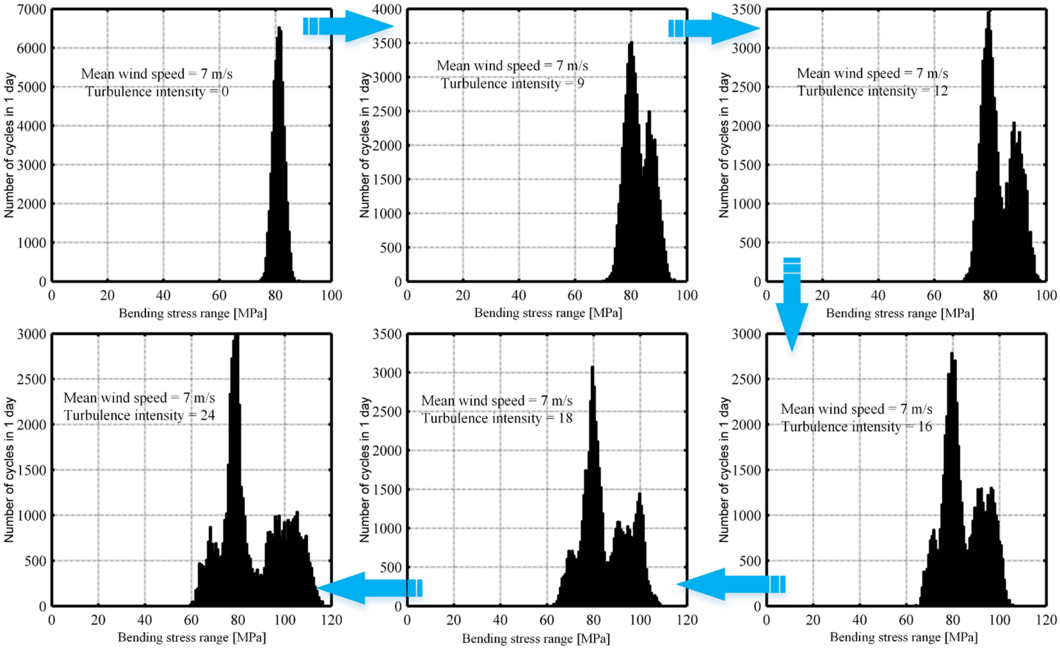

Fig. 12. *Bending stress bins of the first stage sun gear when mean wind speed is 7 m/s and turbulence intensity ranges from 0 % to 24 %*

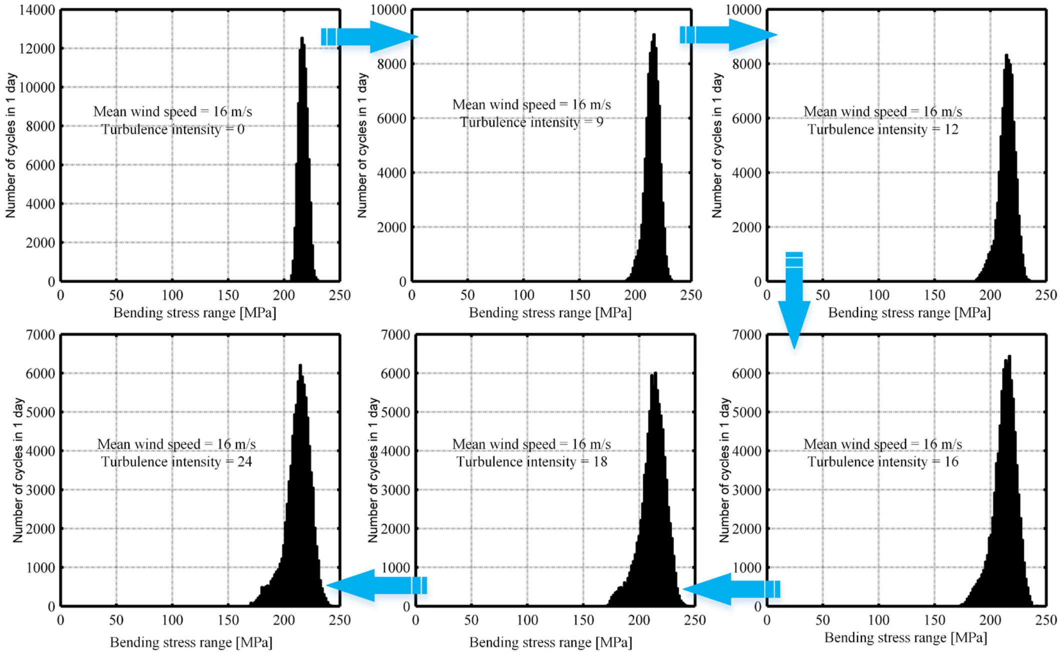

Fig. 13. *Bending stress bins of the first stage sun gear when mean wind speed is 16 m/s and turbulence intensity ranges from 0 % to 24 %*

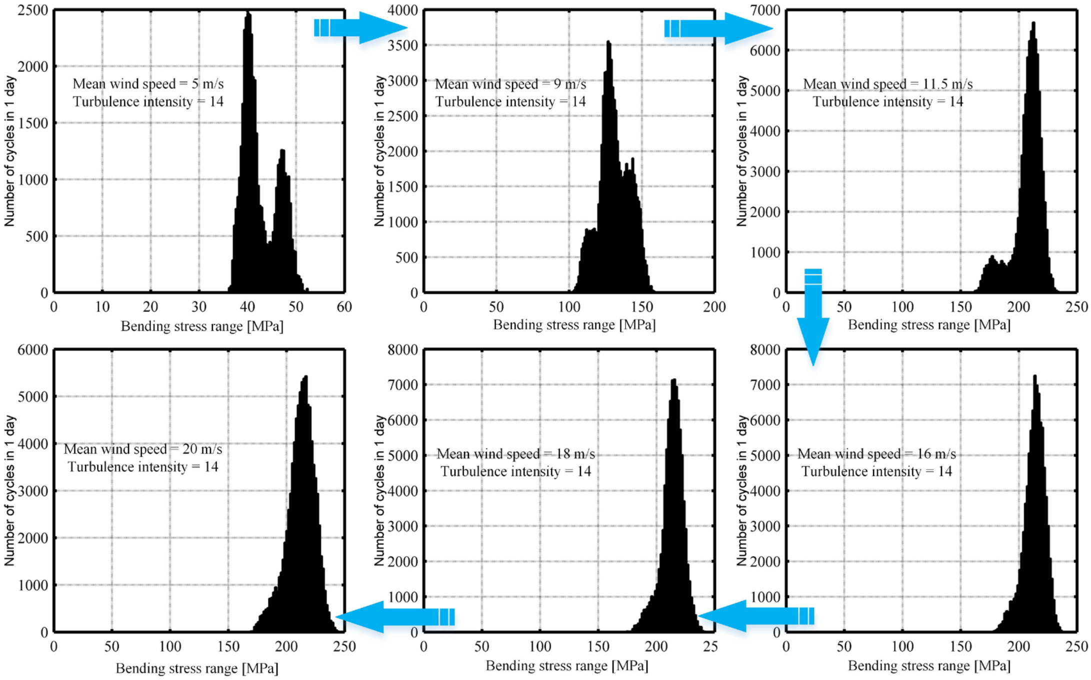

Fig. 14. *Bending stress bins of the first stage sun gear when turbulence intensity equals 14 % and mean wind speed ranges from 5 m/s to 20 m/s*

than the forward because of the ring gear's large radius of relative curvature; therefore, it is reasonable to only consider the forward pitting fatigue damage.

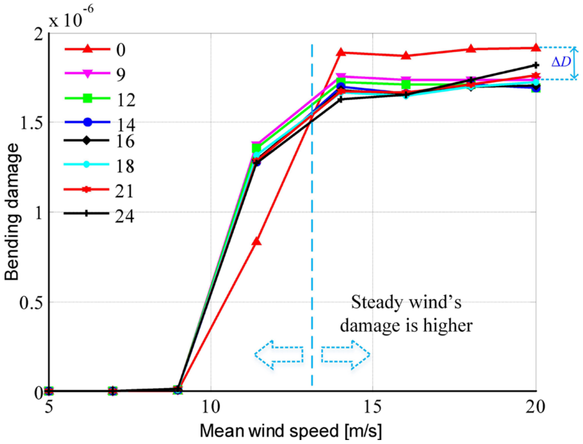

Fig. 15 *The influence of mean wind speed on first stage sun gear's bending fatigue damage*

2.2 Fatigue Damage Analysis under Different Wind Loads

From previous analysis, it can be known that it is reasonable to use only the NTM wind model to study the effect of quasi-steady wind loads on a gearbox's fatigue damage, so that a wind field generated using NTM wind model with different mean wind speeds and turbulence intensities are applied to the wind turbine, and the dynamic responses are acquired. In this section, the stress bins calculated from gearbox dynamic responses using the LDD method are first analysed to see the influence of quasi-steady wind loads on stress bins' distribution. Then, the fatigue damage under different wind loads was analysed to study the influence of mean wind speed and turbulence intensity. Finally, the sensitivities of the gears' fatigue damage to mean wind speed and turbulence intensity were calculated to find the condition in which mean wind speed and turbulence intensity has a great impact on gears' fatigue damage.

2.2.1 Stress Bins

A mechanical component's fatigue damage is calculated from stress bins and SN curve. For a specific gear, the SN curve is determined and stress bins are the only factor influencing component's fatigue damage. Therefore, it is important to study the influence of wind loads on stress bins' distribution.

Fig. 12 shows the first stage sun gear's bending stress bins when mean wind speed equals 7 m/s and turbulence intensity ranges from 0 % to 24 % (only bending stress bins are listed since contacting stress bins look the same and only 6 turbulence intensities are listed because of limited space). When the wind speed is constant, bending stress bins' distribution is concentrated in 80 MPa, and as the wind becomes more turbulent, the stress bins are distributed more dispersedly. When turbulence intensity equals 9 and 12, the distributions have two concentrations at 80 MPa and 90 MPa, and as the intensity increases, another concentration at 70 MPa is forming. It can also be seen that the concentration is moving towards the periphery.

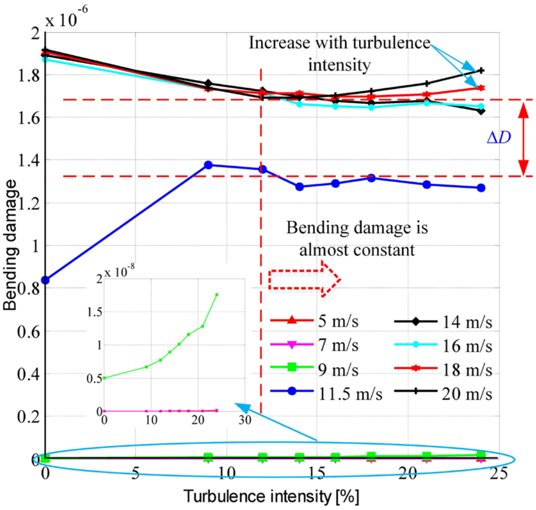

Fig. 16. *The influence of turbulence on first stage sun gear's bending fatigue damage*

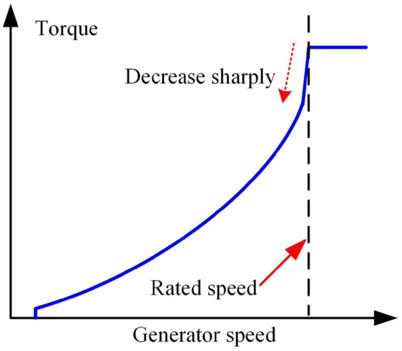

Fig. 17. *Generator torque controller*

Fig. 13 shows the first stage sun's bending stress bins when the mean wind speed is 16 m/s and turbulence intensity ranges from 0 % to 24 %. All the stress bins' distributions look similar, which is concentrated at 220 MPa, but the stress bins are distributed in a more dispersed manner as turbulence intensity increases. Stress distributes 200 MPa to 225 MPa when wind speed is constant, while 190 MPa to 230 MPa when the intensity is 9 %, 180 MPa to 230 MPa when the intensity is 12 %, 175 MPa to 235 MPa when the intensity is 16 %, 170 MPa to 240 MPa when the intensity is 18 % and 150 MPa to 250 MPa when the intensity is 24 %. The difference between Fig. 12 and Fig. 13 says that turbulence intensity has a great influence on stress bins' distribution when the mean wind speed is below the rated wind speed, while affect the distribution slightly if mean wind speed is beyond the rated wind speed.

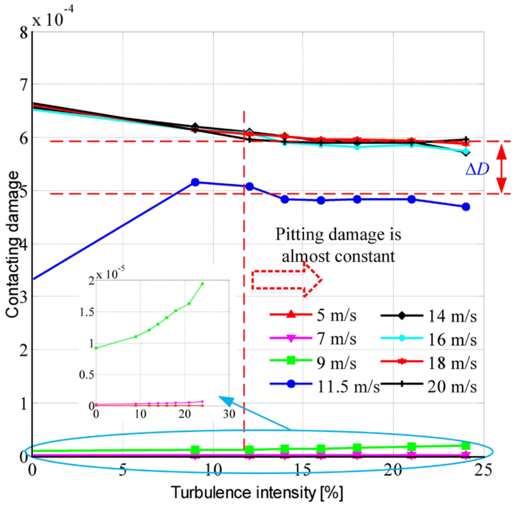

Fig. 18. *The influence of turbulence on first stage sun gear's contacting fatigue damage*

Fig. 14 shows the stress bins' distribution when the turbulence intensity is 14 % and mean wind speed ranges from 5 m/s to 20 m/s. As the mean wind speed increases, bending stress is increasing the when mean wind speed is below the rated wind speed and is almost the same when beyond. It can also be observed that as the speed increases, stress bins are becoming more concentrated, or in other words, turbulence's influence is decreasing. This is because when wind speed is beyond rated, pitch control starts to work so that the wind speed's variations can be tolerated by the pitch control which results in the decreasing effect of turbulence. When the wind speed is below rated, pitch angle stays at a constant value, and only generator speed is controlled the wind turbulence cannot be tolerated and this would cause bigger contact force variations.

2.2.2 Mean Wind Speed and Turbulence Intensity's Influence on Gears' Fatigue Damage

Mean wind speed and turbulence intensity are the two parameters determining wind speed's distribution. Both these parameters' influence on gears' fatigue damage are described in this part. First, the first stage sun gear's fatigue damage under different mean wind speeds and turbulence intensities were compared to determine how they affect gearbox's fatigue damage. Second, based on the fatigue damage result, the comparison factors were calculated according to Eq. to find the gear most sensitive to wind loads.

2.2.2.1 Influence of Mean Wind Speed and Turbulence Intensity on Gears' Fatigue Damage

The first stage sun gear's bending damage is shown in Figs. 15 and 16. Both figures contain the same data, x-axis in Fig. 15 is mean wind speed which can indicate the influence of mean wind speed on gear's bending fatigue damage, while x-axis in Fig. 16 is turbulence intensity which is intended to show the influence of turbulence. From Fig. 15, it is clear that when the mean wind speed is below the rated wind speed, fatigue damage is almost negligible compared with speed equal or beyond. As mean wind speed increases, bending damage also increases and stays almost constant when mean wind speed is larger than 14 m/s; the result proposed by Nejad et al. [9] also shows the same trend.

Fig. 15 also shows that when the mean wind speed reaches a certain value (maybe between 11.5 m/s and 14 m/s), steady wind causes higher damage than turbulent wind; this result is very interesting since in normal aspect, turbulent wind load is considered to be more dangerous. When mean wind speed is larger than 14 m/s, steady wind causes ΔD more damage than turbulent wind; this is very interesting because the normal opinion is the turbulent wind is considered to be more dangerous. As the turbulence intensity increases when mean wind speed is higher than 14 m/s, the stress bins' distribution is becoming more dispersed, and the concentration point is moving slightly towards a smaller value which causes lower fatigue damage.

It can be observed from Fig. 16 that bending fatigue damage increases with turbulence intensity if the mean wind speed is below 11.5 m/s (the shape is like a quadratic function), while when turbulence intensity increases higher than 12 %, the bending damage for the mean wind speeds equal or beyond the rated wind speed is almost constant (when mean wind speed is 18 m/s and 20 m/s, bending damage shows a rising trend, see Fig. 16). Similar to Fig. 15, after intensity reaches 12 %, which means the bending damage is almost constant for high wind speed, there is difference ΔD between rated wind speed and beyond. This is caused by the generator torque controller (a simple variable-speed controller is used in this paper), the relation between torque and speed is shown in Fig. 17, the generator torque decrease sharply when generator speed is below rated. The rated wind speed of the wind turbine model used in this study may be slightly higher than 11.5 m/s (possibly 11.6 m/s), so that generator speed is slightly below rated when the mean wind speed equals 11.5 m/s which results in a lower torque on the main shaft.

The first stage sun gear's contacting fatigue damage is shown in Fig. 18, it is almost the same as Fig. 16 since they use the same force bins. Fig. 18 is listed here to show that fatigue damage does not show a rising trend when mean wind speed is equal or beyond 18 m/s, which says that the rising trend observed in the first stage sun gear's bending damage is not general.

2.2.2.2 Fatigue Damage Comparison Factor

From the result of section 2.1, vulnerable gears with the highest pitting or bending fatigue damage among each stage were found. To see the influence of quasi-steady wind loads on every vulnerable gear's fatigue damage clearly, the fatigue damage is also presented as a percentage compared to the damage when the constant, rated wind speed is loaded. The percentage, η, is defined as:

$$\eta = \frac{D - D_{constant,rated}}{D_{constant,rated}} \times 100, \tag{5}$$

where $D_{constant,rated}$ and D are the fatigue damage when constant rated wind and other winds are loaded, respectively. From the value of η, the influence of mean wind speed and turbulence intensity can be known easily that negative η indicates less damage while positive means more.

The fatigue damage comparison factors of each gear were calculated, which is shown in Table 7. The data in the table tells how gears' fatigue damages change with wind loads, and higher values indicate that the corresponding gear's fatigue damage changes more severely as wind field changes.

There are four types of numbers in the table, dashed underline, single underline, boxed and shadowed. The values with dashed underlined indicate lower damage (only one row is listed for mean wind speed lower than rated for simplicity), the shadowed values imply comparison factors ranging from 60 % to 80 %, the boxed values are within 80 % to 100 %, and the values with single-line are beyond 100 %.

Table 7. *Fatigue damage comparison factor*

Mean wind speed [m/s]	Turbulence intensity [%]	Bending damage			Contacting damage		
		r1	r2	p3	s1	s2	p3
9	24	-94.4	-94.8	-99.6	-94.1	-95.9	-98.5
11.5	0	0	0	0	0	0	0
	9	54.9	39.2	30.4	54.9	34.9	31.3
	12	52.7	37	51.1	53	34	45.8
	14	44.9	30.9	27.4	45.2	27.2	30
	16	44.8	32.4	31.6	44.8	29.4	29.4
	18	45.6	34	18	45.5	30.1	16.7
	21	45.3	32.8	44.2	45.5	29.1	38.8
	24	41.4	28.6	31	41.3	25.1	28.4
14	*0*	***97.7***	***82.4***	**102.2**	***97.3***	***81.9***	***89***
	9	***86.9***	*67.2*	*66.3*	***86.7***	*66.2*	*61.3*
	12	***83.9***	*65.4*	*79*	***83.8***	*62.8*	*88.4*
	14	***81.1***	*61.8*	***87***	***81***	58.7	*76.1*
	16	*79.1*	*61.7*	***91.9***	*78.8*	58.2	*74.2*
	18	*77.7*	*62.3*	*73.1*	*77.3*	59.1	*64.5*
	21	*78.4*	*60.7*	*74.3*	*78.2*	58.9	*65.7*
	24	*72.5*	57.1	**102**	*72.3*	54.4	*75.3*
16	0	***97.1***	***95.5***	**203.5**	***96.4***	**102.8**	**151.1**
	9	***85***	*66*	***80.1***	***84.7***	*63.4*	*69.2*
	12	***82.7***	*64.4*	***97.3***	***82.7***	*62.3*	*79.9*
	14	*77.9*	59.7	**114.2**	*77.7*	57.6	***87.9***
	16	*76.2*	56.6	*67*	*76.2*	53.8	57.1
	18	*75.4*	58.4	**107.6**	*75.1*	55	***85.7***
	21	*76.9*	56.4	**101.6**	*76.6*	54.1	*78.4*
	24	*73.3*	55.8	**126.4**	*72.6*	53.3	***91.5***
18	0	***99.2***	***82.9***	**143.8**	***98.9***	***82.3***	**115.3**
	9	***85***	*69.3*	**107.4**	***84.8***	*67.9*	***83.9***
	12	***82.5***	*65.6*	***80.8***	***82.2***	*62.1*	*65.8*
	14	***81.5***	*62.5*	**104.1**	***81.4***	*60.1*	*78.6*
	16	***80***	58.2	***99***	*79.6*	54.7	*77.3*
	18	*79.4*	59.3	**105.3**	*79.2*	56.9	***81.6***
	21	*79*	*60.7*	**125.8**	*78.5*	58.7	***97.5***
	24	*77.7*	57.6	**195.5**	*77.1*	56.7	**135.4**
20	0	**100**	*75*	**118.3**	***99.8***	*75.6*	***95***
	9	***84.9***	*61.3*	**104.5**	***84.8***	*60.2*	*78.1*
	12	*79.4*	56.3	**114.8**	*79.3*	54.8	***89.8***
	14	*78.6*	59.2	**152.1**	*78*	57.5	**112.9**
	16	*78.1*	54.8	**136.2**	*77.7*	53.4	***94.7***
	18	***88.4***	56.7	**181.2**	*77.7*	55.3	**117.5**
	21	*78.4*	*61.7*	**192.3**	*77.8*	*61.2*	**120**
	24	*79.9*	*60.4*	**296.8**	*79.3*	58.3	**166**

The first impression of the result is that all the values with dashed-line are very close to -100, which means fatigue damage is almost neglectable. Another impression is that almost all the shadowed values are third stage pinion's bending and pitting fatigue damage, especially bending fatigue damage. This implies that the third stage's pinion is the component most sensitive to wind loads among the chosen components. It can also be observed that most of the boxed values are first stage ring gear's bending and sun gear's pitting fatigue damage, while most of the second stage ring gear's bending and sun gear's pitting comparison factors are values with a single-line or without an underline. A wind sensitivity map can be derived, which indicates the ranking of gears' fatigue damage sensitivity to wind loads, shown in Table 8. Details about gears' sensitivity to wind load will be discussed in section 2.2.3.

The results of this part are very useful in practice, the gear with higher sensitivity to wind loads needs more concern (for example it should be designed with higher reliability) when designing since wind loads have a greater impact on gear's fatigue damage, and this would cause gear's fatigue damage to become more uncertain because of wind loads' uncertainties.

2.2.3 Gears' Fatigue Damage Sensitivity to Mean Wind Speed and Turbulence Intensity

In section 2.2.2.2, the chosen components' sensitivity is divided into three levels by comparing their fatigue damage comparison factors. In this section, details about gears' sensitivity to mean wind speed and turbulence intensity will be discussed.

First-order partial derivatives are used to describe damage sensitivity, $\partial D/\partial V$ and $\partial D/\partial I$ are used to describe sensitivities to mean wind speed and turbulence intensity, respectively. To improve the result's visibility, spline interpolation is used. The first stage sun gear' contacting fatigue damage sensitivity to mean wind speed and turbulence intensity is shown in Figs. 19 and 20, respectively. Other components' fatigue damage sensitivities show little difference.

Table 8. *Levels of gears' fatigue damage sensitivity to wind loads*

Level	fatigue damage
Level-1	3rd stage pinion's bending
	3rd stage pinion's contacting
Level-2	1st stage ring gear's bending
	1st stage sun gear's contacting
Level-3	2nd stage ring gear's bending
	2nd stage sun gear's contacting

As Fig. 19 shows, sensitivity to mean wind speed (sensitivity to speed will be used in the following for simplicity) is positive for almost all wind fields. It can also be observed that sensitivity to speed does not change as turbulence intensity changes. The sectional view in Fig. 19 shows that as speed decreases, sensitivity to speed has the peak value at mean wind speed 11.5 m/s and speed below 7.9 m/s. This implies that the first stage sun gear's contacting fatigue damage is more sensitive to mean wind speed when wind speed is very low or at the rated wind speed in comparison with other cases.

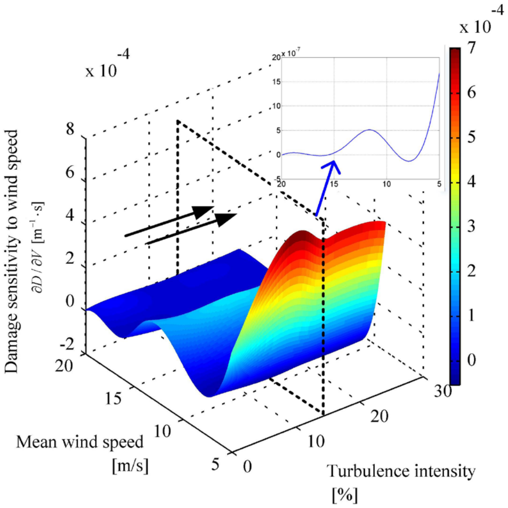

Fig. 19. *First stage sun gear's contacting fatigue damage's sensitivity to mean wind speed*

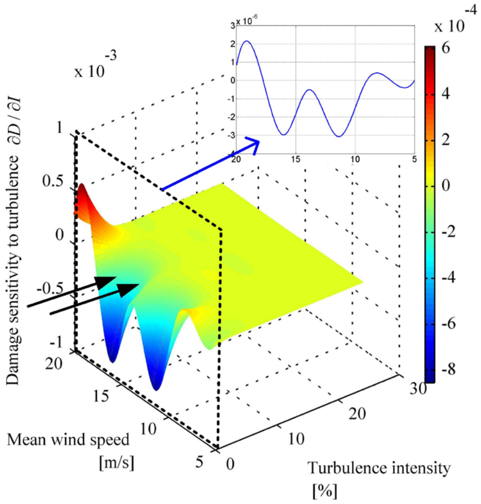

Fig. 20. *First stage sun gear's contacting fatigue damage's sensitivity to turbulence intensity*

Fig. 20 shows sensitivity to turbulence intensity, and the first impression is that when turbulence is beyond 9 %, sensitivity to turbulence is almost zero, which means turbulence has little influence on contacting fatigue damage. This is caused by the small fatigue damage value for low wind speeds. While for high wind speeds, observed from Fig. 18, it is because the turbulence has little influence on fatigue damage when turbulence intensity is greater than 12 %.

Fig. 20 also shows that when turbulence intensity is lower than 9 %, damage sensitivity varies greatly for high wind speeds. There are two valleys (negative) at speed 11.5 m/s and 16 m/s, which means that as the wind becomes more turbulent, fatigue damage would decrease. When mean speed is higher than 17 m/s, sensitivity to turbulence becomes positive and has the peak value at mean wind speed 19 m/s which means fatigue damage increases with turbulence.

Gears' sensitivity to wind loads is useful when designing a pitch control system. At some sensitive points, the pitch control system should be able to tolerate the variation of the wind loads since at these points gears' fatigue damage varies significantly as wind speed changes.

3 CONCLUSIONS

The influence of quasi-steady wind loads on wind turbine gearbox's fatigue life was studied, and the following conclusions about the influence can be drawn:

1. The vulnerable components of each stage are found based on their pitting and bending fatigue damage. This is useful for detecting the source of fault. The first and second stage's ring gear and third stage's pinion are found to be the vulnerable components considering bending fatigue. The first and second stage's sun gear and third stage's pinion were found to be the components with highest probability of pitting failure.
2. Fatigue damage is found to be almost constant when mean wind speed is higher than 14 m/s or when turbulence intensity is beyond 14 % with mean wind speed higher than rated, in other word, wind loads will not cause more fatigue damage. This is a very important conclusion since it implies that it is not the quasi-steady wind loads that accelerate the gearbox's failure. This is caused by the fast response of the pitch control system, which can tolerate wind speed's variance.
3. As the mean wind speed increases beyond 13 m/s, the fatigue damage caused by steady wind is higher than turbulent winds. This is interesting since in normal opinion, turbulent wind is more dangerous. While when mean wind speed is below rated, the fatigue damage increases with turbulence intensity, but the damage caused by mean wind speed below rated is almost neglectable compared with beyond.

4. From the vulnerable gears' damage comparison factor table, the third stage's pinion is found to be the component most sensitive to wind loads. This is meaningful when designing gearboxes, since the sensitive gear requires more concern (for example, it should be designed with higher reliability) because of the great impact of wind loads.
5. Gears' fatigue damage sensitivity to wind speed was found to be constant with turbulence intensity and has the peak value when the mean wind speed equals rated or very low (below 7 m/s). At these positive sensitivity points, especially the peak, pitch control system should be designed to be able to tolerate the variation of wind speed.

4 ACKNOWLEDGEMENTS

The authors gratefully acknowledge the support of the China National Science Foundation project "Study on energy space distribution characteristics and its influence on fatigue crack growth mechanism of wind turbine gearbox" (project number 51475263).

5 REFERENCES

[1] Musial, W., Butterfield, S., Mcniff, B. (2007). Improving Wind Turbine Gearbox Reliability. *European Wind Energy Conference*, Milan.

[2] Rosen, A., Sheinman, Y. (1994). The average output power of a wind turbine in a turbulent wind. *Journal of Wind Engineering and Industrial Aerodynamics*, vol. 51, no. 3, p. 287-302, **DOI:10.1016/0167-6105(94)90064-7**.

[3] Sheinman, Y., Rosen, A. (1992). A dynamic model of the influence of turbulence on the power output of a wind turbine. *Journal of Wind Engineering & Industrial Aerodynamics*, vol. 39, no. 1-3, p. 329-341, **DOI:10.1016/0167-6105(92)90557-Q**.

[4] Jin, X., Liu, H., Ju, W. (2014). Wind turbine seismic load analysis based on numerical calculation. *Strojniški vestnik – Journal of Mechanical Engineering*, vol. 60, no. 10, p. 638-648, **DOI:10.5545/sv-jme.2014.1646**.

[5] Nejad, A.R., Bachynski, E.E., Kvittem, M.I., Luan, C., Gao, Z. Moan, T. (2015). Stochastic dynamic load effect and fatigue damage analysis of drivetrains in land-based and TLP, spar and semi-submersible floating wind turbines. *Marine Structures*, vol. 42, p. 137-153, **DOI:10.1016/j.marstruc.2015.03.006**.

[6] Oyague, F. (2009). *Gearbox modeling and load simulation of a baseline 750-kw wind turbine using state-of-the-art simulation codes*. Technical Report, National Renewable Energy Laboratory, Golden, **DOI:10.2172/947884**.

[7] Micallef, D., Sant, T. (2015). Loading effects on floating offshore horizontal axis wind turbines in surge motion. *Renewable Energy*, vol. 83, p. 737-748, **DOI:10.1016/j.renene.2015.05.016**.

[8] Nejad, A.R., Xing, Y., Guo, Y., Keller, J., Gao, Z., Moan, T. (2015). Effects of floating sun gear in a wind turbine's planetary gearbox with geometrical imperfections. *Wind Energy*, vol. 18, no. 12, p. 2105-2120, **DOI:10.1002/we.1808**.

[9] Nejad, A.R., Gao, Z., Moan, T. (2014). On long-term fatigue damage and reliability analysis of gears under wind loads in offshore wind turbine drivetrains. *International Journal of Fatigue*, vol. 61, p. 116-128, **DOI:10.1016/j.ijfatigue.2013.11.023**.

[10] Dong, W., Xing, Y., Moan, T., Gao, Z. (2013). Time domain-based gear contact fatigue analysis of a wind turbine drivetrain under dynamic conditions. *International Journal of Fatigue*, vol. 48, p. 133-146, **DOI:10.1016/j.ijfatigue.2012.10.011**.

[11] Dong, W., Xing, Y., Moan, T. (2012). Time domain modeling and analysis of dynamic gear contact force in a wind turbine gearbox with respect to fatigue assessment. *Energies*, vol. 5, no. 11, p. 4350-437, **DOI:10.3390/en5114350**.

[12] Xu, X., Tao, Y., Liao, C., Dong, S., Chen, R. (2016). Dynamic simulation of wind turbine planetary gear systems with gearbox body flexibility. *Strojniški vestnik – Journal of Mechanical Engineering*, vol. 62, no. 11, p. 678-684, **DOI:10.5545/sv-jme.2016.3637**.

[13] Ajmi, M., Velex, P. (2005). A model for simulating the quasi-static and dynamic behaviour of solid wide-faced spur and helical gears. *Mechanism and Machine Theory*, vol. 40, no. 2, p. 173-190, **DOI:10.1016/j.mechmachtheory.2003.06.001**.

[14] Osman, T., Velex, P. (2012). A model for the simulation of the interactions between dynamic tooth loads and contact fatigue in spur gears. *Tribology International*, vol. 46, no. 1, p. 84-96, **DOI:10.1016/j.triboint.2011.03.024**.

[15] Kaimal, J.C., Wyngaard, J.C., Izumi, Y., CotéO.R. (1972). Spectral characteristics of surface-layer turbulence. *Quarterly Journal of the Royal Meteorological Society*, vol. 98, no. 417, p. 563-589, **DOI:10.1002/qj.49709841707**.

[16] Jonkman, B.J. (2009). *TurbSim User's Guide*. National Renewable Energy Laboratory, Golden, **DOI:10.2172/965520**.

[17] IEC 61400-1:2005 (2005). *Wind turbines - Part1: Design requirements*. International Electrotechnical Commission, Geneva.

[18] Lescher, F., Zhao, J.Y., Borne, P. (2006). Robust gain scheduling controller for pitch regulated variable speed wind turbine. *Studies in Informatics & Control*, vol. 14, no. 4, p. 299-315.

[19] Giesbers, J. (2012). *Contact Mechanics in MSC Adams - A technical evaluation of the contact models in multibody dynamics software MSC Adams*. University of Twente, Twente.

[20] ISO 6336-3:2006(E) (2008). *Calculation of load capacity of spur and helical gears - Part 3: Calculation of tooth bending strength*. International Organization for Standardization, Geneva.

[21] ISO 6336-2:2006(E) (2006). *Calculation of load capacity of spur and helical gears - Part 2: Calculation of surface durability (pitting).* International Organization for Standardization, Geneva.

[22] ISO 6336-5:2003(E) (2003). *Strength and quality of materials*. International Organization for Standardization, Geneva.

[23] Nejad, A.R., Gao, Z., Moan, T. (2014). Fatigue reliability-based inspection and maintenance planning of gearbox components in wind turbine drivetrains. *Energy Procedia*, vol. 53, p. 248-257, **DOI:10.1016/j.egypro.2014.07.234**.

Strojniški vestnik - Journal of Mechanical Engineering 63(2017)5, 314-319
© 2017 Journal of Mechanical Engineering. All rights reserved.
DOI:10.5545/sv-jme.2016.4247
Original Scientific Paper
Received for review: 2016-12-06
Received revised form: 2017-03-20
Accepted for publication: 2017-03-27

Drop-in Performance Analysis and Effect of IHX for an Automotive Air Conditioning System with R1234yf as a Replacement of R134a

Mehmet Direk[1,*] – Alper Kelesoglu[2] – Ahmet Akin[2]
[1] University of Yalova, Faculty of Engineering, Turkey
[2] University of Yalova, Institute of Science and Engineering, Turkey

This paper presents the experimental comparative performance analysis of an automotive air conditioning (AAC) system using R1234yf and R134a. For this purpose, an AAC experiment setup used for R134a was built to obtain the drop-in performance of a new refrigerant R1234yf. Among the low global warming potential (GWP) refrigerants, R1234yf was particularly chosen due to its similar thermo-physical properties with R134a. However, the system with R1234yf could not perform as efficiently as R134a can. Therefore, an internal heat exchanger (IHX) was employed to enhance the performance of the R1234yf system. After that, the performances of R1234yf and R134a were compared under various compressor speeds and air stream temperatures. The results showed that the cooling capacity and COP of the system with R1234yf were 17.1 % and 12.4 %, respectively, lower compared to the one with R134a. However, when the IHX was introduced into the system with R1234yf, the cooling capacity and COP values were significantly enhanced by 7.9 % and 4.1 %, respectively.

Keywords: R134a, R1234yf, automotive air conditioning, internal heat exchanger

Highlights
- *The performance of the system was examined with the refrigerants, R134a and R1234yf.*
- *The results showed that the COP of the system was higher at lower compressor speeds and air stream temperatures.*
- *The effects of a double-pipe internal heat exchanger for the system with R1234yf were investigated.*
- *The performance of the system with R1234yf was significantly enhanced by the internal heat exchanger.*

0 INTRODUCTION

Nowadays, one of the biggest problems for humankind is global warming caused by increased greenhouse gas emissions. Regarding to the global warming, the limitation studies for the usage of chlorofluorocarbon (CFC), hydrochlorofluorocarbon (HCF), and hydrofluorocarbon (HFC) continues. The usage of refrigerants that have GWP values higher than 150 in new AAC systems was restricted in 2006 by the European Parliament MAC Directive [1]. With the European Parliament Regulation No 517/2014, the MAC Directive is reconsidered and the usage of higher GWP refrigerants such as R134a (GWP value 1430) in AAC systems was planned to be prohibited starting from the year 2022 [2]. In contrast, European Parliament Regulation No 206/2012 stated that from 2014, small air conditioning systems up to 12 kW must supply coefficient of performance (COP) values at least 1.62 and 1.80 for the refrigerants that have GWP values higher and lower than 150, respectively [3]. Even though R134a can achieve the represented COP value in small air conditioning systems, its usage was prohibited by European Parliament Regulation No 517/2014. Therefore, finding an alternative refrigerant to R134a became an important task. Recent studies showed that R1234yf had significant potential as an alternative and possible replacement for R134a in AAC systems. Furthermore, cooling capacity and COP values of R1234yf could be quite similar to R134a by only applying a few simple system modifications [4]. R1234yf has similar thermo-physical properties with R134a and therefore there is no necessity for a significant change to the system. Additionally, R1234yf can be charged to the system 10% lower than R134a because of lower vapour density at higher refrigerant vapour temperature [5]. Zilio et al. [6] used R1234yf in conventional R134a AAC system which has a nominal cooling capacity of 5.8 kW. They found that R1234yf can be used in direct expansion applications because of the mild flammability properties. Qi [7] discussed the improvement potentials of R1234yf based on the simplified thermodynamic cycle analysis. He found that the system with R1234yf has 4.8 % to 7 % and 7.7 % to 10.6 % lower COP and cooling capacity values than R134a did. Abdelaziz et al. [8] made an experimental analysis to compare the performance of R134a and R1234ze. The results indicate that R1234ze has 16 % lower energy consumption than R134a did. Cho and Park [9] investigated the performance of AAC system with R1234yf. The results showed that the system with R1234yf has 3.4 % to 4.6 % lower second law efficiency than R134a did at all compressor speeds.

---

*Corr. Author's Address: Yalova University, Department of Energy Systems Engineering, Yalova, 77200, Turkey. mehmetdirek@hotmail.com

In contrast, others (Zilio et al. [6]; Navarro-Esbrí et al. [10]; Pottker and Hrnjak [11]) have reported the reductions in COP and cooling capacity when using R1234yf as a drop-in replacement for R134a. In this context, various manners of increasing the COP in a vapour compression refrigeration system can be highlighted, such as the increase of the refrigerating effect in the evaporator by means of an IHX. Domanski et al. [12] made a theoretical evaluation for different refrigerants including R134a to obtain the IHX effects on the performance parameters. They implied that the IHX in the case of R134a has positive effect for COP and cooling capacity.

Furthermore, they found that the IHX caused an increase in the compression work due to a rise in the superheat degree of the system. Aprea et al. [13] claimed that IHX has an advantage in the system performance where the system requires low suction temperature and uses R134a as a working fluid. Accordingly, they presented an inequality between the COP and suction temperature. Then, they implied that the COP of the system tends to increase with increasing suction temperature with respect to the discharge temperature limits. In addition, they assumed that the specific heat at constant pressure was temperature independent and the pressure drops in the system was negligible. As a result, they found that inaccuracies were below 5 % for different refrigerants.

Klein et al. [14] made detailed analysis with different refrigerants including R134a. They concluded that the reduction possibility of liquid containing vapour that could harm the compressor is the major benefit of the IHX. Additionally, it prevents the possibility of vapour containing liquid entering the expansion device. As a result, they showed that the relative capacity index for R134a was changed by 5 %, while the IHX effectiveness is 13 %.

Mastrullo et al. [15] experimentally investigated the performance of 19 ozone-friendly refrigerants. They claimed that the pressure drop of the liquid side in IHX is negligible, but the vapour side pressure drop has a significant influence on the system performance. They concluded that the rise in the pressure drop of the system causes the reduction in COP.

Hermes [16] claimed that the fair comparison for the system with and without IHX could be made in the case of supplying the same cooling capacity. In addition, he found that when the evaporation temperature of the refrigerant increases at a fixed condensation temperature, the COP of the system is decreased for R134a. Furthermore, he showed that the compressor discharge temperature of the refrigerant with IHX is higher than the basic cycle and this increment not only depends on the suction temperature of the compressor, but also depends on the changing evaporator pressure ratio.

Navarro-Esbrí et al. [17] found that the IHX is more effective for the system with R1234yf than R134a. They also showed that the cooling capacity and COP values improved by 2 % and 6 % when the IHX with 25 % effectiveness is added to the system. Additionally, they pointed out that there were no significant changes with pressure drops when the IHX adapted to the system. Thus, they found unity with their theoretical calculations.

Cho and Park [9] determined that the COP of the system with R1234yf is improved by up to 4.6 % when IHX was employed in the system.

Direk et al. [18] carried out an experimental analysis to compare the performance of R134a and R1234yf using a frigorific air conditioning system at different amount of charges. They claimed that the time dependent temperature gradient is compatible for both refrigerants.

Pottker and Hrnjak [11] demonstrated that the COP of the system with R1234yf is increased by increasing the sub-cooling degree of the condensed liquid refrigerant when IHX was used in the system. They used 1.5 m aluminium concentric double pipe IHX with 35 % effectiveness in their system. They found that the presence of IHX increased the sub-cooling degree, thus the COP of their system is improved by 16 %.

This study extends the performance analysis of R1234yf as an alternative to R134a for an AAC system. For this purpose, an AAC experimental setup using R134a was developed to determine the drop-in performance of R1234yf. The drop-in performance analysis was performed under different compressor speeds and air stream temperatures. Then, the effect of IHX on the performance of the AAC system using R1234yf was investigated. The experimental performance of both refrigerants was discussed and compared in terms of the cooling capacity, COP and compressor discharge temperature.

1 THERMODYNAMIC ANALYSIS

When the system reaches the steady-state conditions, the first law of thermodynamics can be used to make energy analysis for each component of the system. During the analysis, kinetic energy and potential energy variance of the system were assumed to be negligible and the compression process was assumed to be adiabatic. Regarding the performance parameters of the system, cooling capacity ($\dot{Q}_{evap}$) and ($\dot{W}_{comp}$)

values were calculated using Eq. 1 and Eq. 2. Fig. 1 symbolizes the paths of the system. Accordingly, the system without the IHX follows the cycle 1-2-3-4, and the one with IHX follows the cycle 1’-2’-3’-4’.

The cooling capacity ($\dot{Q}_{evap}$) of the AAC system can be evaluated by:

$$\dot{Q}_{evap} = \dot{m}_r \left(h_1 - h_4\right), \tag{1}$$

where $\dot{m}_r$ is the refrigerant mass flow rate and h is the enthalpy of the refrigerant.

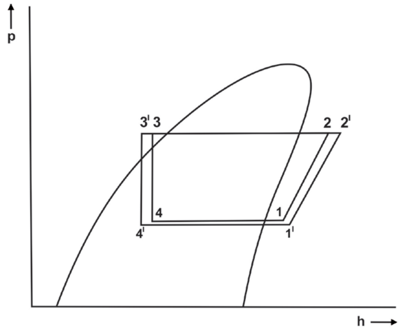

Fig. 1. *P-h diagram of the system with and without IHX*

The power absorbed by the refrigerant during the compression process can be evaluated by:

$$\dot{W}_{comp} = \dot{m}_r \left(h_2 - h_1\right). \tag{2}$$

The COP which is defined as the cooling capacity can be expressed by Eq. (3):

$$COP = \frac{\dot{Q}_{evap}}{\dot{W}_{comp}}. \tag{3}$$

2 EXPERIMENTAL SETUP

The experimental system includes the conventional AAC system components as seen in Fig. 2. The system was composed of a belt-driven swash-plate compressor, a laminar micro-channel evaporator, a parallel-flow condenser and a thermostatic expansion valve (TXV). The compressor was connected to an electric motor with an inverter. The evaporator and condenser were mounted close to the discharges of two different 1-m long air channels. The AAC components specifications for the system are reported in Table 1.

2 kW and 5 kW electrical resistance heaters were located in the evaporator and condenser channels to supply homogeneously heated air. A 900-mm double-pipe heat exchanger with 15.875 mm outer and 9.525 mm inner diameter was adapted to the system. A turbine type volume flow meter, which was located in the liquid line, was used to measure the refrigerant volume flow rate. K-type thermocouples were used to measure the refrigerant and air temperatures. The refrigerant pressures at the inlet and outlet of the compressor were monitored with a digital manifold. The measured variables were acquired through a data acquisition system and recorded on a computer. Characteristics of the instrumentation can be seen in Table 2.

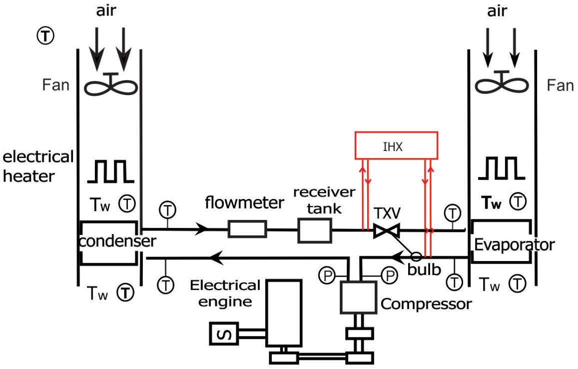

Fig. 2. *Schematic diagram of the experimental setup*

Table 1. *Specifications of equipment of automotive air conditioning system*

Component	Specification
Compressor	Stroke volume: 138 cm^3
	Cylinder numbers: 7
	Max. speed: 5000 rpm
Condenser	Capacity: 5.34 kW
	Dimensions: (635×355×20) mm^3
	No. of channels: 31
Evaporator	Capacity: 5.23 kW
	Dimensions: (210×275×70) mm^3
	No. of channels: 20

Table 2. *Specifications of the instrumentation*

Measured variable	Instrument	Range	Uncertainty [%]
Temperature [°C]	K-type thermocouple	–50 to 500	± 0.5
Pressure [bar]	Digital manifold	0 to 40	± 0.75
Humidity [%]	Hygrometer	10 to 100	± 3
Air velocity [ms^{-1}]	Anemometer	0.1 to 20	± 2
Volume flow rate [m^{3}s^{-1}]	Turbine flow meter	0.2 to 1.2	± 1

2.1 Testing Procedure

To compare the energy performance of the AAC system, experiments were conducted for R134a and

R1234yf. Before the experiments, the air temperatures at the evaporator and condenser channels were set to 27 °C or 35 °C by the electrical resistance heaters. Additionally, the AAC system was charged with 960 g and 830 g in case of testing R134a and R1234yf, respectively. Furthermore, the fans were adjusted to supply appropriate air speed and the air flow rates with respect to the evaporator and condenser channels cross sections were evaluated 0.166 m^{3}s^{-1} and 0.501 m^{3}s^{-1}, respectively. In addition, the relative humidity of the air streams measured between 50 % to 70 %. The sub-cooling and superheat degrees were maintained between 5 °C to 8 °C.

The experiments were performed under five different compressor speeds (1000, 1250, 1500, 1750, and 2000) rpm. The steady-state conditions were achieved when the air stream temperatures within a tolerance of ±0.5 °C and the sub-cooling and superheat degrees between 5 °C to 8 °C. To ensure that the system attained steady-state conditions, experiments were performed with an additional 5 minutes.

3 RESULTS AND DISCUSSION

The influence of the compressor speeds on some of the performance parameters of the AAC system was demonstrated in Figs. 3 to 6. Fig. 3 shows the variation of cooling capacity with compressor speed when the air stream temperature at the inlet of the evaporator ($T_{evap,ain}$) and condenser ($T_{cond,ain}$) maintained at 27 °C. As seen in Fig. 3 the difference between cooling capacities of the system with R1234yf and R134a were increased as the compressor speed increased. In addition, the cooling capacity of the system with R134a is higher than that of R1234yf at the same compressor speeds. The main reason for this is R134a has higher enthalpy difference value at the same temperature difference. Regarding the increasing compressor speed, the slope of the cooling capacity for R1234yf tends to decrease after 1250 rpm in comparison with R134a. However, with adequate sub-cooling degree provided from the IHX, the cooling capacity difference in comparison with R134a is virtually the same after 1250 rpm.

Fig. 4 shows that the increasing compressor speed causes a decrease in COP of the AAC system. It is understood that the COP decreases exponentially whereas the compressor power increases linearly. This is because the cooling capacity does not have the same increasing tendency with the increasing compressor speed. Furthermore, the mass flow rate of the system with R1234yf was higher than that of R134a because of the higher pressure ratios.

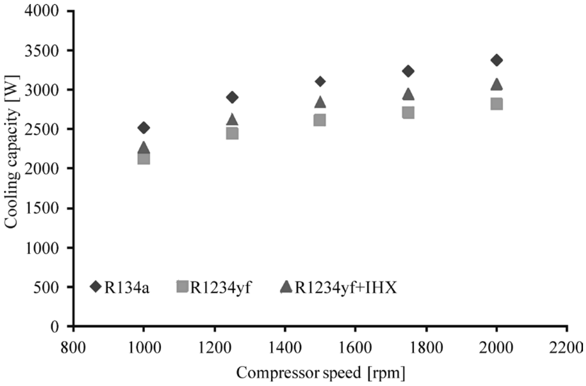

Fig. 3. *Variation of $\dot{Q}_{evap}$ cooling capacity with compressor speed ($T_{evap,ain}$ = $T_{cond,ain}$ = 27 °C)*

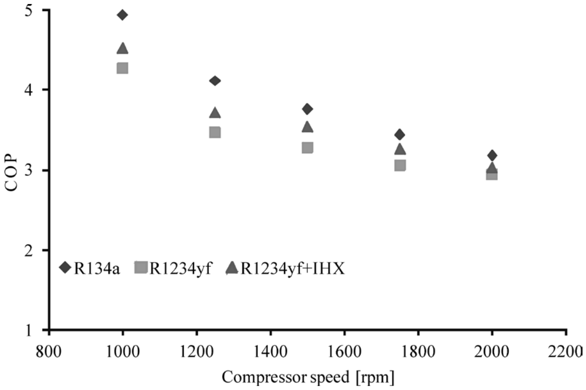

Fig. 4. *Variation of COP with compressor speed ($T_{evap,ain}$ = $T_{cond,ain}$ = 27 °C)*

From Fig. 3 and 5, it can be understood that the cooling capacity difference increases when the air stream temperature is increased. For instance, at 1250 rpm, the cooling capacity of the system with R1234yf was 13.9 % and 20.4 % lower than that of R134a.

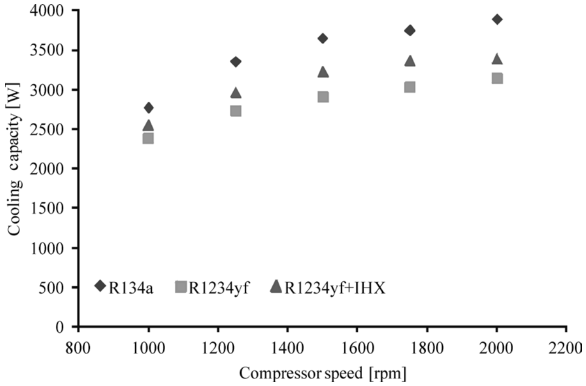

Fig. 5. *Variation of cooling capacity with compressor speed ($T_{evap,ain}$ = $T_{cond,ain}$ = 35 °C)*

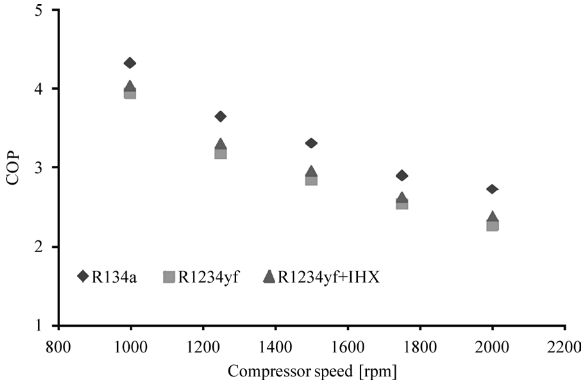

Fig. 6. *Variation of COP with compressor speed ($T_{evap,ain}$ = $T_{cond,ain}$ = 35 °C)*

Figs. 3 to 6 demonstrated that the cooling capacity and COP are higher for the system with R1234yf when using IHX. The cooling capacity and COP for R1234yf were increased by 6.3 % to 8.4 % and 6.4 % to 9.9 %, respectively when IHX used at the air stream temperatures of 27 °C and 35 °C. It is noteworthy that the cooling capacity difference between R134a and R1234yf was decreased due to the achieved suitable sub-cooling degree when the IHX was used at high compressor speeds.

Fig. 7 indicates that the discharge temperature of the compressor increases with the higher level of superheating supplied. Additionally, when the IHX was adapted to the system, a 4.2 °C and 5.2 °C increment in the discharge temperature was observed for air stream temperatures of 27 °C and 35 °C, respectively.

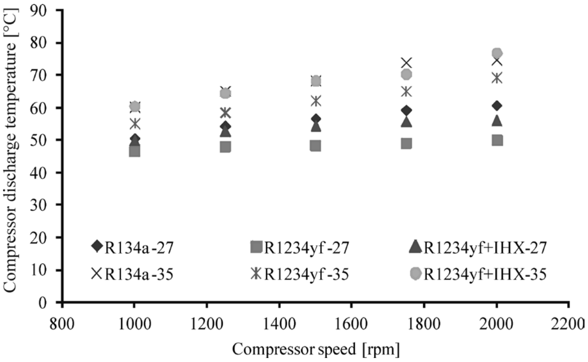

Fig. 7. *Compressor discharge temperatures*

However, R1234yf has lower discharge temperatures for all compressor speeds, with or without IHX in comparison to R134a. Thus, using R1234yf would not cause any detrimental issues in compressors with the same working conditions of R134a. That is why R1234yf will be a good alternative for the AAC system manufactured for R134a. In contrast, it was determined that the COP of the system for R1234yf was 7.5 % to 15.7 % and 8.85 % to 16.8 % lower in comparison to R134a for air stream temperatures of 27 °C and 35 °C, respectively. Finally, it was observed that the rate of increase for both cooling capacity and COP was lower for air stream temperatures of 35 °C in comparison to 27 °C.

4 CONCLUSIONS

The first aim of this study was to evaluate a drop in performance of R1234yf as a R134a replacement in the AAC system without any modification.

For this purpose, the cooling capacity and COP of the system were determined and presented as a function of compressor speeds and air stream temperatures. It was determined that the cooling capacity and COP of the system with R1234yf were 13.9 % to 20.4 % and 7.5 % to 16.5 % lower than that of R134a, respectively. Thus, it was proven that R1234yf can be a good drop in replacement of R134a not only because of the similar performance but also being a more environmentally friendly refrigerant considering the performance difference.

The second aim of the study was to determine the effect of IHX on the experimental system with R1234yf. For this reason, double pipe heat exchanger was selected and the experimental procedures were repeated. The results showed that the cooling capacity of R1234yf was improved by 6.3 % to 8.6 % and 6.4 % to 9.9 % for the air stream temperatures of 27 °C and 35 °C, respectively. The compressor power was also increased due to the superheating effect of IHX and thus increasing the equivalent heat duty of the compressor. In addition, the COP of the system was increased by 2.8 % to 7.4 % and 2.4 % to 4.8 % for air stream temperatures of 27 °C and 35 °C, respectively. After all the aforementioned analysis, it was determined that higher cooling capacity and COP can be achieved by using IHX for the system with R1234yf.

5 ACKNOWLEDGEMENTS

The authors would like to thank the University of Yalova for supporting this study through Research Project No: 2015/BAP/123.

6 REFERENCES

[1] *Regulation (EU) No 517/2014 of the European Parliament and the Council of 16 April 2014 on Fluorinated Greenhouse*

Gases and Repealing Regulation (EC) No 842/2006 (2014). Official Journal of the European Union, Brussels.

[2] *Directive 2006/40/EC of the European Parliament and of the Council of 17 May 2006 Relating to Emissions from Air Conditioning Systems in Motor Vehicles and Amending Council Directive 70/156/EC (2006).* Official Journal of the European Union, Brussels.

[3] *Regulation (EU) No 206/2012 of the European Parliament and the Council of 6 March 2012 Implementing Directive 2009/125/EC of the European Parliament and of the Council with Regard to Ecodesign Requirements for Air Conditioners and Comfort Fans (2012).* Official Journal of the European Union, Brussels.

[4] Meyer, J. (2008). HFO-1234yf system enhancements and comparison to R134a. *Proceedings of the SAE Alternative Refrigerant Systems Symposium*, Phoenix.

[5] Daviran, S., Kasaeian, A., Golzari, S., Mahian, O., Nasirivatan, S., Wongwises, S. (2016). A comparative study on the performance of HFO-1234yf and HFC-134a as an alternative in automotive air conditioning systems. *Applied Thermal Engineering*, vol. 110, p. 1091-1100, **DOI:10.1016/j.applthermaleng.2016.09.034**.

[6] Zilio, C., Brown, J.S., Schiochet, G., Cavallini, A. (2011). The refrigerant R1234yf in air conditioning systems. *Energy*, vol. 36, no. 10, p. 6110-6120, **DOI:10.1016/j.energy.2011.08.002**.

[7] Qi, Z. (2013). Experimental study on evaporator performance in mobile air conditioning system using HFO-1234yf as working fluid. *Applied Thermal Engineering*, vol. 53, no. 1, p. 124-130, **DOI:10.1016/j.applthermaleng.2013.01.019**.

[8] Karber, K.M., Abdelaziz, O., Vineyard, E.A. (2012). Experimental performance of R-1234yf and R-1234ze as drop-in replacements for R-134a in domestic refrigerators. *International Refrigeration and Air Conditioning Conference*, Purdue, p. 2241-1-2241-10.

[9] Cho, H., Park, C. (2016). Experimental investigation of performance and exergy analysis of automotive air conditioning systems using refrigerant R1234yf at various compressor speeds. *Applied Thermal Engineering*, vol. 101, p. 30-37, **DOI:10.1016/j.applthermaleng.2016.01.153**.

[10] Navarro-Esbrí, J., Mendoza-Miranda, J.M., Mota-Babiloni, A., Barragán-Cervera, A., Belman-Flores, J.M. (2012). Experimental analysis of R1234yf as a drop-in replacement for R134a in a vapour compression system. *International Journal of Refrigeration*, vol. 36, no. 3, p. 870-880, **DOI:10.1016/j.ijrefrig.2012.12.014**.

[11] Pottker, G., Hrnjak, P. (2015). Experimental investigation of the effect of condenser subcooling in R134a and R1234yf air conditioning systems with and without internal heat exchanger. International Journal of Refrigeration, vol. 50, p. 104-113, **DOI:10.1016/j.ijrefrig.2014.10.023**.

[12] Domanski, P.A., Didion, D.A., (1994). Evaluation of suction-line/liquid-line heat exchanger in the refrigeration cycle. *International Journal of Refrigeration*, vol.17, no. 7, p. 487-493, **DOI:10.1016/0140-7007(94)90010-8**.

[13] Aprea C., Ascani M., de Rossi, F. (1999). A criterion for predicting the possible advantage of adopting a suction/liquid heat exchanger in refrigeration system. *Applied Thermal Engineering*, vol. 19, no. 4, p. 329-336, **DOI:10.1016/S1359-4311(98)00070-2**.

[14] Klein, S.A., Reindl, D.T., Brownell, K. (2000). Refrigeration system performance using liquid-suction heat exchangers. *International Journal of Refrigeration*, vol. 23, no. 8, p. 588-596, **DOI:10.1016/S0140-7007(00)00008-6**.

[15] Mastrullo, R., Mauro, A.W., Tino, S., Vanoli, G.P. (2007). A chart for predicting the possible advantage of adopting a suction/liquid heat exchanger in refrigerating system. *Applied Thermal Engineering*, vol. 27, no. 14-15, p. 2443-2448, **DOI:10.1016/j.applthermaleng.2007.03.001**.

[16] Hermes, C.J.L. (2013). Alternative evaluation of liquid-to-suction heat exchanger in the refrigeration cycle. *International Journal of Refrigeration*, vol. 36, no. 8, p. 2119-2127, **DOI:10.1016/j.ijrefrig.2013.06.007**.

[17] Navarro-Esbrí, J., Molés, F., Barragán-Cervera, Á. (2013). Experimental analysis of the internal heat exchanger influence on a vapour compression system performance working with R1234yf as a drop-in replacement for R134a. *Applied Thermal Engineering*, vol. 59, no. 1-2, p. 153-161, **DOI:10.1016/j.applthermaleng.2013.05.028**.

[18] Direk, M., Tunckal, C., Yuksel, F. (2016). Comparative performance analysis of experimental frigorific air conditioning system using R-134a and HFO-1234yf as a refrigerant. *Thermal Science*, vol. 20, no. 6, p. 2065-2072, **DOI:10.2298/TSCI140715130D**.

Strojniški vestnik - Journal of Mechanical Engineering 63(2017)5, 320-330
© 2017 Journal of Mechanical Engineering. All rights reserved.
DOI:10.5545/sv-jme.2016.3843 *Original Scientific Paper*

Received for review: 2016-06-30
Received revised form: 2017-02-13
Accepted for publication: 2017-02-27

The Calculation of Meshing Efficiency of a New Type of Conical Involute Gear

Li Yu[1,3] – Guangjian Wang[1,2,*] – Shuaidong Zou[1,3]
[1] Chongqing University, State Key Laboratory of Mechanical Transmissions, China
[2] Chongqing University, College of Automotive Engineering, China
[3] Chongqing University, College of Mechanical Engineering, China

A new type of conical involute gear, proposed in this paper, can be applied in precise gear transmission for adjusting the backlash because of the special characteristics of its teeth. The meshing states of parallel external gear transmission based on the proposed gears are analysed and presented. The expressions of the length of contact and relative sliding velocity at any meshing position are derived. Then, the calculation formula of meshing efficiency is given by utilizing the piecewise equivalent method. Next, the variation of the length of contact line, unit load, meshing efficiency in a meshing period with different gear parameters and different operations are illustrated by employing numerical examples, and the influences of gear parameters and operations on meshing efficiency of the proposed gears are discussed based on the computing results. In the end, the applicability of the calculation is introduced.

Key words: conical involute gear, gear transmission, tangential modification, meshing efficiency

Highlights

- *A new type of conical involute gear for anti-backlash is introduced.*
- *The meshing states and calculation of correlative parameters of the proposed gear are presented.*
- *The meshing efficiency of the proposed gear and its variation are obtained by using detailed examples.*
- *The influences of gear parameters and operations on meshing efficiency of the proposed gear are discussed.*

0 INTRODUCTION

A new type of conical involute gear [1] and [2] (as shown in Fig. 1) is based on tangential modification or composite modification (includes the common modification and tangential modification; for distinguishing from the tangential modification, the common modification is called "radial modification" in this paper). When the gear is designed with composite modification, the radial modification coefficient is constant, and the tangential modification coefficient varies linearly along the axial direction. There is an angle between the two surfaces of the tooth; the backlash between two meshing surfaces can be adjusted by regulating the relative axial displacement of the meshing teeth, as shown in Figs. 2 and 3, so the vibration and noise can be weakened by eliminating or diminishing backlash. The characteristic of the unilateral tooth profile of this gear is similar to the involute helical gear.

In mechanical transmission, high mechanical efficiency can degrade heat generation, energy consumption, and air pollution [3] to [5]. Therefore, the friction loss is an important factor that should be taken into account during the design of gear transmission [6], chain system [7] and [8], and so on. The optimization of parameters and the utilization of high efficiency mechanical types are usually considered for heightening mechanical efficiency [3] and [5]. Recently, the application of new materials [9] and [10] and a mixture of different transmission types [11] has become an effective method to decrease friction loss in mechanical transmission.

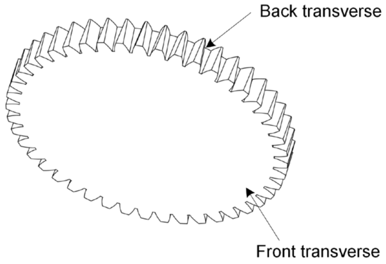

Fig. 1. *The new type of conical involute gear*

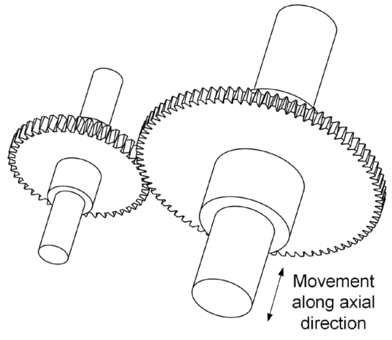

Fig. 2. *The 3D model of the external transmission*

---

*Corr. Author's Address: Chongqing University, State Key Laboratory of Mechanical Transmissions, China, r7mars@163.com

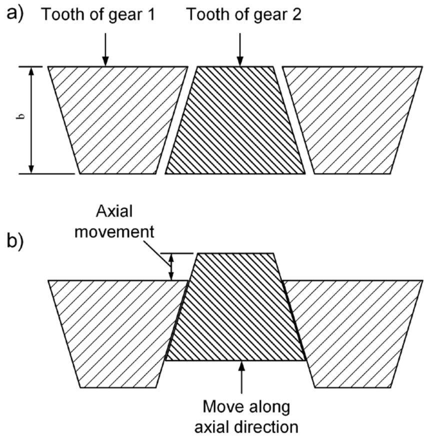

Fig. 3. *Unfolded figure at the cylindrical surface of pitch circle, a) without axial movement, b) with axial movement*

In gear transmission, the computation of efficiency can offer references for the design of gear parameters. Improving the efficiency of the gear system is beneficial to reduce frictional heat generation within the gearbox and relieve gear failure modes, such as scoring and pitting **[12]**. The friction losses caused by sliding and rolling were computed, and the actual loss along the meshing line, considering all friction factors, were studied in **[13]**. Petry-Johnson et al. **[12]** proposed the way to measure the efficiency of spur gears under high speed and variable loads. The mechanical efficiency of parallel-axis gear pairs and cross-axis gear pairs were calculated in **[14]** and **[15]**, the gear contact analysis model and a new friction coefficient formula based on Newtonian thermal elasto-hydrodynamic lubrication are applied. The sliding friction loss of helical gear transmission was computed, and the influences of helical gear parameters on meshing efficiency were studied in **[16]** to **[19]**. Seetharaman and Kahraman **[20]** and Luke and Olver **[21]** made correlative analysis and estimations of load-independent spin power losses in gear transmission. Seetharaman and Kahraman **[20]** and Diab et al. **[22]** developed numerical investigations on load-independent air-pumping power losses.

Although the meshing process of the proposed gears is the same as an involute helical gear when the rotating direction is unchangeable, the current calculation of meshing efficiency of a helical gear usually utilized the equivalent method, such as considering the helical gear as equivalent to a spur gear. The calculations mainly focused on the total efficiency of the meshing circle without illustrating the instantaneous variation of the meshing efficiency during the meshing processing. -Generally, the change of the mount of meshing teeth was not considered.

This paper studied the calculation of the meshing efficiency of the proposed gear. Firstly, the meshing process of this gear is presented in detail, and the calculating method of meshing efficiency is given. Secondly, according to the numerical calculation, the influence of gear parameters and operations on meshing efficiency is discussed. Finally, the comparison between the results in this paper and relative references is illustrated.

1 ANALYSIS OF MESHING PROCESS

The tooth surfaces of the new type of conical involute gear are helical because of the linearly variable tangential modification along the axial direction, as shown in Fig. 1. As illustrated in Fig. 4, the root of front transverse of pinion meshes first, and then the whole tooth comes into mesh until the top of the tooth in the back transverse departs from mesh. Currently, the influences of assembled and manufactured errors on efficiency in gear transmission are difficult to quantify, and the effects of the errors such as tiny eccentricity error on efficiency is very limited, so the assembled and manufactured errors are not considered in this analysis. Considering the factors such as tooth width, helical angle and length of meshing line, the probable meshing states can be expressed as seven types in Fig. 5. Defining the tangent point of the base circle and meshing line in the front transverse as the reference start, which is shown in Figs. 4 and 5, the distance between any meshing point and the reference start at any moment can be expressed as $l_x = r_b \tan\alpha_x$, which is indicated in Figs. 4 and 5.

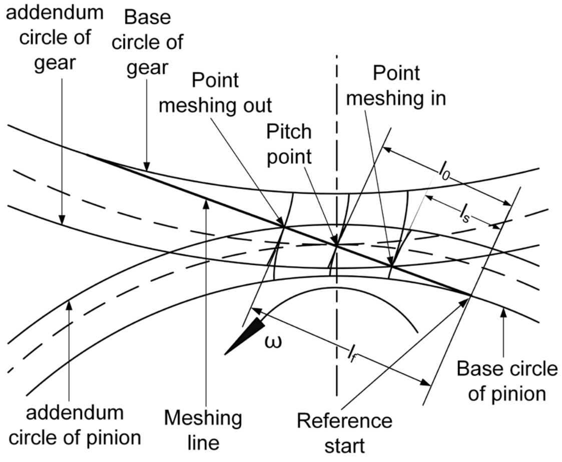

Fig. 4. *The meshing process in the front transverse*

At any meshing position in the front transverse, the length of contact line can be represented as:

$$L=\begin{cases}(l_x-\mathrm{l_s})/\sin\beta_\mathrm{b} & \mathrm{l_s}\le l_x\le \mathrm{l_{ts}}\\ \mathrm{b}/\cos\beta_\mathrm{b} & \mathrm{l_{ts}}< l_x\le \mathrm{l_f}\\ \mathrm{b}/\cos\beta_\mathrm{b}-(l_x-\mathrm{l_f})/\sin\beta_\mathrm{b} & \mathrm{l_f}< l_x\le \mathrm{l_{tf}}\end{cases}, \quad (1)$$

where $\mathrm{l_s}$, $\mathrm{l_f}$, $\mathrm{l_{ts}}$ and $\mathrm{l_{tf}}$ can be obtained through the following expressions:

$$\mathrm{l_s}=\mathrm{r_b}\tan\alpha_\mathrm{s}, \quad (2)$$

$$\mathrm{l_f}=\mathrm{r_b}\tan\alpha_\mathrm{f}, \quad (3)$$

$$\mathrm{l_{ts}}=\mathrm{l_s}+\mathrm{b}\tan\beta_\mathrm{b}, \quad (4)$$

$$\mathrm{l_{tf}}=\mathrm{l_f}+\mathrm{b}\tan\beta_\mathrm{b}. \quad (5)$$

In Eqs. (2) and (3), α_s and α_f can be computed based on the gear parameters.

At any meshing moment, the relative sliding velocity of any meshing point on the contact line can be expressed as:

$$v_s=\begin{cases}(1+1/\mathrm{i_0})\omega_1(\mathrm{l_0}-l_x+y\sin\beta_\mathrm{b}) & l_x\in[\mathrm{l_s},\mathrm{l_0}]\\ (1+1/\mathrm{i_0})\omega_1\left\|l_x-\mathrm{l_0}\right|-y\sin\beta_\mathrm{b}| & l_x\in[\mathrm{l_0},\mathrm{l_t}]\\ (1+1/\mathrm{i_0})\omega_1(l_x-\mathrm{l_0}-y\sin\beta_\mathrm{b}) & l_x\in[\mathrm{l_t},\mathrm{l_f}]\\ (1+1/\mathrm{i_0})\omega_1(\mathrm{l_f}-\mathrm{l_0}-y\sin\beta_\mathrm{b}) & l_x\in[\mathrm{l_f},\mathrm{l_{tf}}]\end{cases}, \quad (6)$$

where ω_1 is the angular velocity of the pinion, $\mathrm{l_t}$ is distance between the meshing point and the reference start in the front transverse while the back transverse meshes across the pitch point, $\mathrm{i_0}$, $\mathrm{l_0}$ and $\mathrm{l_t}$ can be obtained as below:

$$\mathrm{i_0}=\mathrm{z_2}/\mathrm{z_1}, \quad (7)$$

$$\mathrm{l_0}=\mathrm{r_b}\tan\alpha_0, \quad (8)$$

$$\mathrm{l_t}=\mathrm{l_0}+\mathrm{b}\tan\beta_\mathrm{b}, \quad (9)$$

where α_0 is the engagement angle at pitch circle, and α_0 is 20° when the radial modification is zero, as shown in Fig. 5.

According to Eqs. (1) to (5), the length of contact line is available during a meshing circle, and the whole meshing process could be divided into many micro-segments, so the variation of the length of contact line is obtained. On the basis of Eq. (6), the relative sliding velocity of any meshing point on contact line is available, and its variation along the contact line and meshing line can be acquired by considering the gear consists of many micro-pieces along the axial direction.

2 THE CALCULATION OF MESHING EFFICIENCY

In actual application, if the input power is constant, the meshing efficiency can be derived by computing the power of sliding friction.

The power of sliding friction is caused by the common action of the relative sliding between the meshing surfaces and the load on the surfaces, which is also affected by the coefficient of friction between the surfaces, these relationships can be illustrated by the following expression:

$$P_f=\mu F v_s. \quad (10)$$

In most of the engagement process, the number of meshing teeth is more than one, and the calculation of the total length of contact lines usually involves two or more pairs of teeth and their meshing position on the meshing line. According to Eq. (10), the power of sliding friction of meshing points varies instantaneously along with the position on contact line and meshing line.

2.1 Calculation of Unit Load

To simplify the calculation, the load distribution of teeth is thought to be uniform, which means the effect of the deformation and stiffness of the teeth is not considered, so the unit load can be expressed as:

$$F_{ei}=\frac{\mathrm{M}}{\mathrm{i_0}*\mathrm{r_b}\sum_{\mathrm{k}=1}^{N}L_k}, \quad (11)$$

where L_k is the length of the contact line of the k^{th} meshing tooth, N is the number of the meshing teeth.

If the position of the meshing point in the front transverse of reference tooth is expressed as l_{x1}, the position of the meshing point in the front transverse of the k^{th} meshing tooth before the reference tooth can be derived by the formula below:

$$l_{xi}=l_{x1}+k*\mathrm{p_b}. \quad (12)$$

Quoting the result of Eq. (12), the length of the contact line of the k^{th} meshing tooth is available with Eq. (1), and the unit load also can be computed with Eq. (11).

2.2 Calculation of Relative Sliding Velocity

Referring to the transformation mentioned above, the relative sliding velocity of any meshing point on the contact line at any meshing moment can be calculated with Eq. (6). Taking the front transverse

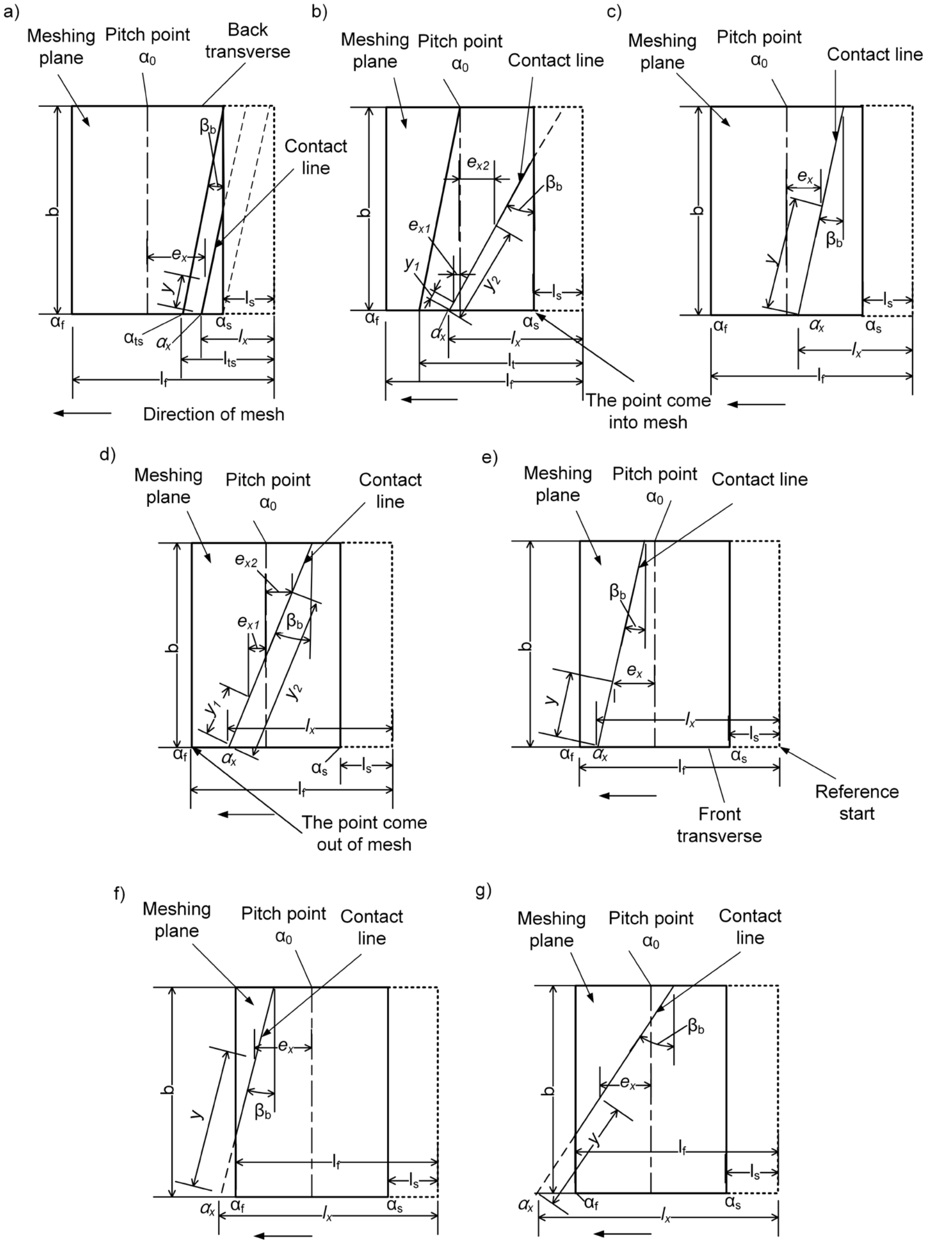

y—The distance between any meshing point on the contact line and the front transverse along contact line, when the contact line is at the same side of pitch point;

y_1, y_2—The distance between the meshing points on the contact line and the front transverse along contact line, when the meshing points are respective at different sides of pitch point;

e_x—The distance between any meshing point and the pitch point along meshing line in any transverse, when the contact line is at the same side of pitch point;

e_{x1}, e_{x2}—The distance between the meshing points and the pitch point along meshing line, when the meshing points are respective at the different sides of pitch point;

Fig. 5. *The probable meshing states; a)the meshing point in front transverse doesn't arrive at the pitch point and the tooth partly comes into mesh; b) the meshing point in front transverse has meshed across the pitch point, but the tooth does not totally come into mesh; c) the meshing point in front transverse does not arrive at the pitch point while the whole tooth is in mesh; d) the meshing point in front transverse has meshed across the pitch point, and the meshing point in back transverse has not arrived at the pitch point, while the whole tooth is in mesh; e) the meshing points in the back transverse have meshed across the pitch point while the whole tooth is in mesh; f) the meshing point in the back transverse has meshed across the pitch point while the tooth has partly meshed out; g) the meshing point in back transverse has not arrived at the pitch point while the tooth has partly meshed out*

as the reference, the position of any meshing point on contact line along meshing line can be denoted as:

$$l_{xi} = l_{x1} + k * \mathrm{p_b} - y_\mathrm{k} \sin\beta_\mathrm{b}, \tag{13}$$

where y_k is the distance between any meshing point of the k^{th} meshing tooth to the front transverse along contact line.

So the relative sliding velocity of any meshing point on the contact line of the k^{th} tooth at any moment can be derived by taking Eq. (13) into Eq. (6).

2.3 Friction Coefficient

The friction coefficient is an important factor in calculating the power of sliding friction, which depends on the load, parameters of gear, the surface roughness of tooth, lubrication, lubricant viscosity, and other factors. Although the empirical formulas for calculating the coefficient of friction were summarized with the theoretical derivation and experimental model in [23] to [33], these studies were usually had certain limitations because of the difficulties of actual test and the influence of multi-factors, so it is still difficult to propose a generally applicable formula and exactly test in practice. This paper referred the mean coefficient of friction in [4], [31] to [33], which is described as follows:

$$\mu = 0.048\left(\frac{\mathrm{F_{bt}}/\mathrm{b}}{\upsilon_{\Sigma\mathrm{c}}\rho_\mathrm{c}}\right)^{0.2}\eta^{-0.05}\mathrm{R}_a^{0.25}\mathrm{X_L}, \tag{14}$$

where $\mathrm{X_L}$ is the lubricant factor, considering $\mathrm{X_L} = 1$ for mineral oil here [30] and [32], R_a is the surface roughness, and $\upsilon_{\Sigma\mathrm{c}}$ can be calculated as:

$$\upsilon_{\Sigma\mathrm{c}} = 2 \cdot \upsilon_\mathrm{t} \cdot \sin\alpha_0.$$

From Eq. (14), it can be observed that the friction coefficient is constant during the meshing process when the gear parameters and operations are definite. At the same time, the gear parameters and operations are the main determinants of the coefficient of friction. Thus, the influence of gear parameters and operations on meshing efficiency can be well studied. In contrast, the utilization of Eq. (14) is also helpful for comparing the computing results of efficiency with the results calculated by the method in [4].

2.4 The Computation of Meshing Efficiency

According to the computation mentioned before, setting the front transverse as reference, dividing the gear into m pieces along contact line and considering the meshing line made up of n segments, the instantaneous power of sliding friction loss of any micro gear piece can be expressed as:

$$P_{fkij} = \mu F_{ei}\Delta y\upsilon_{skij}. \tag{15}$$

In Eq. (15), υ_{skij} is the sliding velocity at any meshing point on the contact line, subscript $k = 1, 2, \ldots, N$, which means the code of meshing teeth, and subscript $i = 1, 2, \ldots, m$, $j = 1, 2, \ldots, n$, which indicate the position of the meshing point on the contact line and meshing line respectively. Thus, the power of the sliding friction of a single tooth at any meshing position is,

$$P_{fki} = \mu\sum_{\mathrm{i}=1}^{m} F_{ei}\Delta y\upsilon_{skij}. \tag{16}$$

Based on Eq. (16), the computation of total power of sliding friction at any meshing position is shown below:

$$P_{\Sigma fi} = \sum_{k=1}^{N} P_{fki}. \tag{17}$$

Therefore, if the sliding friction is the main consideration, the instantaneous meshing efficiency can be computed as:

$$\eta = 1 - \frac{P_{\Sigma fi}}{\mathrm{P}}. \tag{18}$$

3 CALCULATION RESULTS OF NUMERICAL EXAMPLE

Based on the calculation of meshing efficiency during the meshing process derived above, the computation was carried out with detail gear parameters.

Table 1 illustrates the reference and variable value of modulus, helical angle and radial modification. When one parameter varies, the other parameters remain consistent with the reference value, so the analysis and calculation with single variation is available. The output torque is 50000 N·mm and input speed is 955.4 r/min when the discussions concentrate on the variation of gear parameters. Table 2 expresses the different output torque and input speed while the gear parameters are the reference values in Table 1.

Fig. 6 shows the variation of the length of contact line, the unit load, relative sliding velocity and meshing efficiency along the meshing line while the gear parameters are reference values, and the maximum number of meshing teeth is two. In Fig. 6a, the right side of lines 1, 2, and 3 indicates the reference tooth in a meshing period, and the left side of the lines participates the tooth before the reference tooth. The line 1 means the reference tooth is partly

Table 1. *The reference value and variation of gear parameters*

Gear parameters	Teeth number of pinion z_1	Teeth number of gear z_2	Pressure angle α [°]	Modulus [mm]	Width of tooth [mm]	Helical angle β [°]	The radial modification coefficient of pinion (zero transmission)
Reference value	45	80	20	2	20	3	0
Variable value	45	80	20	1, 2, 3	20	1, 2, 3, 4	-0.3, -0.2, -0.1, 0.1, 0.2, 0.3

meshing in, line 2 is the process from the whole reference tooth coming into mesh to the meshing point arriving at the pitch point, line 3 indicates the meshing state of reference tooth from the meshing point in front transverse at pitch point to the end of a meshing period; the three meshing processes are recorded with red, green and black separately. It can be observed that the right black part in the third process is longer than the left, which illustrates the reference tooth meshing with single tooth near the end of the meshing period when the tooth before the reference tooth has meshed out, and this also can be known by the variation of length of contact line and unit load in Figs. 6c and d.

Table 2. *The different operation values*

Operation parameter	Output torque (constant input speed ω = 1500 r/min) [N·mm]	Input speed (constant output torque 30000 N·mm) [r/min]
Variable values	20000, 30000, 40000, 50000	1500, 2000, 2500, 3000

When the output torque is constant, the variation of the length of contact line is in contrast with the unit load. Fig. 6b shows the curve of meshing efficiency varying with the position of meshing point in the front transverse of the reference tooth along the meshing line. Referring to Fig. 6a, it can be observed that meshing efficiency is constant when there are two teeth meshing with the whole tooth. In this period, the contact lines of two teeth are at different sides of the pitch point, as the states illustrated in Figs. 5c and e, so the decrements of e_x in Fig. 5c is equal to the increments of e_x in Fig. 5e, which leads to the inverse variation of relative sliding velocity of two meshing teeth. Otherwise, the length of the contact line increases gradually partly during the mesh-in period in the front transverse because of the existence of helical angle, and the unit load decreases during this process. However, the meshing efficiency decreases in this period, meshing points are far from the pitch point, and the relative slide is serious. The same phenomenon also appears when the tooth before the reference tooth is meshing out, but the decrease of the length of contact line leads to the increase of meshing efficiency.

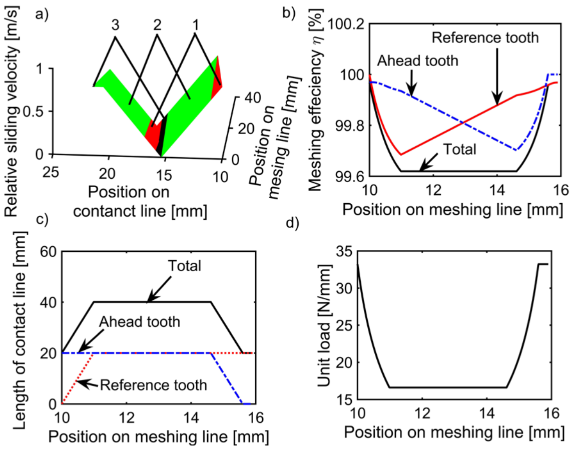

Fig. 6. *When the gear parameters are reference value; a) the variation of relative sliding velocity, b) the variation of meshing efficiency, c) the variation of total length of contact line, d) the variation of unit load*

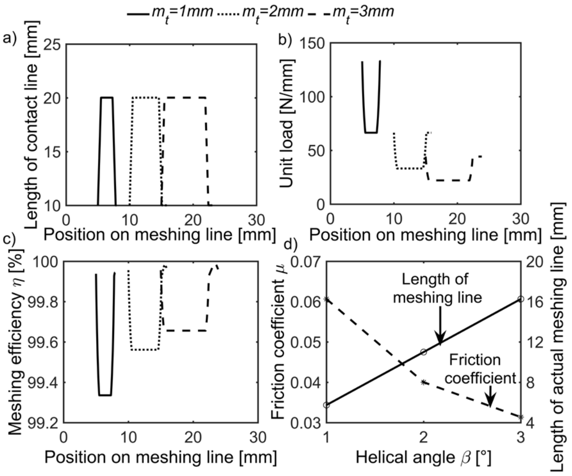

Fig. 7. *The variation with different modulus, a) length of contact line, b) unit load, c) meshing efficiency, d) coefficient of friction and the length of meshing line*

In Fig. 7 is shown the variation of the length of contact line, the unit load and the meshing efficiency along the meshing line with different modulus, for avoiding the zero-tooth thickness at the back transverse, the width of the tooth is 10 mm. In Fig. 7a, the maximum length of contact line is identical when the modulus varies, and the length of meshing line and the radius of base circle increases with the increase of modulus. Thus, the unit load decreases with the increase of modulus, and the maximum relative sliding velocity increases with the increase of modulus while the operation is fixed. In contrast, the increase of modulus leads to the decrease of positive force and increase of the relative radius of curvature, therefore, the coefficient of friction decreases with the increase of the modulus by Eq. (14). The influences of unit load and relative sliding velocity acting on the meshing efficiency are opposite, so the variation of meshing efficiency is mainly due to the change of the coefficient of friction with different modulus.

Fig. 8 indicates the variation of the length of contact line, the unit load, coefficient of friction, the length of meshing line and the meshing efficiency along the meshing line with different helical angle, and the partial detail figures are given in Figs. 8a to c. As Fig. 8a shows, the length of contact line increases with the increase of the helical angle when the whole tooth is meshing, and the unit load decreases with the increase of the helical angle in this period. Furthermore, the instantaneous minimum meshing efficiency increases with the helical angle, as Fig. 8c illustrated, but the mean meshing efficiency in a period decrease with the helical, as Table 3 shows. Because the length of actual meshing line lengthens with the helical angle, so does friction loss during meshing in and meshing out increases.

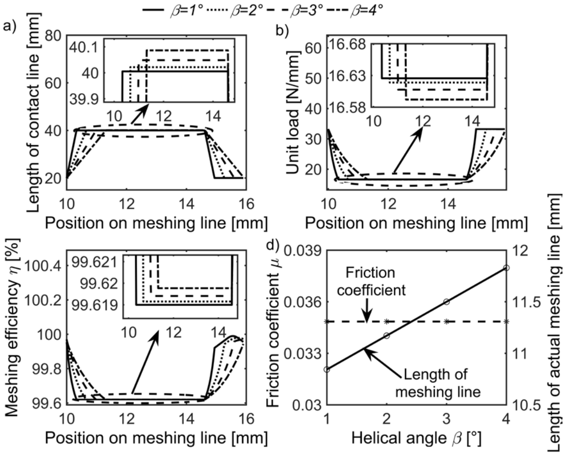

Fig. 8. *The variation with different helical angles, a) length of contact line, b) unit load, c) meshing efficiency, d) coefficient of friction and the length of meshing line*

The variations of the length of contact line, unit load, coefficient of friction, the length of meshing line and meshing efficiency with different radial modification of pinion are obtained in Fig. 9, and the radial modification of gear is opposite to the pinion. The radial modification affects the meshing start, meshing destination, and the relative meshing position between the meshing teeth in different meshing periods, so the variation of relative sliding velocity caused by the change of meshing position is the main influence factor of meshing efficiency. When the radial modification of pinion is negative, the smaller modification leads to the longer distance between the meshing start and the pitch point, which results in higher relative sliding velocity during the mesh-in process, so the meshing efficiency decreases, as shown in Fig. 9c. When the modification of pinion is positive, the bigger radial modification leads to the longer distance between the meshing destination and the pitch point, which results in higher relative sliding velocity, so the curve of the meshing efficiency during the mesh-out period appears as a wave trough when the modification is 0.3.

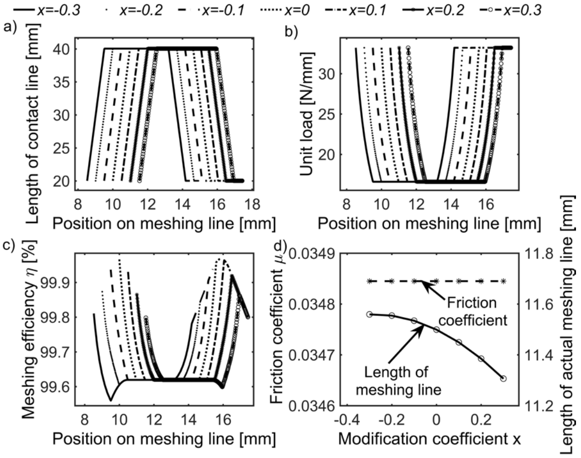

Fig. 9. *The variation with different modifications of pinion, a) length of contact line, b) unit load, c) meshing efficiency, d) enlarged figure of meshing efficiency, e) coefficient of friction and the length of meshing line*

As Figs. 10 and 11 show, the curves of meshing efficiency are provided by setting the output torque and input speed as variations. When the output torque is constant, the output power and the relative sliding velocity enlarge with the increase of the input speed, which means the increase of P and $P_{\Sigma fi}$ in Eq. (14), and the increments counteract with each other, so the variation of meshing efficiency at different input speeds is mainly caused by the variation of coefficient of friction under different input speeds. From Eq. (18), the coefficient of friction decreases along with the increase of input speed under the same output load, so the meshing efficiency increases along with the increase of input speed as shown in Fig. 10. When the input speed is fixed, the effect of the increase of output torque on the P and $P_{\Sigma fi}$ in Eq. (18) is the same as above, but the increase of output torque leads to the enlargement of friction coefficient, so the meshing efficiency decreases along with the increase of output torque at the same input speed as illustrated in Fig. 11. The variations of the meshing efficiency under different operations have good agreement with the trends of experimental results in [19].

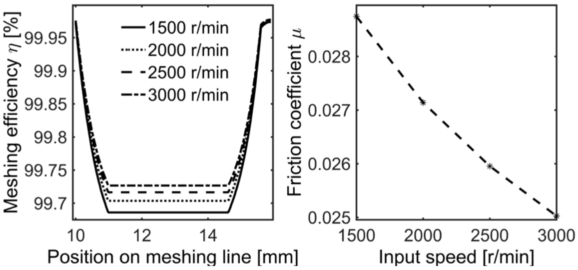

Fig. 10. *The variation of meshing efficiency at different input speeds; a) meshing efficiency, b) coefficient of friction*

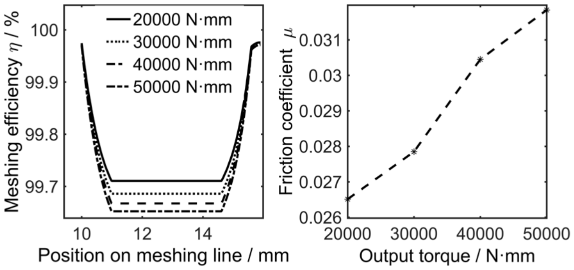

Fig. 11. *The variation of meshing efficiency at different out torques; a) meshing efficiency, b) coefficient of friction*

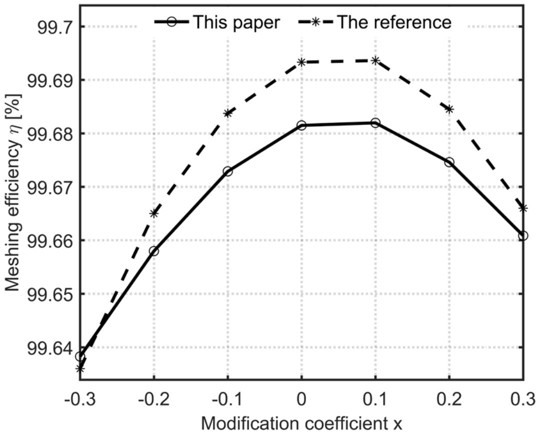

Fig. 12. *The comparison between calculating results in this paper and the results obtained by calculation in reference [4]*

To validate our calculation, the comparison between the results in this paper and the meshing efficiency calculated by the method in [4] is carried out, and the detail is presented in Fig. 12 and Table 3. Based on the same gear parameters, the variation of mean efficiency computed by our method is closed to the efficiency calculated according to the method in [4] with different modification coefficient, as shown in Fig. 12. Furthermore, the comparisons are carried out when different modulus, helical angle and operations are considered, the corresponding results are listed in Table 3. In Table 3, the η_f^c is the friction power loss computed in the current paper, η_f^r is the friction power loss calculated with the formula in reference [4], and E_r represents the percentage of the error between two differently calculated results.

Table 3. *Comparison of friction power loss obtained by two calculating methods in our paper and reference [4]*

Variation of parameter or operation		η_f^c [%]	η_f^r [%]	E_r [%]
Different modulus [mm]	1	0.556	0.534	0.041
	2	0.359	0.352	0.020
	3	0.280	0.276	0.015
Different helical angle [°]	1	0.310	0.306	0.013
	2	0.314	0.307	0.025
	3	0.319	0.307	0.039
	4	0.323	0.307	0.052
Different input speed [r/min]	1500	0.263	0.253	0.039
	2000	0.248	0.240	0.034
	2500	0.237	0.228	0.039
	3000	0.229	0.220	0.040
Different output torque [N·mm]	20000	0.242	0.233	0.039
	30000	0.263	0.253	0.039
	40000	0.278	0.268	0.039
	50000	0.291	0.280	0.039

4 CONCLUSION

The meshing efficiency of the proposed gear was calculated by dividing contact line and meshing line into micro-segments, and the variations of sliding velocity, contact line and unit load in a meshing period are illustrated. The variation of the length of contact line, unit load and instantaneous meshing efficiency are studied by considering the modulus, helical angles and modification coefficient as variables. In addition, the variations of meshing efficiency with different input speed and output torque were also discussed. The influences of parameters and operations on efficiency can be summarized as in Fig. 13.

It can be known from the calculation results that a larger modulus is helpful for heightening meshing efficiency while a heavier load decreases meshing efficiency, so a larger modulus can improve meshing efficiency under heavy load. A larger helical angle increases loss during mesh-in and mesh-out processes; therefore, choosing little helical angle can reduce friction loss while the anti-backlash requirement is satisfied. Modification may increase the relative slide in the mesh-in or mesh-out period, thus, little positive or negative modification should be considered in design. In contrast, maintaining high input speed is beneficial for heightening meshing efficiency.

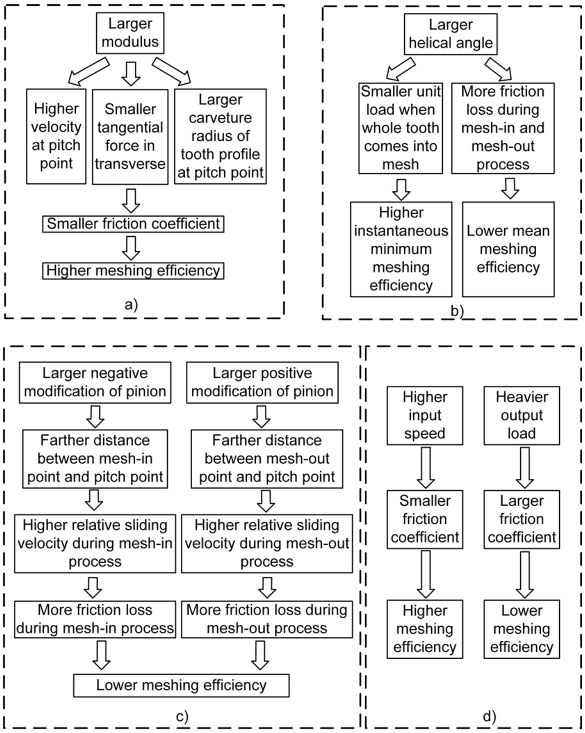

Fig. 13. *The influence of gear parameters and operations on meshing efficiency: a) modulus, b) helical angle, c) modification coefficient, d) operations*

Although the calculation of meshing efficiency presented in this paper is based on the new type of conical involute gear, the meshing process of helical gear is similar to the new type of conical involute gear, so the calculation can also apply in computing the meshing efficiency of helical gear when the influence of the tooth deformation on unit load is not taken into account.

5 ACKNOWLEDGEMENTS

This research received financial support from The National Natural Science Foundation of China (contract No. 51275538).

6 NOMENCLATURES

b	width of tooth, [mm]
F	positive force, [N]
F_{ei}	unit load, [N/mm]
i_0	transmission ratio
L	length of contact line, [mm]
l_0	distance between pitch point and reference point, [mm]
l_f	distance between meshing point in front transverse and reference point along meshing line when the tooth begins to mesh out, [mm]
l_s	distance between meshing point in front transverse and reference point along meshing line when the tooth begins to come into mesh, [mm]
l_{tf}	distance between virtual meshing point in front transverse and reference point along meshing line when whole tooth comes out of mesh, [mm]
l_{ts}	distance between meshing point in front transverse and reference point along meshing line when whole tooth just comes across pitch point, [mm]
l_x	distance between any meshing point in front transverse and reference point along meshing line, [mm]
M	output torque, [N·mm]
P	input power, [W]
P_f	power of sliding friction, [W]
p_b	base pitch in transverse, [mm]
r_b	radius of base circle of pinion, [mm]
v_s	relative sliding velocity, [m/s]
$\upsilon_{\Sigma c}$	the sum of the tangential velocity at pitch point, [m/s]
F_{bt}	the transverse force in tangent, [N]
y	the distance between the meshing point and front transverse along, [mm]
Δy	the length of micro-segment along contact line, [mm]
X_L	lubricant factor
z_1	teeth number of pinion
z_2	teeth number of gear
α_0	engagement angle at pitch circle, [°]
α_f	engagement angle in front transverse when the tooth begins to mesh out, [°]
α_s	engagement angle in front transverse when the tooth begins to come into mesh, [°]
α_x	engagement angle in front transverse at any moment, [°]
β_b	helical angle of base circle, [°]
η	meshing efficiency
μ	coefficient of friction between the meshing surfaces

ρ_c curvature radius of the tooth profile at the pitch point in transverse, [mm]

Subscripts

i the position of meshing point along contact line

j the position of meshing point along meshing line in front transverse

k the number of meshing teeth

7 REFERENCES

[1] Wang, G.J., Chen, X.A. (2008). *Variable tooth thickness cylindrical modified gear and its application in transmission device*. Patent CN 101285520A, China.

[2] Yu, L., Wang, G.J., He, L.L. (2015). The electrically controlling anti-backlash based on variable tooth thickness gear. *The International Conference on Gears*, p. 591-600.

[3] Kakavas, I., Olver, A.V., Dini, D. (2016). Hypoid gear vehicle axle efficiency. *Tribology International*, vol. 101, p. 314-323, **DOI:10.1016/j.triboint.2016.04.030**.

[4] Baglioni, S., Cianetti, F., Landi, L. (2012). Influence of the addendum modification on spur gear efficiency. *Mechanism and Machine Theory*, vol. 49, p. 216-233, DOI:10.1016/j.mechmach-theory.2011.10.007.

[5] Kolivand, M., Li, S., Kahraman, A. (2010). Prediction of mechanical gear mesh efficiency of hypoid gear pairs. *Mechanism and Machine Theory*, vol. 45, p. 1568-1582, **DOI:10.1016/j.mechmachtheory.2010.06.015**.

[6] Perić, S., Nedić, B., Trifković, D., Vuruna, M. (2013). An experimental study of the tribological characteristics of engine and gear transmission oils. *Strojniški vestnik - Journal of Mechanical Engineering*, vol. 59, no. 7-8, p. 443-450, **DOI:10.5545/sv-jme.2012.870**.

[7] Calì, M., Sequenzia, G., Oliveri, S.M., Fatuzzo, G. (2016). Meshing angles evaluation of silent chain drive by numerical analysis and experimental test. *Meccanica*, vol. 51, p. 475-489, **DOI:10.1007/s11012-015-0230-0**.

[8] Cheng, Y.B., Wang, Y., Li, L., Yin, S.B., An, L.C., Wang, X. P (2015). Design method of dual phase Hy-Vo silent chain transmission system. *Strojniški vestnik - Journal of Mechanical Engineering*, vol. 61, no. 4, p. 237-244, **DOI:10.5545/sv-jme.2014.2318**.

[9] Li, X.M., Sosa, M., Andersson, M., Olofsson, U. (2016). A study of the efficiency of spur gears made of powder metallurgy materials – ground versus super-finished surfaces. *Tribology International*, vol. 95, p. 211-220, **DOI:10.1016/j.triboint.2015.11.021**.

[10] Duhovnik, J., Zorko, D., Sedej, L. (2016). The effect of the teeth profile shape on polymer gear pair properties. Technical Gazette, vol. 23, no. 1, p. 199-207, **DOI:10.17559/TV-20151028072528**.

[11] Rossetti, A., Macor, A. (2013). Multi-objective optimization of hydro-mechanical power split transmissions. *Mechanism and Machine Theory*, vol. 62, p. 112-128, **DOI:10.1016/j.mechmachtheory.2012.11.009**.

[12] Petry-Johnson, T.T., Kahraman, A., Anderson, N.E., Chase, D.R. (2007). An experiment investigation of spur gear efficiency. *Journal of Mechanical Design*, vol. 130, no. 6, p. 1-10, **DOI:10.1115/1.2898876**.

[13] Michlin, Y., Myunster, V. (2002). Determination of power loss in gear transmissions with rolling and sliding friction incorporated. *Mechanism and Machine Theory*, vol. 37, no. 2, p. 167-174, **DOI:10.1016/S0094-114X(01)00070-2**.

[14] Xu, H., Kahraman, A., Anderson, N.E., Maddock, D.G. (2007). Prediction of mechanical efficiency of parallel-axis gear pairs. *Journal of Mechanical Design*, vol. 129, no. 1, p. 58-68, **DOI:10.1115/1.2359478**.

[15] Xu, H. (2005). *Development of a Generalized Mechanical Efficiency Prediction Methodology for Gear Pairs*. PhD Thesis, Ohio State University, Columbus.

[16] Wang, C., Fang, Z.D, Jia, H.T. (2009). Calculation of sliding friction loss of helical gear. *Journal of Yanshan University*, vol. 33, no. 2, p. 99-102, **DOI:10.3969/j.issn.1007-791X.2009.02.002**.

[17] Wang, C., Gao, C.Q., Cui, H.Y. (2012). The selection of helical cylindrical gear parameters based on meshing efficiency. *Journal of Yanshan University*, vol.36, no. 2, p. 126-130, **DOI:10.3969/j.issn.1007-791X.2012.02.006**.

[18] Marques, P.T.M., Martins, R.C., Seabra, J.H.O. (2016). Power loss and load distribution models including frictional effects for spur and helical gears. *Mechanism and Machine Theory*, vol. 96, p. 1-25, **DOI:10.1016/j.mechmachtheory.2015.09.005**.

[19] Aarthy, V., Tech, B. (2009). *An experimental investigation of helical gear efficiency*. MSc Thesis, Ohio State University, Columbus.

[20] Seetharaman, S., Kahraman, A. (2009). Load-independent spin power losses of a spur gear pair: model formulation. *Journal of Tribology*, vol. 131, no. 2, p. 1-11, **DOI:10.1115/1.3085943**.

[21] Luke, P., Olver, A.V. (1999). A study of churning losses in dip-lubricated spur gears. *Proceedings of the Institution of Mechanical Engineers, Part G: Journal of Aerospace Engineering*, vol. 213, no. 5, p. 337-346, **DOI:10.1243/0954410991533061**.

[22] Diab, Y., Ville, F., Houjoh, H., Sainsot, P., Velex, P. (2005). Experimental and numerical investigations on the air-pumping phenomenon in high-speed spur and helical gears. *Proceedings of the Institution of Mechanical Engineers, Part C: Journal of Mechanical Engineering Science*, vol. 219, no. 8, p. 785-800, **DOI:10.1243/095440605X31652**.

[23] Benedict, G.H., Kelley, B.W. (1961). Instantaneous coefficients of gear tooth friction. *ASLE Transactions*, vol. 4, no. 1, p. 59-70, **DOI:10.1080/05698196108972420**.

[24] O'Donoghue, J.P., Cameron, A. (1966). Friction and temperature in rolling sliding contacts. *Tribology Transactions*, vol. 9, no. 2, p. 186-194, **DOI:10.1080/05698196608972134**.

[25] Drozdov, Y.N., Gavrikov, Y.A. (1968). Friction and scoring under the conditions of simultaneous rolling and sliding of bodies. *Wear*, vol. 11, no. 4, p. 291-302, **DOI:10.1016/0043-1648(68)90177-4**.

[26] Martin, K.F. (1978). A review of friction predictions in gear teeth. *Wear*, vol. 49, no. 2, p. 201-238, **DOI:10.1016/0043-1648(78)90088-1**.

[27] Kumar, P., Jain, S.C., Ray, S. (2001). Study of surface roughness effects in elastohydrodynamic lubrication of

rolling line contacts using a deterministic model. Tribology International, vol. 34, no. 10, p. 713-722, **DOI:10.1016/S0301-679X(01)00066-4**.

[28] Cioc, C., Cioc, S., Moraru, L., Kahraman, A., Keith, T.G.Jr. (2002). A deterministic elastohydrodynamic lubrication model of high-speed rotorcraft transmission components. *Tribology Transactions*, vol. 45, no. 4, p. 556-562, **DOI:10.1080/10402000208982587**.

[29] ISO/TR 13989-1:2000(E). *Calculation of Scuffing Load Capacity of Cylindrical, Bevel and Hypoid Gears – Part 1: Flash Temperature Method.* International Organization for Standardization, Geneva.

[30] Martinsa, R., Seabra, J., Brito, A., Seyfert, Ch., Luther, R., Igartua, A (2006). Friction coefficient in FZG gears lubricated with industrial gear oils: Biodegradable ester vs. mineral oil. *Tribology International*, vol. 39, no. 6, p. 512-521, **DOI:10.1016/j.triboint.2005.03.021**.

[31] Martins, R.C., Cardoso, N.F.R., Bock, H., Igartua, A. Seabra, J.H.O. (2009). Power loss performance of high pressure nitrided steel gears. *Tribology International*, vol. 42, no. 11-12, p. 1807-1815, **DOI:10.1016/j.triboint.2009.03.006**.

[32] Fernandes, C.M.C.G, Martins, R.C., Seabra, J.H.O. (2014). Torque loss of type C40 FZG gears lubricated with wind turbine gear oils. *Tribology International*, vol. 70, p. 83-93, **DOI:10.1016/j.triboint.2013.10.003**.

[33] Magalhães, L., Martins, R., Locateli, C., Seabra, J. (2010). Influence of tooth profile and oil formulation on gear power loss. *Tribology International*, vol. 43, no. 10, p. 1861-1871, **DOI:10.1016/j.triboint.2009.10.001**.

Strojniški vestnik - Journal of Mechanical Engineering 63(2017)5, 331-348
© 2017 Journal of Mechanical Engineering. All rights reserved.
DOI:10.5545/sv-jme.2017.4324
Review Scientific Paper
Received for review: 2017-01-13
Received revised form: 2017-03-24
Accepted for publication: 2017-04-05

Machine-Vision-Based Human-Oriented Mobile Robots: A Review

Miha Finžgar* – Primož Podržaj
University of Ljubljana, Faculty of Mechanical Engineering, Slovenia

In this paper we present a study of vision-based, human-recognition solutions in human-oriented, mobile-robot applications. Human recognition is composed of detection, tracking and identification. Here, we provide an analysis of each step. The applied vision systems can be conventional 2D, stereo or omnidirectional. The camera sensor can be designed to detect light in the visible or infrared parts of the electromagnetic spectrum. Regardless of the method or the type of sensor chosen, the best results in human recognition can be obtained by using a multimodal solution. In this case, the vision system is enhanced with other forms of sensory information. The most common sensors are laser range finders, microphones and sonars. As medicine is expected to be one of the main fields of application for mobile robots, we give it special emphasis. An overview of current applications and proposal of potential future applications are given. Without doubt, properly controlled mobile robots will play an ever-increasing role in the future of medicine.

Keywords: mobile robot, machine vision, human recognition, image-processing algorithms, medical applications, review, overview

Highlights

- *An overview of vision-based, human recognition solutions in human-oriented, mobile-robot applications is presented.*
- *A comparison of conventional 2D, stereo and omnidirectional vision systems is made.*
- *The advantages of multimodal systems over vision-only systems are described.*
- *A table of overviewed hardware and software solutions together with their performance is provided in order to make a comparison between various systems easier.*
- *The most promising and relevant mobile-robot applications from the field of medicine are discussed.*

0 INTRODUCTION

Mobile robots are receiving more and more attention because of their ability to move around in a real-world environment and to perform various tasks. These two characteristics make mobile robots suitable for use in numerous industrial and domestic applications (e.g., personal assistance, guidance, surveillance, transportation, cleaning). Furthermore, they can operate in environments that are hostile or even inaccessible to humans. Human-oriented mobile robots are becoming increasingly important since the need for health-based assistance is increasing for the growing number of elderly and/or chronically ill people. Mobile robots could offer assistance and reliable health monitoring and therefore improve people's quality of life. These robots could also be used in telemedicine, which would not only reduce the costs needed to travel to outpatient-based doctors and the number of missed working days, but also save patients' time [1]. On the other hand, even the mere presence of a mobile robot can have a positive effect on people's well being [1].

In general, robotic applications in healthcare and social care can be classified into two main groups [2]: traditional robots intended for (telerobotic) surgery and rehabilitation and robots supporting "softer" human-robot interaction tasks such as logistics, telepresence, companionship, education of children with special needs and motivational coaching. Mobile examples include HelpMate [3] used in the transportation of supplies to healthcare staff and PR7 [4] used for telecommunication. More recent mobile-robot applications are dealing with the assistance of elderly people [5], support for autism diagnosis and intervention [6] and assessments of people's physiological state [7]. However, the challenges remain. One of the most important is human-robot interaction (HRI). In order to make it as natural as possible and to ensure reliable execution of the mobile robots' tasks these systems should be autonomous, robust, fast, non-contact and, most importantly, safe. These characteristics are needed for unbiased, real-time measurements in different situations (occlusions, varying illumination, etc.). Moreover, it is necessary for the mobile robots to provide only the tasks for which they were built and not to keep people under surveillance and/or disturb their privacy [8]. Mobile robots' functions in general include 1) reaching the goal and 2) performing certain tasks. In order to reach the goal, quickly acquired, low-resolution data about the mobile robot's environment is needed, while for the task execution, more detailed data is required [9]. For mobile robots to be efficient during their interactions with humans, the implementation of machine vision is essential. Additionally, visual systems have an important role in medicine for diagnosing [10], screening and monitoring [11]. This

---

*Corr. Author's Address: University of Ljubljana, Faculty of Mechanical Engineering, Aškerčeva c. 6, SI-1000 Ljubljana, Slovenia, miha.finzgar@fs.uni-lj.si

allows mobile robots to not only recognize humans and avoid obstacles but also to perform certain healthcare tasks.

In order to assess the feasibility of implementation with respect to different visual systems for assessments of human physiology on mobile robots it is of great importance to review the proposed vision-based, human-recognition solutions in human-oriented mobile robots. In the first section, each step of the human recognition in mobile robots is addressed. In the second section an overview of the applied sensor modalities that offer human recognition are presented. This section is divided into two parts: the first one presents vision-only-based solutions, while the second one presents multimodal solutions. The third section presents the proposed applications of human-oriented mobile robots. The fourth section includes a short discussion, with the authors' views on the challenges and available solutions regarding the implementation of mobile robots in any real-world environment, with an emphasis on performing health-care tasks.

1 HUMAN RECOGNITION

The crucial characteristic of mobile robots needing to work in a human environment is the ability to recognise people. This is important for safety reasons, the successful performance of the mobile robots' tasks and a natural HRI. Human recognition consists of 3 basic steps **[12]**: detection, tracking (localisation) and identification.

Humans can be detected with vision-based, invisible-band, sensor-based and sensor fusion-based approaches **[13]**. It can involve image-background subtraction in cases when the mobile robot (together with the camera(s) mounted on it) is not moving **[14]**, but most commonly it employs colour-based feature detection, shape- or model-based approaches and machine-learning-based approaches. Colour-based approaches use the predefined colour models of human skin and fit the pixels to these models. These approaches are fast, but are at the same time susceptible to illumination variation and changes to a person's position relative to the mobile robot's vision system **[15]**. Additionally, they provide false-positive detections due to skin-coloured, static background regions or objects **[16]**. In order to differentiate between real skin and a skin-like coloured object, the size of the detected object and the object's width-to-height ratio can be used **[14]**. Model-based approaches use various parameters that describe the shape and/or motion of the target. They are usually computationally more demanding and require constraining the dynamics of the system, but provide additional pieces of information regarding the tracked object's position and the correspondence of specific parts of the tracked objects with the actual image. The speed and accuracy of these approaches are affected by the initial conditions and any feature variances **[15]**. Additionally, the detection of facial features strongly depends on the size of the entire face blob **[17]**. When it comes to face detection algorithms, interested reader can refer to the article written by Zafeiriou et al. **[18]**. It offers a thorough description of face detection algorithms together with their comparison, it presents benchmarks and evaluation metrics and it also discusses future challenges in the field. Machine-learning-based approaches require a predefined set of images and their computational cost increases with increasing image/video resolution **[15]**.

Various approaches can be used for the tracking: mean-shift and its variant the continuously adaptive mean-shift algorithm (CamShift), optical flow (e.g., Lucas-Kanade method), particle filters, Kalman filters, multiple hypothesis tracking, etc. The performance of tracking approaches depends on the environment. For example, CamShift can provide false tracking if the background colour is similar to the target's colour **[19]** or when the illumination is too intense **[20]**. The Lucas-Kanade approach has difficulties in cases where there is a lot of movement near the target or when the target moves too far from its initial position **[20]**. Additionally, if the mobile robot is not moving there are no cues for optical flow computation. This disadvantage can be overcome using a motion-dependent approach **[21]** in which background subtraction is performed when the robot is not moving, with an optical-flow-based approach being used otherwise (the switching is based on the processing load and the mobile robot's movement). A particle filter might offer the best results in comparison to the Lucas-Kanade and CamShift approaches due to its non-parametricity and robustness to background colour distribution and movements in the background **[20]**. In the case of multiple humans a set of independent particle filters can be used (each human appearing in the scene for the first time is detected, while previously detected ones continue to be tracked) **[22]**. An important characteristic of independent tracking filters is their computational efficiency, which allows real-time tracking, but their performance deteriorates if the tracked objects are too close to each other **[22]**. The cost effectiveness of the Kalman filter can be increased by applying the filter only to the region of interest (ROI) and not over the entire image **[23]**. Kalman filters are constrained by linear or

Gaussian assumptions, whereas particle filters are not. However they are, in general, computationally more demanding [24]. The ground truth for tracking can be obtained by using ceiling-mounted cameras ([24] and [25]) or by manual annotation [26]. The tracking is more successful if the motion of the moving target is predicted [27]; the state-estimation problem can be solved in a 2D image plane [28]. Classic approaches to human recognition deal separately with detection and tracking, which results in the potential loss of information as well as in an increased computational load [29]. The other approaches, known as track-before-detect or unified tracking [30], deal with detection and tracking simultaneously.

In general, human identification can be most successfully achieved using biometrics, which is based on measurements of physiological and behavioural characteristics [31]. Human identification by mobile robots is, however, based mostly on colour features [12], texture features or combinations of both [32]. The latter offers high human-recognition rates as well as real-time performance in crowded environments; a combination of features offers better results than feature used on its own [32]. An example of the colour-feature approach is a comparison of the colour histograms of people's clothes [24]. However, this approach does not work in environments in which human apparel is identical (e.g., in industrial and healthcare environments) and it does not offer an instant daily identification of a single person, since human apparel is usually changing daily. On the other hand, this approach can be useful for emergency personnel following applications [16].

Human recognition in real-world applications is very challenging due to varying illumination, varying appearances, directions and behaviours of humans, background variations, limited time for computation [13] and vibrations of the mobile robot [33], which are due to uneven floors or mobile-robot construction deficiencies. In the outdoor environment, there are additional challenges, such as weather and terrain diversity [34]. Often, the robust solutions for the aforementioned challenges are not applicable to mobile robots. For example, occlusions can be easily solved by implementing a camera mounted above the observed environment [35] or by using multiple cameras [36], which is not always possible and/or desirable. The effect of occlusions on the correct tracking rate in mobile robots is therefore handled by applying kinematic models to each tracked object (implicit solution) [37] or by predicting human behaviour in detected occlusions (explicit solution) [22]. In order to achieve the best human recognition possible it is important to choose an appropriate number of features, while at the same time achieving real-time execution of the algorithms programmed in the mobile robots.

Table 1. *Reviewed literature*

Research	Hardware	Studied environment	Applied algorithms	Algorithms' performance
Böhme et al. [14]	Extended B21 RW1, IS Robotics with IR layer, 2 sonar sensors, omnidirectional camera, two frontally aligned colour cameras, binaural auditory system $f_{system} = 0.5$ Hz	indoor environment (home store)	• updated motion-based foreground-background segmentation [37] • binaural sound localization based on inter-aural time differences and spikes [38] and [39] • upper body contour modelling • skin colour (dichromatic r-g) detection [40] • CCNNW-based face detection [41] using public data set [42] • dynamic neural field for final selection • tracking: condensation algorithm [43]	no quantitative evaluation
Fritsch et al. [44]	Bielefeld robot companion – BIRON (based on ActiveMedia Pioneer PeopleBot) with Sony EVI-D31 PT camera, two AKG far-field microphones and a SICK LRF $f_{system} = 5$ Hz $f_{microphone} = 5.5$ Hz $f_{LRF} = 4.7$ Hz	indoor environment (office); robot is tracking a target human, who at one point is turned away from the robot, is not speaking and his legs are occluded	• face detection (Viola Jones) [45] • mixture of Gaussians-based colour (LUV) representation for torso recognition • Cross-Power Spectrum Phase Analysis based sound source localization [46] • leg detection [47] • custom simple cue fusion • multi-modal anchoring for data fusion extended by supervising module [47] • attention system for focusing the mobile robot on target human [48]	tracking: $SR \approx 80$ %

Cielniak and Duckett [12]	Pan-tilt colour camera Canon VC-C4R, IR camera NEC Thermal Tracer TS7302 f_{camera} = 5 Hz	indoor environment (office corridor); mobile robot was following the corridor with 10 walking humans;	• thresholding and connectivity- plus size-based segmentation for human detection (thermal images) • temperature and colour (HSV) statistics (first two moments) • human identification: k-NN classifier, Bayes' classifier and dynamic identification	classification (dynamic version of Bayes' classifier): $SR_{thermal}$ = 69.84 % SR_{colour} = 89.42 % $SR_{combination}$ = 94.04 %
Wilhelm et al. [49]	mobile robot B21 RWI, IS Robotics with omnidirectional camera Sony DWW VL500, 24 sonar sensors in 2 layers, two frontal cameras on PT unit	indoor environment (home store)	• skin colour (dichromatic r-g) detection using look up table with manually classified colour pixels [50] • automatic white-balance algorithm for colour calibration • sonar-based distance measurements • face detection (Viola-Jones) [45] • tracking: condensation algorithm [43]	no quantitative evaluation
Treptow et al. [51]	ActivMedia PeopleBot mobile robot with NEC Thermal Tracer TS730 f_{camera} = 15 Hz	indoor environment (unconstrained corridor and laboratory room) with 18 different humans; 1) person following; 2) corridor following; 3) stationary robot	• elliptic contour model for human detection similar to [43] • integral image features model based on Viola-Jones approach [45] • cascaded model evaluation for combining both models • tracking: set of independent particle filters (multiple humans)	tracking (single human): $ACC_{object\ count} \approx$ 92 % $ACC_{object\ area} \approx$ 78 % tracking (multiple humans): $ACC_{object\ count} \approx$ 84 % $ACC_{object\ area} \approx$ 64 % All results are for the combination of contour and feature-based model
Martin et al. [25]	Home Robot System – HOROS with fish-eye omnidirectional camera, SICK LRF and 16 sonar sensors Pentium M 1.6 GHz f_{sonar} = 10 Hz f_{LRF} = 10 Hz f_{camera} = 7 Hz	indoor environment (hallway); people walking past the mobile robot performing survey task	• heuristic method for detection of leg-pairs using LRF scans [47] • distance measurements on sonar scans of leg profiles • skin-colour (dichromatic r–g) detection [49] • tracking: condensation algorithm [43]	tracking: SR = 93 % FPR = 25 % $CPU\ load$ = =(40 to 50) %
Kim and Suga [33]	wheelchair mobile robot with omnidirectional camera f_{camera} = 15 fps	indoor environment (undefined place with undefined moving object and humans)	• expansion of grayscale omnidirectional image into panoramic • Lucas-Kanade optical flow method [52] • estimation of FOE and FOC • detection of moving objects using the evaluation value	tracking: $ERR_{OF\ min}$ = 2.15 % (rotation) $ERR_{OF\ max}$ = 3.86 % (right turn)
Chang et al. [53]	Kondo KHR-1 with webcam f_{camera} = 3 fps	indoor environment (office?); 4 individual humans	• skin-colour (dichromatic r-g) detection • hand-shape recognition (Hu moment invariants [54]) • tracking: active contour model with mean-shift, active contour model only	hand shape recognition: SR = 96.8 %
Vadakkepat et al. [55]	Magellan Pro with Sony EVI-D30 pan-tilt camera, 16 sonar and tactile sensors Pentium II	indoor environment (office?); 6 individual humans	• skin-colour (YCbCr and YUV) features and geometry features for face detection • tracking: CamShift [56] (HSV colour space)	tracking: SR = 84.2 % (YCbCr colour space) SR = 89.8 % (UV colour space)
Bellotto and Hu [24]	Pioneer mobile robot with PTZ colour camera and SICK LRF Pentium III 800 MHz, 128 MB RAM f_{LRF} = 5 Hz f_{camera} = 10 Hz f_{system} = 5 Hz	indoor environment (laboratory, corridor, office); 1) human following through different rooms, 2) 3 humans walking in front of the mobile robot or hiding	• leg detection based on the recognition of their typical patterns • Viola-Jones' face detection [57] • state prediction model [58] based on CV model • tracking: unscented Kalman filter [59] • human identification: comparison of colour histograms of human clothes [60] and NN data (multiple humans)	no quantitative evaluation

Fernandez-Caballero et al. [21]	MoviRobotics mSecurit mobile robot with thermal IR camera, PTZ dome camera, ultrasound sensors Intel Celeron M 600 MHz, 1 GB RAM $f_{IR\ camera} = (5 \text{ to } 6)$ fps $f_{system} = 6$ Hz	indoor (undefined) and outdoor (?) environment plus chosen images from OTCBVS data set [61]	• normalization and thresholding for human candidates' blob detection • image subtraction or Lucas-Kanade optical flow method [52] (depending on mobile robot's motion)	human detection (image subtraction approach): $TPR = (83.09 \text{ to } 90.94)$ %; $PR = (98.62 \text{ to } 100)$ % (robot acquired images) $TPR = (72.52 \text{ to } 82.54)$ %; $PR = (98.62 \text{ to } 100)$ % (OTCBVS data set) human detection (optical flow approach): $TPR = (79.62 \text{ to } 98.57)$ %; $PR = (94.59 \text{ to } 100)$ % (robot acquired images)
Cielniak et al. [22]	ActivMedia PeopleBot mobile robot with PTZ camera Canon VC-C4R, NEC Thermal Tracer TS7302 0.85 GHz (robot); 2.00 GHz (PC) $f_{camera} = 15$ Hz (both cameras)	indoor environment (a corridor and a laboratory room); 1) humans walking in front of the 1.1) non-moving robot and 2.1) moving robot	• elliptic contour model adaptive colour (RGB) model based on the first three moments of colour distribution [62] • classification algorithm occlusion handling: combination of thermal and colour features determined by AdaBoost [63] • (used in occlusion handling) • tracking: particle filter/set of independent particle filters	occlusion classification: $SR_{thermal} = (76.4 \pm 4.5)$ % $SR_{colour} = (69.0 \pm 1.9)$ % $SR_{combination} = (89.4 \pm 2.5)$ % $t_{p\_robot} = 68.8$ ms $t_{p\_PC} = 25.9$ ms (for 1000 samples using colour representation using first three moments)
Kang et al. [13]	Dasa Robot Tetra-DS with Point Grey LadyBug2 camera Intel Core2 Quad Q9400 2.66 GHz, 4 GB RAM, Nvidia GTX460 $f_{camera} = 30$ fps $f_{system} = (9.3 \text{ to } 12.8)$ fps	outdoor environment; moving and non-moving humans (occlusions, different positions relative to the robot), cars and other objects	• combined local-global optical flow method (based on global Horn's approach [64] and Lucas-Kanade approach [52]) computed on GPU • detection of ROIs using parallax flow • shape-based human detection (based on parallax flow estimation, Chamfer distance and HOG-based SVM classifier)	human detection: $TPR_{mid\ range} = 69.14$ % $TPR_{near\ range} = 98.36$ % $t_p = (78 \text{ to } 108)$ ms
Alvarez-Santos [32]	Pioneer P3DX mobile robot, SICK-LMS200 laser scanner, PointGrey Chameleon CMLN-1352C with Fujinon Fujifilm Vari-focal CCTV lens Intel Core2 Duo P8600 (2.4 GHz), 4 GB RAM	indoor environment (office); 1) varying lightning conditions (20-400 lx, shadows, reflections), 2) walking humans trying to distract the mobile robot system; indoor environment (museum): crowded, various light sources, reflective and uneven floor	• human detector based on HOG [65] • torso detection based on the extensive initial pool of colour (H1L1S1, L2AB, YCbCr, H2S2V, greyscale) and texture features (local binary patterns: classic [66], census [67], centre-symmetric [68] and semantic [69], edge density based on Canny edge detector [70], HOG [65], MPEG-7 edge histogram inspired descriptor [71]) • leg detection using laser scanner • sensor fusion at the tracker stage	$F_{max} = 0.987$ (combinations of 8 features) $t_p = 20$ ms
Baltzakis et al. [15]	no information 2.8 GHz, 4 GB RAM $f_{system} = 16$ Hz (maximum value)	indoor environment (office); 1) a single human and 2) multiple humans; indoor environment (exhibition centre): human and tour-guide robot interaction scenario	• background subtraction (28) and skin-colour (YUV) detection (face, hand) based on [72] and [73] • tracking: propagated pixel hypotheses algorithm [74] extended by an incremental probabilistic classifier • Viola-Jones' boosted cascade detector [57] (facial features) with anthropometric constraints • tracking: feature-based;(eyes, mouth) using normalized cross-correlation as similarity measure	tracking: $TPR_{max} = 95.09$ %; FPR = 0.22 % (mouth) $TPR_{max} = 95.58$ %; FPR = 0 % (left eye) $TPR_{max} = 93.30$ %; FPR = 0.22 % (righty eye)

Fotiadis et al. [34]	Robotnik Summit XL with a pan-tilt zoom camera Point Grey Firefly MV (60 Hz) and a LRF Hokuyo UTM-30LX-EW $f_{LRF} = 40$ Hz $f_{camera} = 60$ fps $f_{system} = 8$ Hz	indoor environment (gymnasium); 1) one human passed by non-moving mobile robot 2) random number of humans passed by moving mobile robot; outdoor environment: humans walking in front of moving mobile robot	• jumping distance segmentation, novel feature set for feature extraction and real AdaBoost classifier (LRF data) • HOG descriptor **[65]** with SVM classifier **[75]** (visual data)	indoor: $ACC_{max} = 99.88$ % $TPR_{max} = 95.20$ % $TNR_{max} = 99.76$ % (all Bayesian/mean fusion + adaptive projection) outdoor: $ACC_{max} = 99.63$ % (Bayesian/mean fusion + fixed-size projection) $TPR_{max} = 93.01$ % (maximum fusion; adaptive projection) $TNR_{max} = 99.99$ % (Bayesian/mean fusion + fixed-size projection)
Zhang et al. [26]	Pioneer 3-DX mobile robot with ASUS Xtion Pro Live RGB-D camera Intel Core i7 2.0 GHz (quad core) and 4 GB RAM (DDR3) $f_{system} =$ (7 to 15) fps	indoor environment (laboratory); 1) humans walking with simple trajectories, 2) humans lifting humanoid robots and putting them away, 3) humans picking up objects, exchanging them and delivering them to other rooms	• separation of candidate point clusters using RANSAC **[76]** guided with prior-knowledge • candidate detection based on DOI • cascade of detectors **[77]** using height-, size-, surface- and HOG-based detector • DAG-based framework (human object classification **[78]**, data association, matching, tracking: extended Kalman filter **[79]**)	multiple object tracking: $ACC_{max} = 95.39$ % $FNR_{min} = 2.77$ % $FPR_{min} = 1.10$ %
Susperregi et al. [16]	RMP Segway mobile platform with Kinect (4 Hz), Heimann HTPA thermal sensor and Hokuyo UTM-30LX laser $f_{Kinect} = 30$ fps $f_{system} = 4$ Hz	indoor environment (museum); various lightning conditions, people naturally walking in front of the camera	• leg detection **[80]** • colour-based (RGB) vest detection • temperature-based human detection (thermal vision) • tracking: SIR particle filter **[81]**	$ERR_{estimation\ min} =$ (17.44 ± 22.54)° $ERR_{estimation\ min} =$ (0.10 ± 0.31) m (both results are obtained with following weighted combination of sensory data: 0.15× leg detection, 0.7× vest detection, 0.15× thermal detection)
Susperregi et al. [82]	RMP Segway mobile platform with Kinect, Heimann HTPA thermal sensor and Hokuyo UTM-30LX laser $f_{Kinect} = 30$ fps $f_{system} = 1$ Hz	indoor environment (manufacturing shop floor and museum); varying illumination conditions and human-like objects	• 23 different image transformations • 5 supervised machine-learning approaches (IB1 **[83]**, Naïve-Bayes **[84]**, Bayesian network **[85]**, C4.5 **[86]**, SVM) with hierarchical classifier **[87]**	human detection: $ACC = 96.74$ % $FPR = 4.64$ % $FNR = 1.88$ % $PR = 95.36$ % $TPR = 98.07$ %
Petrović et al. [23]	unknown mobile robot with Point Grey Bumblebee XB3 $f_{camera} = 12$ Hz $f_{system} = 4$ Hz	indoor (office) and outdoor (meadow) environment; a single human walking in front of the robot	• disparity map segmentation (connected pixel labelling **[88]**) • feature-based (2D - Hu moment invariants **[54]**, 3D – object's height and width) object classification • tracking: modified Kalman filter	no quantitative data $t_p = 81$ ms $t_{lat} = 100$ ms (both results for case of sequential processing + distributed computing)
Mehdi et al. [8]	Autonomous Robot for Transport and Service - ARTOS, with LRF range finder, RFID reader, PTZ camera, sonar and tactile sensors	simulated indoor environment (apartment); a single human	• MDP-based human search similar to **[89]** and **[90]** • face detection using Haar cascade classifier **[91]** standing posture detection based on HOG **[65]**)	no relevant quantitative data
Ćirič et al. [92]	DaNi mobile robot with FLIR E50 thermal camera 400 MHz, 128 MB RAM (embedded operation) + 256 MB RAM (storage) $f_{camera} = 60$ Hz	indoor environment (an unconstrained corridor and a hall); humans walking in front of the robot during 1) corridor following, 2) person following, 3) non-moving robot	• thermal image threshold segmentation optimized with genetic algorithm • feature detection (Hu moment invariants **[54]**) • SVM classification **[75]**	classification: $SR = 97.3$ %

Hu et al. [93]	Pioneer3DX mobile robot with RGB-D camera, LRF and sonar sensor $f_{camera} = 30$ fps	indoor environment (T-shaped corridor); 8 different humans leading the robot from starting to the end position	• human leg tracking using adaptive breakpoint detector [94] • estimation of human walk model • tracking: modified mean-shift [95] with depth information	anticipative front following: $t = (54.2 \pm 19.6)$ s $d_{robot} = 16.94 \pm 3.80$ m $d_{human} = (21.29 \pm 6.83)$ m passive front following: $t = (49.1 \pm 26.0)$ s $d_{robot} = (16.41 \pm 3.81)$ m $d_{human} = (19.49 \pm 5.71)$ m combined strategy: $t = (33.7 \pm 4.5)$ s $d_{robot} = (15.06 \pm 1.51)$ m $d_{human} = (17.40 \pm 0.80)$ m (no significant differences between anticipative and passive back and side following)
Ali et al. [20]	Pioneer 3AT mobile robot with stereo camera and 16 sonar sensors Intel Core i3 2.4GHz, 4 GB RAM	indoor (laboratory) and outdoor environment (corridor, natural environment); multiple humans	• Haar-based human upper-body and face detection [91] • manual selection of target person • tracking: CamShift [56], Lucas-Kanade [52], particle filter [96] • Kalman-filter-based estimation and correction • stereo correspondence and linear triangulation (for target positioning)	$t_{p\_meanshift} = 0.02649$ s $t_{p\_LK} = 0.02712$ s $t_{p\_PT} = 0.02891$ s
Bayram et al. [19]	modified Turtlebot II mobile robot with two Kinect modules, microphone array 2 netbooks with Intel Celeron 1.5GHz (dual core), 4 GB RAM $f_{Kinect} = 10$ fps $f_{microphone} = 100$ Hz	indoor environment (laboratory); 1) moving humans with changing face direction towards the mobile robot; various lightning conditions and background variation (vision only) 2) one human, moving and speaking simultaneously 2) two humans speaking 2.1) with each other and 2.2) independently (vision and audio) 3) speaking human not present in robot's eye-sight (audio only)	• GEVD-MUSIC [97] • face detection • eyes detection based on Haar cascade classifier • skin-color (YCbCr) detection [98] • particle-filter based sensor fusion • tracking: CamShift [99]	face detection: $PR = 98$ % $TPR = 94$ % audio-visual human tracking: $ERR_{localization} = 1.86°$ (one human) $ERR_{localization} = 1.40°$ (two humans)

Legend: ACC – accuracy [%], ACC_{max} – maximum accuracy [%], $ACC_{object\ area}$ – accuracy of object area [%], $ACC_{object\ count}$ – accuracy of object count [%], AdaBoost – adaptive boosting, CCNNW – cascade-correlation neural network, CPU – central processing unit, CV – constant velocity, DAG – directed acyclic graph, DOI – depth of interest, d_{human} – total human displacement [m], d_{robot} – total robot displacement [m], $ERR_{localization}$ – target localization error, $ERR_{OF\ max}$ – maximum error percentage (ratio of true and detected optical flow), $ERR_{OF\ min}$ – minimum error percentage (ratio of true and detected optical flow), f_{camera} – camera frame rate, f_{Kinect} – sampling rate Kinect sensor(s), f_{LRF} – sampling rate of LRFs, F_{max} – maximum F measure, $f_{microphone}$ – sampling rate of microphone(s), FNR – false negative rate [%], FNR_{min} – minimum false negative rate [%], FPR – false positive rate [%], FPR_{min} – minimum false positive rate [%], f_{sonar} – sampling rate of sonar sensor(s), f_{system} – frequency of the entire system, GPU – graphics processing unit, HOG – histogram of oriented gradients, IB1 – instance based algorithm 1, IR – infrared, k-NN – k-nearest neighbour; LRF – laser range finder, MDP – Markov decision process, NN – nearest neighbour, OTCBVS – Object tracking and classification beyond the visible spectrum, PR – precision [%], PT – pan-tilt, PTZ – pan-tilt-zoom, RANSAC - random sample consensus, RFID - radio frequency identification, SN – sensitivity [%], SR – success rate [%], SR_{colour} – success rate using colour features [%], $SR_{combination}$ – success rate using combination of thermal and colour features [%], $SR_{thermal}$ – success rate using thermal features [%], SVM – support vector machine, t – time [s], t_{lat} – latency [ms], TNR_{max} – maximum true negative rate [%], t_p – processing time [ms], t_{p_LK} – processing time for Lucas-Kanade algorithm [ms], $t_{p\_meanshift}$ – processing time for mean-shift algorithm [ms], t_{p_PC} – processing time on personal computer [ms], t_{p_PT} – processing time for particle filter algorithm [ms], t_{p_robot} – processing time on mobile robot computer [ms], TPR – true positive rate [%], TPR_{max} – maximum true positive rate [%]

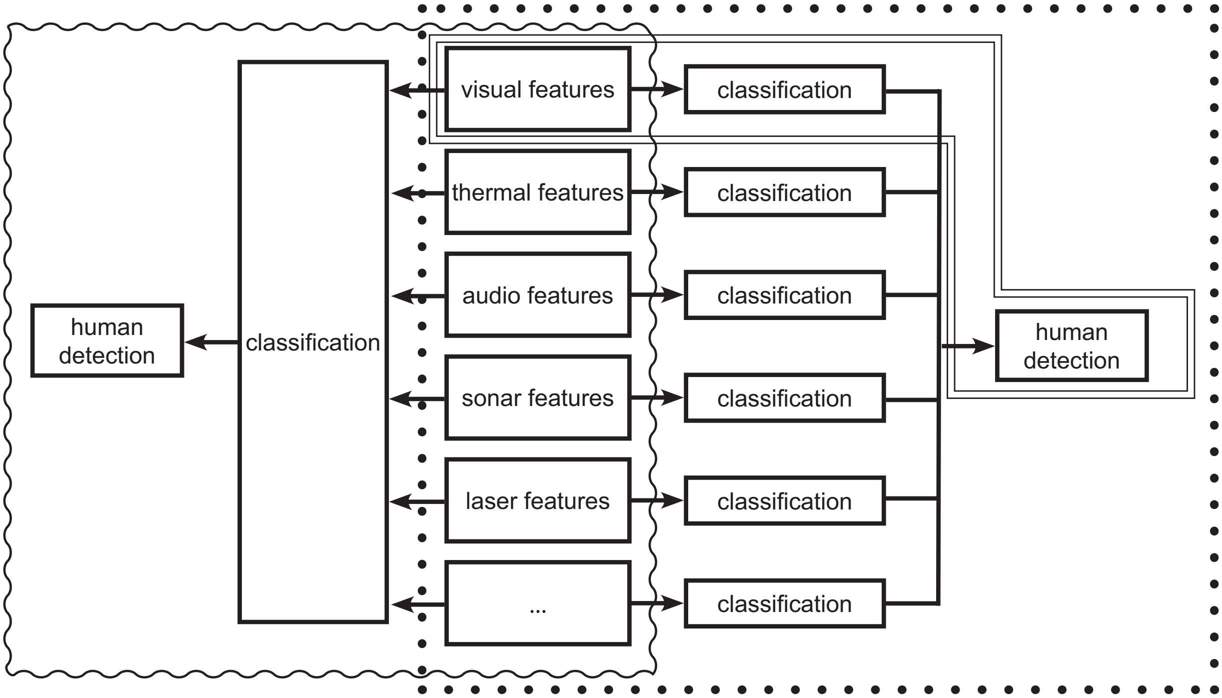

Fig. 1. *A block diagram representing basic difference between vision-only-based system (double-thin-lined shape) and multimodal systems (wavy and dotted shapes correspond to two different kinds of fusion level) shown on the example of human detection task*

2 SENSOR MODALITIES IN HUMAN-ORIENTED MOBILE ROBOTS

Machine-vision-based, human-oriented mobile robots can be either vision-only or multimodal. Table 1 offers information about the hardware and software solutions of these systems together with their performance and environmental settings.

2.1 Vision-Only-Based Systems

Vision-only-based mobile-robot systems are composed of colour vision, thermal vision or a combination of the two. In colour-vision systems, the following approaches have been implemented: conventional 2D vision, stereo vision and omnidirectional vision.

Colour vision offers robustness to geometric distortions [12], but it is susceptible to lighting variations [12] and resolution [32]. Solutions for reducing the sensitivity to illumination variations include the application of alternative colour spaces: HSV, dichromatic r-g, YUV, YCbCr and LUV. In general, any colour space that offers separate brightness and colour information can be used [49]. However, the employment of an alternative colour space may still not guarantee successful human detection. Therefore, Baltzakis et al. [15] applied prior-probability-based skin-colour detection [73], which adapts to the illumination changes. On the other hand, Wilhelm et al. [49] dealt with varying illumination by applying an automatic white-balance algorithm to the captured images in YUV colour space (a coated aluminium ring was used as a white reference). Additionally, the mean Y value was used for maintaining a brightness value of about 80 % of the maximum by controlling the camera's iris.

Conventional 2D vision lacks information about the object's location and/or its size. On the other hand, stereo systems offer additional depth information, which, however, raises the computational load due to the need for an accurate stereo correspondence. Stereo systems are less susceptible to different positions of people relative to the cameras and work even in short occlusions [100]. Depth information also offers smoother tracking by adjusting the mobile robot's speed to keep the distance to the target fixed [23]. Omnidirectional vision can be performed using various lenses, which define the characteristics of the acquired images. For example, images acquired using an optical system with a fish-eye lens have poorer resolution in the peripheral region when compared to the centre region and a perspective image [9]. Images taken with omnidirectional cameras also do not provide accurate distances between the target objects and the mobile robot, but only the angle of detection **[25]**. Furthermore, the optical flow pattern in omnidirectional images differs from the pattern in perspective images. This can be solved by transforming an omnidirectional image into a panoramic image **[33]**. An important advantage of omnidirectional vision is its ability to visualize a broader field of view for the mobile robot.

Thermal vision is based on thermal infrared (IR) video cameras, which detect emitted thermal energy in IR spectrum. Therefore, the pixels in the thermal images correspond to the temperature values. Due to the distinctive thermal profile of humans, their detection is simplified (no need for environment mapping and/or creating background models **[12]**). Additionally, temperature features are not susceptible to lighting variations, which offers visualization even in darkness and robustness to the direction of the human relative to the mobile robot. Important drawbacks include phantom detections, hard differentiation between humans, varying thermal characteristics of the airflow and the dependency of multiple-person tracking on their mutual position **[51]**. Human detection in thermal images can be performed by simple thresholding **[21]**, whether by using a single threshold value or defining the optimal value using a genetic algorithm as in **[101]**. Treptow et al. **[51]** improved thermal-vision-based human detection by proposing an elliptical contour model (one ellipse for body position and one for head position).

Vision systems can also be mounted on the ceiling and not on the mobile robots. This approach can be used in the vision-only-based control of mobile robots **[102]**, when obtaining the ground truth for tracking (as mentioned in Section 1) or in numerous Intelligent Space (iSpace) applications. iSpace is a term that refers to a space equipped with sensors and actuators, which provide an understanding of people's behaviour as well as providing them with information **[103]**. iSpace additionally controls electrically connected systems and robots in order to provide a particular service for people **[103]**. It also enables mobile robots to perform human-oriented operations, without having their own sensors and intelligence. Research regarding mobile robots in iSpace is not discussed in this manuscript.

2.2 Multimodal Systems

A single-sensor system cannot usually offer robust human tracking. It has been suggested that the most complete system for human recognition should be multimodal **[22]**, since the integration of multiple sensory channels can improve a mobile robot's performance **[19]**. This is mostly achieved by overcoming the limitations of each individual sensor. For example, in leg detection using laser range finders (LRF) false positives due to leg-like-shaped objects (e.g., table or chair legs) often occur. On the other hand, false negatives appear if a human stands sideways relative to the robot's position, is wearing clothes that hide their legs **[25]** or his/her legs are occluded. Sonar sensors are usually noisy, inaccurate and unreliable (highly dependent on the distance between the mobile robot and the target human) **[25]**. However, in sudden illumination changes sonar sensors might be able to detect a human, in contrast to the colour-vision-based approaches. They can also aid colour vision in differentiating between human faces and potential skin-coloured objects positioned behind the human faces (data from sonar sensors is used to modify the weights of the skin-colour detector) **[49]**. Auditory modality is very susceptible to noise **[19]**, which can disturb the detection and localization of sound sources of interest, but in combination with visual information human identification can be improved (if the person is not in the mobile robot's field of view **[19]**). The presence of an additional camera in an omnidirectional-based system offers verification of whether the detected object in the image obtained with the omnidirectional camera is really a human **[49]**. Fig. 1 shows basic difference between vision-only-based and general multimodal systems.

Since multimodality can improve a mobile robot's performance, the majority of the reviewed literature proposed multimodal systems (see Table 1). They include different combinations of visual systems, LRF, sonar sensors and/or microphones. Some of the research even used Kinect (Microsoft Corporation, USA), since it consists of multiple sensing devices. These include RGB cameras, 3D depth sensors (IR laser and monochrome CMOS sensor) and multi-array microphones, all mounted on a motorized tilt. Kinect has some limitations when it comes to its implementation on mobile robots. For a valid depth the mapping distance between the device and the object has to be more than 0.8 m, whereas from the resolution and noise points of view this distance should be even larger **[104]**. Besides that the sunlight influences the measurements with an embedded IR camera **[105]** and Kinect's software is adopted to images captured with a static camera. Multimodal systems are also associated with some other problems. The common ones include the computational load and the increased costs of a mobile robot. An example of a particular technical challenge includes the occurrence of misalignments due to a vertical projection from the laser to the image plane. Therefore, Fotiadis et al. [34] developed an adaptive ROI technique that compensates for these misalignments and offers a greater detection range.

The sensory data can be integrated using sequential integration (one data type is used for human detection and a reduction of the search space for other data, which is used for the verification). The outcome of this approach greatly depends on the human-detection phase. If it fails, the entire approach fails. A solution to this problem is the concurrent/parallel processing of sensory data and the integration (the entire space is tracked and the data is fused) [34]. An example of parallel processing is the generation of a Gaussian probability-based hypothesis for each data type and a combination of all the distributions by covariance intersection [25]. Jin et al. [106] proposed a fusion technique that also takes the temporal information of the measured data into account (previously acquired sensor data is used for a better measurement accuracy).

An example of a multimodal system was proposed by Fritsch et al. [44], who used auditory, vision and LRF channels. In the situations in which the target human is not facing the robot (which prevents face detection), is not speaking and the LRF fails to detect the legs the authors used colour-based torso detection (by applying a mixture of Gaussians). This approach, however, requires that each human wears different, uniformly coloured clothes. Another interesting multimodal approach was proposed by Wilhelm et al. [49], who used a two-component system for human detection. The first one helps positioning the potential human target by means of skin-colour detection and sonar data, while the second uses face detection on a high-resolution image. This component is used for verification and also offers the potential for extracting useful information about the state of a human in order for a robot to adapt to it.

3 PROPOSED APPLICATIONS OF HUMAN-ORIENTED MOBILE ROBOTS

Some of the proposed applications for the reviewed robot systems include: tracking a pre-registered person [13], an autonomous search for a single elderly person in an unstructured indoor environment [8], support for emergency personnel [16], additional support for autonomous guidance of humans in museums [15], visual guidance of mobile robots [53] and [107], providing information for staff and visitors of a specific public building [24], survey tasks [25], interactive shopping assistance [14], surveillance of large outdoor infrastructures [34], human-robot cooperation in transportation and investigations of hazardous environments [23]. Please note that all the above-mentioned proposed application have not yet been realised.

Another useful characteristic of mobile robots is human following, which is important in applications in which a proper interaction of a mobile robot with a walking human is essential (e.g., in rehabilitation [108]). Human following can be passive or anticipative. In the former, the mobile robot's motion is defined only by the position of the target human. This is useful in situations in which a person wants to control the movement of the mobile robot. On the other hand, an anticipative approach is based on predicting a person's trajectory by observing his or her walking mode. This is useful in front human following (useful in leading people through healthcare facilities). However, it has been reported that only using an anticipative approach in front following is not successful, because people change their behaviour unintentionally in the presence of a mobile robot and try to lead it [93]. A short overview of recent human-following robot applications was published in [93].

4 FUTURE CHALLENGES IN THE FIELD OF HUMAN-ORIENTED MOBILE ROBOTS

In this section we provide our view of the challenges that need to be considered when implementing mobile robots in real-world environments.

4.1 HRI and Perception of Mobile Robots by the Elderly People and Chronically Ill People

Human-oriented mobile robots with healthcare tasks should be modelled as social robots. This means that they should be able to interact with humans in various situations [109]. For a social interaction, people need to treat the robots as social beings [109]. In order to achieve as successful HRI as possible it is important to understand the perception of mobile robots by the elderly and chronically ill people.

It is hard to generalize this perception, since the age is not the only factor influencing it. In order to accept any robot, its user needs to be motivated for using the robot, which 1) has to be easy to use and 2) has to allow its user to feel comfortable (physical-, cognitive- and emotional-wise) [110]. There are numerous factors influencing the aforementioned criteria, namely individual and robot factors. Besides the age, the former include needs, gender, experience with technology, cognitive ability, education, culture, anxiety and attitudes towards robots [110]. Robot factors include appearance (humanness, size, facial expression, gender), personality and adaptability [110].

In general, with increasing age the willingness of the people to use robots decreases. However, there are reports that elderly are more likely to accept robots in order to gain back independence in handling everyday tasks upon losing it [111]. Furthermore, lack of familiarity with technology, which is often present in the elderly people, can result in uncertainty toward the robots [112]. Additionally, due to various attitudes toward aging in different cultures the cross-cultural differences exist [113]. When it comes to the robot factors, the elderly people do not want to be accompanied by the robots, which would make them look weak or dependent [114]. Additionally, they prefer smaller sized robots [115]. One of the most important characteristics is also robots' ability to adapt to the particular elderly user, since the elderly differ between each other in e.g. eyesight, movement abilities and hearing capability [110]. When it comes to chronically ill patients, the same factors need to be considered. Another important characteristic, which influences HRI in chronically ill and/or elderly people is the fact that interaction between this people is not short-termed or even single-termed, so the long-term interaction studies are highly important [116]. Unfortunately robots' appearance and behaviour cannot be adopted entirely to human expectations, so it has been suggested that human expectations can be modified in order to achieve better perception of robots [110]. More advanced view on this topic is out of scope of this article. The interested reader can refer to the following review articles: [110], [116] and [117].

4.2 Human Identification Challenges

In general, human identification can be performed using hard biometrics (iris, fingerprint and face). These trails are unique to the individuals, but the identification accuracy strongly depends on the data quality [118]. Distance from the sensor to the target, noise and user's willingness to cooperate are some of the factors that influence this quality [118]. Multimodal hard biometrics systems can offer improved performance, but can be time consuming and require even more human cooperation. As an alternative approach, one can use soft biometrics. These are composed of global (age, gender, skin colour, etc.) and local traits (eyes, eyebrows, nose, mouth, etc.) [118]. They are not unique to the individuals but can as a whole enhance the identification performance of hard biometrics and can be extracted even from lower quality data or from semantic descriptions [119]. Another popular way to identify humans (mainly in surveillance applications) is gait analysis [120], but this approach lacks applicability in healthcare, mobile-robot applications (bed bound patients, gait disorders, etc.). Lastly, human identification should be as pleasant as possible. The user should not be agitated in any way, since that could influence user's (patho)physiological state.

4.3 Possible Extensions of Multimodal Systems

Besides vision and auditory sense, there are three additional senses: touch, olfaction (airborne chemical sensing) and taste. Tactile sensors in mobile robotics are useful in applications in which physical contact with humans is required. Examples include lifting up a dummy human [121] and assisting elderly or disabled people by moving heavy objects instead of them [122]. In the latter case, its user is guiding the robot by the means of tactile communication. In these applications stability of the mobile robots [123] needs to be carefully addressed. In contrast to visual, auditory and tactile signals, which are based on single physical quantities, taste and olfaction only have a meaning when humans interpret them, since taste and odour are not properties of chemical substances [124]. This makes the implementation of olfaction and taste in any real mobile robotic applications very challenging.

Olfaction has been however already implemented in mobile robots for the purpose of gas distribution mapping, trail guidance and gas source localization [125]. On contrary, sense of taste has been implemented in the form of electronic tongues, which have their potential in use in food and pharmaceutical industries for objective and reproducible assessment of taste of foods and drugs [124].

Since healthcare mobile robots are mainly used in indoor environments, the airborne chemical sensing would be very useful in carbon monoxide detection and in prevention of sick building syndrome [126]. Furthermore, some medical conditions have characteristic odours [127] and therefore e.g., the analysis of exhaled breath could be used as a supportive diagnostic tool [128]). On the other hand different odour sensations can also cause symptoms in humans (e.g., headache, nausea, cough, stress) [129]. Identification of these odours could therefore be helpful in preventing mistakes by attributing symptoms to the wrong causes.

4.4 Other Challenges

In order to implement mobile robots in many uncontrolled environments (useful in outdoor healthcare tasks) it is also necessary to ensure the continuous mobility of these mobile robots. In [130], an approach capable of detecting failure at any wheel and optimizing traction is proposed. Additionally, this solution does not increase the hardware complexity of the mobile robot, nor the control system. The next desired characteristic of mobile robots with human-oriented tasks is real-time performance with as little energy consumption as possible. For example, the ideal system would be smooth, rapid, accurate and energy efficient. This can be achieved by mimicking animal-like coordination of the head, neck and eyes. For example, in [131], an approach using chameleon-inspired binocular vision for a swift search of a mobile robot's surroundings and a two-step aim at the target (rough and accurate) is proposed.

When it comes to real-time performance, it is suggested to first define this term. In human-oriented mobile robots the real-time performance can be defined on the basis of a person's reaction time (RT) [26]. The RT for the detection of a visual stimulus is (180 to 200) ms [132] (which is longer than for tactile and auditory RT). This means that frame rates higher than 5 fps offer real-time performance. Similar criterion was proposed in [26]. The real-time performance can be achieved using distributed computing [23] or by using computationally more demanding solutions only when needed [26].

Next, mobile robots implemented in public spaces are likely to attract people, which can result in the narrowing of passageways due to a large number of people surrounding the robot. The former can make it difficult for humans to avoid the crowd, while the latter can aggravate the performance of the mobile robot. Both situations are highly undesirable, e.g., in emergency situations. One of the proposed solutions (based on pedestrian-behaviour simulation) is to anticipate the crowding and try to avoid congestion, while at the same time respecting the surrounding humans' walking comfort and the performance of tasks, for which the mobile robot was built [133]. In cases of people gathering around the robot, an obstacle-avoiding behaviour based on a human-behaviour model can be applied [134]. For an even more successful implementation of mobile robots into public places, a long-term study in terms of their usage [135] would most likely be highly beneficial.

Other challenges include the secure transmission and collection of the measured personal data [136], which needs to be collected ethically.

4.5 A Possible Role of Vision-Based Mobile Robots in Healthcare Measurements

From the perspective of measuring clinically relevant parameters using vision systems we see the following implementations. Mobile robots with thermal vision could be used in fever screening [137], but, in general, also in thermoregulation studies, the detection of breast cancer, diagnosing diabetic neuropathy and vascular disorders, dermatology, etc. [10]. Many of these fields could significantly improve the patient's well being by regular home monitoring of a disease, which could reduce its burden (e.g., by monitoring diabetic patients with thermo vision it could be possible to prevent diabetic foot ulcers [138]). Colour-vision-based mobile robots could provide some physiological data by means of remote photoplethysmography (remote PPG) measurements, whether in reflection [11] or transmittance mode [139]. It can also be used in telemedicine in the form of simple online consultations or as a tool for diagnosing/monitoring diseases (teledermatology) [140]. In the near future, we aim to develop a human-oriented, colour-vision-based mobile robot performing certain healthcare tasks.

4.6 Techonological Trends

Current trends in robotics are focused on soft robotics. This term primarily covers implementation of soft materials, actuators and sensors in different machine application. Soft robots are expected to offer softness and safety (by the means of more natural physical HRI), which are highly desirable characteristics for the use in healthcare applications (lifting of the patients, minimally invasive surgeries, various wearable and implantable devices) [141]. From the perspective of elderly people these robots could be used as an adaptive exercisers for cognition and daily activities [141].

5 CONLCUSIONS

The reviewed literature reveals that there is no universal solution for a human-oriented mobile robot. Different hardware and software solutions have their pros and cons in different environmental settings and situations, which makes us believe that mobile robots with multiple sensor modalities will be the most studied in the near future. An interesting solution for indoor environments, such as households or clinics, is iSpace, which could offer the implementation of mobile robots with different tasks in the same environment. From the perspective of human recognition, the human-identification step seems to be the most challenging. We believe that a lot of effort will be put into it, since correct identification is crucial in healthcare, where misidentification could result in the wrong treatment, having potentially fatal consequences. Because vision systems are already being widely used in medicine, the use of thermal vision and colour vision in mobile robots for diagnostic/screening purposes is promising. In the future, to implement mobile robots in as many healthcare applications as possible, the focus will need to be put on HRI, human identification, robustness of the mobile robots' task performance and quality, together with security of the measured data.

6 ACKNOWLEDGEMENT

The presented research of the Young Researcher Miha Finžgar was supported by the Slovenian Research Agency (ARRS).

7 REFERENCES

[1] Wada, K., Shibata, T. (2007). Living with seal robots - its sociopsychological and physiological influences on the elderly at a care house. *IEEE Transactions on Robotics*, vol. 23, no. 5, p. 972-980, **DOI:10.1109/Tro.2007.906261**.

[2] Dahl, T., Boulos, M. (2014). Robots in health and social care: A complementary technology to home care and telehealthcare? *Robotics*, vol. 3, no. 1, p. 1-21, **DOI:10.3390/robotics3010001**.

[3] Evans, J.M. (1994). Helpmate: An autonomous mobile robot courier for hospitals. *Proceedings of the IEEE/RSJ/GI International Conference on Intelligent Robots and Systems*, p. 1695-1700, **DOI:10.1109/iros.1994.407629**.

[4] Sucher, J.F., Todd, S.R., Jones, S.L., Throckmorton, T., Turner, K.L., Moore, F.A. (2011). Robotic telepresence: A helpful adjunct that is viewed favorably by critically ill surgical patients. *The American Journal of Surgery*, vol. 202, no. 6, p. 843-847, **DOI:10.1016/j.amjsurg.2011.08.001**.

[5] Pripfl, J., Körtner, T., Batko-Klein, D., Hebesberger, D., Weninger, M., Gisinger, C., Frennert, S., Eftring, H., Antona, M., Adami, I., Weiss, A., Bajones, M., Vincze, M. (2016). Results of a real world trial with a mobile social service robot for older adults. *11th ACM/IEEE International Conference on Human-Robot Interaction*, p. 497-498, **DOI:10.1109/hri.2016.7451824**.

[6] Galán-Mena, J., Ávila, G., Pauta-Pintado, J., Lima-Juma, D., Robles-Bykbaev, V., Quisi-Peralta, D. (2016). An intelligent system based on ontologies and ICT tools to support the diagnosis and intervention of children with autism. IEEE Biennial Congress of Argentina, p. 1-5, **DOI:10.1109/ARGENCON.2016.7585361**.

[7] Ma, Y., Xiao, D., Li, R., Ruan, H., Shan, Z., Junlong, Z., Zhang, Y. (2015). Android-based intelligent mobile robot for indoor healthcare. *17th International Conference on E-health Networking, Application & Services (HealthCom)*, p. 472-474, **DOI:10.1109/HealthCom.2015.7454548**.

[8] Mehdi, S.A., Berns, K. (2014). Behavior-based search of human by an autonomous indoor mobile robot in simulation. *Universal Access in the Information Society*, vol. 13, no. 1, p. 45-58, **DOI:10.1007/s10209-013-0301-8**.

[9] Yagi, Y. (1999). Omnidirectional sensing and its applications. *IEICE Transactions on Information and Systems*, vol. 82, no. 3, p. 568-579.

[10] Lahiri, B.B., Bagavathiappan, S., Jayakumar, T., Philip, J. (2012). Medical applications of infrared thermography: A review. *Infrared Physics & Technology*, vol. 55, no. 4, p. 221-235, **DOI:10.1016/j.infrared.2012.03.007**.

[11] Aarts, L.A., Jeanne, V., Cleary, J.P., Lieber, C., Nelson, J.S., Bambang Oetomo, S., Verkruysse, W. (2013). Non-contact heart rate monitoring utilizing camera photoplethysmography in the neonatal intensive care unit - a pilot study. *Early Human Development*, vol. 89, no. 12, p. 943-948, **DOI:10.1016/j.earlhumdev.2013.09.016**.

[12] Cielniak, G., Duckett, T. (2004). People recognition by mobile robots. *Journal of Intelligent & Fuzzy Systems*, vol. 15, no. 1, p. 21-27.

[13] Kang, S., Roh, A., Nam, B., Hong, H. (2011). People detection method using graphics processing units for a mobile robot with an omnidirectional camera. *Optical Engineering*, vol. 50, no. 12, p. 1-8, **DOI:10.1117/1.3660573**.

[14] Böhme, H.-J., Wilhelm, T., Key, J., Schauer, C., Schröter, C., Groß, H.-M., Hempel, T. (2003). An approach to multi-modal human–machine interaction for intelligent service robots. *Robotics and Autonomous Systems*, vol. 44, no. 1, p. 83-96, **DOI:10.1016/S0921-8890(03)00012-5**.

[15] Baltzakis, H., Pateraki, M., Trahanias, P. (2012). Visual tracking of hands, faces and facial features of multiple persons. *Machine Vision and Applications*, vol. 23, no. 6, p. 1141-1157, **DOI:10.1007/s00138-012-0409-5**.

[16] Susperregi, L., Martinez-Otzeta, J.M., Ansuategui, A., Ibarguren, A., Sierra, B. (2013). RGB-D, laser and thermal sensor fusion for people following in a mobile robot. *International Journal of Advanced Robotic Systems*, vol. 10, p. 1-9, **DOI:10.5772/56123**.

[17] Ying-li, T. (2004). Evaluation of face resolution for expression analysis. *Conference on Computer Vision and Pattern Recognition Workshop*, p. 82-82, **DOI:10.1109/cvpr.2004.334**.

[18] Zafeiriou, S., Zhang, C., Zhang, Z. (2015). A survey on face detection in the wild: Past, present and future. *Computer Vision and Image Understanding*, vol. 138, p. 1-24, **DOI:10.1016/j.cviu.2015.03.015**.

[19] Bayram, B., Ince, G. (2015). Audio-visual multi-person tracking for active robot perception. *IEEE/SICE International Symposium on System Integration*, p. 575-580, **DOI:10.1109/sii.2015.7405043**.

[20] Ali, B., Ayaz, Y., Jamil, M., Gilani, S.O., Muhammad, N. (2015). Improved method for stereo vision-based human detection for a mobile robot following a target person. *South African Journal of Industrial Engineering*, vol. 26, no. 1, p. 102-119, **DOI:10.7166/26-1-891**.

[21] Fernandez-Caballero, A., Castillo, J.C., Martinez-Cantos, J., Martinez-Tomas, R. (2010). Optical flow or image subtraction in human detection from infrared camera on mobile robot. *Robotics and Autonomous Systems*, vol. 58, no. 12, p. 1273-1281, **DOI:10.1016/j.robot.2010.06.002**.

[22] Cielniak, G., Duckett, T., Lilienthal, A.J. (2010). Data association and occlusion handling for vision-based people tracking by mobile robots. *Robotics and Autonomous Systems*, vol. 58, no. 5, p. 435-443, **DOI:10.1016/j.robot.2010.02.004**.

[23] Petrović, E., Leu, A., Ristić-Durrant, D., Nikolić, V. (2013). Stereo vision-based human tracking for robotic follower. *International Journal of Advanced Robotic Systems*, vol. 10, no. 5, **DOI:10.5772/56124**.

[24] Bellotto, N., Hu, H. (2008). Multimodal people tracking and identification for service robots. *International Journal of Information Acquisition*, vol. 5, no. 3, p. 209-221, **DOI:10.1142/S0219878908001612**.

[25] Martin, C., Schaffernicht, E., Scheidig, A., Gross, H.M. (2006). Multi-modal sensor fusion using a probabilistic aggregation scheme for people detection and tracking. *Robotics and Autonomous Systems*, vol. 54, no. 9, p. 721-728, **DOI:10.1016/j.robot.2006.04.012**.

[26] Zhang, H., Reardon, C., Parker, L.E. (2013). Real-time multiple human perception with color-depth cameras on a mobile robot. *IEEE Transactions on Cybernetics*, vol. 43, no. 5, p. 1429-1441, **DOI:10.1109/TCYB.2013.2275291**.

[27] Xu, L.-Q., C. Hogg, D. (1997). Neural networks in human motion tracking – an experimental study. *Image and Vision Computing*, vol. 15, no. 8, p. 607-615, **DOI:10.1016/S0262-8856(97)00007-3**.

[28] Tsai, C.-Y., Song, K.-T. (2009). Dynamic visual tracking control of a mobile robot with image noise and occlusion robustness. *Image and Vision Computing*, vol. 27, no. 8, p. 1007-1022, **DOI:10.1016/j.imavis.2008.08.011**.

[29] Okuma, K., Taleghani, A., de Freitas, N., Little, J.J., Lowe, D.G. (2004). A boosted particle filter: Multitarget detection and tracking. Pajdla, T., Matas, J. (eds.), *Computer Vision - ECCV,* Springer-Verlag Berlin Heidelberg, Berlin, Heidelberg, p. 28-39, **DOI:10.1007/978-3-540-24670-1_3**.

[30] Stone, L.D., Streit, R.L., Corwin, T.L., Bell, K.L. (2013). *Bayesian multiple target tracking*. Artech House, Norwood, MA.

[31] Ahmad, S.M.S., Ali, B.M., Adnan, W.A.W. (2012). Technical issues and challenges of biometric applications as access control tools of information security. *International Journal of Innovative Computing Information and Control*, vol. 8, no. 11, p. 7983-7999.

[32] Alvarez-Santos, V., Pardo, X.M., Iglesias, R., Canedo-Rodriguez, A., Regueiro, C.V. (2012). Feature analysis for human recognition and discrimination: Application to a person-following behaviour in a mobile robot. *Robotics and Autonomous Systems*, vol. 60, no. 8, p. 1021-1036, **DOI:10.1016/j.robot.2012.05.014**.

[33] Kim, J., Suga, Y. (2007). An omnidirectional vision-based moving obstacle detection in mobile robot. *International Journal of Control Automation and Systems*, vol. 5, no. 6, p. 663-673.

[34] Fotiadis, E.P., Garzon, M., Barrientos, A. (2013). Human detection from a mobile robot using fusion of laser and vision information. *Sensors* (Basel), vol. 13, no. 9, p. 11603-11635, **DOI:10.3390/s130911603**.

[35] Intille, S.S., Davis, J.W., Bobick, A.F. (1997). Real-time closed-world tracking. *Proceedings of IEEE Computer Society Conference on Computer Vision and Pattern Recognition*, p. 697-703, **DOI:10.1109/CVPR.1997.609402**.

[36] Mittal, A., Davis, L.S. (2003). M2tracker: A multi-view approach to segmenting and tracking people in a cluttered scene. *International Journal of Computer Vision*, vol. 51, no. 3, p. 189-203, **DOI:10.1023/A:1021849801764**.

[37] Wren, C.R., Azarbayejani, A., Darrell, T., Pentland, A.P. (1997). Pfinder: Real-time tracking of the human body. *IEEE Transactions on Pattern Analysis and Machine Intelligence*, vol. 19, no. 7, p. 780-785, **DOI:10.1109/AFGR.1996.557243**.

[38] Schauer, C., Zahn, T., Paschke, P., Gross, H.-M. (2000). Binaural sound localization in an artificial neural network. *Proceedings of the IEEE International Conference on Acoustics, Speech, and Signal Processing*, p. 865-868, **DOI:10.1109/icassp.2000.859097**.

[39] Schauer, C., Paschke, P. (1999). A spike-based model of binaural sound localization. *International Journal of Neural Systems*, vol. 9, no. 05, p. 447-452, **DOI:10.1142/S0129065799000460**.

[40] Yang, J., Lu, W., Waibel, A. (1998). Skin-color modeling and adaptation. *Asian Conference on Computer Vision*, p. 687-694.

[41] Fahlman, S.E., Lebiere, C. (1990). The cascade-correlation learning architecture. Touretzky, D.S. (ed.), *Advances in neural information processing systems 2*. Morgan Kaufmann Publishers, San Francisco, p. 524-532.

[42] AT&T Laboratories Cambridge. The database of faces, from *http://www.cl.cam.ac.uk/research/dtg/attarchive/facedatabase.html*, accessed on 2016-12-16.

[43] Isard, M., Blake, A. (1998). Condensation–conditional density propagation for visual tracking. *International Journal of Computer Vision*, vol. 29, no. 1, p. 5-28, **DOI:10.1023/A:1008078328650**.

[44] Fritsch, J., Kleinehagenbrock, M., Lang, S., Fink, G.A., Sagerer, G. (2004). Audiovisual person tracking with a mobile robot. *Proceedings of International Conference on Intelligent Autonomous Systems*, p. 898-906.

[45] Viola, P., Jones, M. (2001). Robust real-time object detection. *International Journal of Computer Vision*, vol. 4, p. 34-47.

[46] Giuliani, D., Omologo, M., Svaizer, P. (1994). Talker localization and speech recognition using a microphone array and a cross-powerspectrum phase analysis. *International Conference on Spoken Language Processing*.

[47] Fritsch, J., Kleinehagenbrock, M., Lang, S., Plötz, T., Fink, G.A., Sagerer, G. (2003). Multi-modal anchoring for human–robot interaction. *Robotics and Autonomous Systems*, vol. 43, no. 2, p. 133-147, **DOI:10.1016/S0921-8890(02)00355-X**.

[48] Lang, S., Kleinehagenbrock, M., Hohenner, S., Fritsch, J., Fink, G.A., Sagerer, G. (2003). Providing the basis for human-robot-interaction: A multi-modal attention system for a mobile robot. *Proceedings of the 5th International Conference on Multimodal Interfaces*, p. 28-35, **DOI:10.1145/958432.958441**.

[49] Wilhelm, T., Bohme, H., Gross, H.M. (2004). A multi-modal system for tracking and analyzing faces on a mobile robot. *Robotics and Autonomous Systems*, vol. 48, no. 1, p. 31-40, **DOI:10.1016/j.robot.2004.05.004**.

[50] Feyrer, S., Zell, A. (1999). Detection, tracking, and pursuit of humans with an autonomous mobile robot. *Proceedings of the IEEE/RSJ International Conference on Intelligent Robots and Systems*, p. 864-869, **DOI:10.1109/iros.1999.812788**.

[51] Treptow, A., Cielniak, G., Duckett, T. (2006). Real-time people tracking for mobile robots using thermal vision. *Robotics and Autonomous Systems*, vol. 54, no. 9, p. 729-739, **DOI:10.1016/j.robot.2006.04.013**.

[52] Lucas, B.D., Kanade, T. (1981). An iterative image registration technique with an application to stereo vision. *International Joint Conference on Artificial Intelligence*, p. 674-679.

[53] Chang, J.S., Kim, E.Y., Kim, H.J. (2008). Mobile robot control using hand-shape recognition. *Transactions of the Institute of Measurement and Control*, vol. 30, no. 2, p. 143-152, **DOI:10.1177/0142331207080144**.

[54] Hu, M.-K. (1962). Visual pattern recognition by moment invariants. *IRE Transactions on Information Theory*, vol. 8, no. 2, p. 179-187, **DOI:10.1109/TIT.1962.1057692**.

[55] Vadakkepat, P., Lim, P., De Silva, L.C., Jing, L., Ling, L.L. (2008). Multimodal approach to human-face detection and tracking. *IEEE Transactions on Industrial Electronics*, vol. 55, no. 3, p. 1385-1393, **DOI:10.1109/Tie.2007.903993**.

[56] Bradski, G.R. (1998). Computer vision face tracking for use in a perceptual user interface. *Intel Technology Journal Q2*, p. 1-15.

[57] Viola, P., Jones, M.J. (2004). Robust real-time face detection. *International Journal of Computer Vision*, vol. 57, no. 2, p. 137-154, **DOI:10.1023/B:VISI.0000013087.49260.fb**.

[58] Bellotto, N., Hu, H. (2006). Vision and laser data fusion for tracking people with a mobile robot. *IEEE International Conference on Robotics and Biomimetics*, p. 7-12, **DOI:10.1109/ROBIO.2006.340251**.

[59] Julier, S.J., Uhlmann, J.K. (2004). Unscented filtering and nonlinear estimation. *Proceedings of the IEEE*, vol. 92, no. 3, p. 401-422, **DOI:10.1109/jproc.2003.823141**.

[60] Comaniciu, D., Ramesh, V., Meer, P. (2000). Real-time tracking of non-rigid objects using mean shift. *Proceedings of the IEEE Conference on Computer Vision and Pattern Recognition*, p. 142-149, **DOI:10.1109/cvpr.2000.854761**.

[61] Oklahoma State University. OTCBVS benchmark dataset collection, from *http://vcipl-okstate.org/pbvs/bench/*, accessed on 2016-12-16.

[62] Stricker, M.A., Orengo, M. (1995). Similarity of color images. *IS&T/SPIE's Symposium on Electronic Imaging: Science & Technology*, p. 381-392.

[63] Freund, Y., Schapire, R.E. (1995). A desicion-theoretic generalization of on-line learning and an application to boosting. *European Conference on Computational Learning Theory*, p. 23-37, **DOI:10.1007/3-540-59119-2_166**.

[64] Horn, B.K., Schunck, B.G. (1981). Determining optical flow. Artificial Intelligence, vol. 17, no. 1-3, p. 185-203, **DOI:10.1016/0004-3702(81)90024-2**.

[65] Dalal, N., Triggs, B. (2005). Histograms of oriented gradients for human detection. *IEEE Computer Society Conference on Computer Vision and Pattern Recognition*, p. 886-893, **DOI:10.1109/cvpr.2005.177**.

[66] Ojala, T., Pietikäinen, M., Harwood, D. (1996). A comparative study of texture measures with classification based on featured distributions. *Pattern Recognition*, vol. 29, no. 1, p. 51-59, **DOI:10.1016/0031-3203(95)00067-4**.

[67] Zabih, R., Woodfill, J. (1994). Non-parametric local transforms for computing visual correspondence. *European Conference on Computer Vision*, p. 151-158, **DOI:10.1007/bfb0028345**.

[68] Heikkilä, M., Pietikäinen, M., Schmid, C. (2006). Description of interest regions with center-symmetric local binary patterns. Kalra, P.K., Peleg, S. (eds.), *Computer Vision, Graphics and Image Processing. Lecture Notes in Computer Science,* Springer, p. 58-69, **DOI:10.1007/11949619_6**.

[69] Mu, Y., Yan, S., Liu, Y., Huang, T., Zhou, B. (2008). Discriminative local binary patterns for human detection in personal album. *IEEE Conference on Computer Vision and Pattern Recognition*, p. 1-8.

[70] Canny, J. (1986). A computational approach to edge detection. *IEEE Transactions on Pattern Analysis and Machine Intelligence*, no. 6, p. 679-698, **DOI:10.1109/TPAMI.1986.4767851**.

[71] Won, C.S., Park, D.K., Park, S.-J. (2002). Efficient use of MPEG-7 edge histogram descriptor. *Etri Journal*, vol. 24, no. 1, p. 23-30, **DOI:10.4218/etrij.02.0102.0103**.

[72] Baltzakis, H., Argyros, A., Lourakis, M., Trahanias, P. (2008). Tracking of human hands and faces through probabilistic fusion of multiple visual cues. *International Conference on Computer Vision Systems*, p. 33-42, **DOI:10.1007/978-3-540-79547-6_4**.

[73] Argyros, A.A., Lourakis, M.I. (2004). Real-time tracking of multiple skin-colored objects with a possibly moving camera. *European Conference on Computer Vision*, p. 368-379, **DOI:10.1007/978-3-540-24672-5_29**.

[74] Baltzakis, H., Argyros, A.A. (2009). Propagation of pixel hypotheses for multiple objects tracking. *International Symposium on Visual Computing*, p. 140-149, **DOI:10.1007/978-3-642-10520-3_13**.

[75] Cortes, C., Vapnik, V. (1995). Support-vector networks. *Machine Learning*, vol. 20, no. 3, p. 273-297, **DOI:10.1007/BF00994018**.

[76] Fischler, M.A., Bolles, R.C. (1981). Random sample consensus: A paradigm for model fitting with applications to image analysis and automated cartography. *Communications of the ACM*, vol. 24, no. 6, p. 381-395, **DOI:10.1145/358669.358692**.

[77] Viola, P., Jones, M.J., Snow, D. (2005). Detecting pedestrians using patterns of motion and appearance. *International*

Journal of Computer Vision, vol. 63, no. 2, p. 153-161, **DOI:10.1007/s11263-005-6644-8**.

[78] Bourdev, L., Malik, J. (2009). Poselets: Body part detectors trained using 3D human pose annotations. *IEEE 12th International Conference on Computer Vision*, p. 1365-1372, **DOI:10.1109/iccv.2009.5459303**.

[79] Einicke, G.A., White, L.B. (1999). Robust extended kalman filtering. *IEEE Transactions on Signal Processing*, vol. 47, no. 9, p. 2596-2599, **DOI:10.1109/78.782219**.

[80] Martínez-Otzeta, J.M., Ibarguren, A., Ansuategi, A., Susperregi, L. (2009). Laser based people following behaviour in an emergency environment. *International Conference on Intelligent Robotics and Applications*, p. 33-42, **DOI:10.1007/978-3-642-10817-4_4**.

[81] Arulampalam, M.S., Maskell, S., Gordon, N., Clapp, T. (2002). A tutorial on particle filters for online nonlinear/non-Gaussian Bayesian tracking. *IEEE Transactions on Signal Processing*, vol. 50, no. 2, p. 174-188, **DOI:10.1109/78.978374**.

[82] Susperregi, L., Sierra, B., Castrillon, M., Lorenzo, J., Martinez-Otzeta, J.M., Lazkano, E. (2013). On the use of a low-cost thermal sensor to improve Kinect people detection in a mobile robot. *Sensors* (Basel), vol. 13, no. 11, p. 14687-14713, **DOI:10.3390/s131114687**.

[83] Aha, D.W., Kibler, D., Albert, M.K. (1991). Instance-based learning algorithms. *Machine Learning*, vol. 6, no. 1, p. 37-66, **DOI:10.1007/BF00153759**.

[84] Cestnik, B. (1990). Estimating probabilities: A crucial task in machine learning. *Proceedings of the 9th European Conference on Artificial Intelligence*, p. 147-149.

[85] Sierra, B., Lazkano, E., Jauregi, E., Irigoien, I. (2009). Histogram distance-based Bayesian network structure learning: A supervised classification specific approach. *Decision Support Systems*, vol. 48, no. 1, p. 180-190, **DOI:10.1016/j.dss.2009.07.010**.

[86] Quinlan, J.R. (2014). C4. 5: *Programs for Machine Learning*. Elsevier.

[87] Martínez-Otzeta, J.M., Sierra, B., Lazkano, E., Astigarraga, A. (2006). Classifier hierarchy learning by means of genetic algorithms. *Pattern Recognition Letters*, vol. 27, no. 16, p. 1998-2004, **DOI:10.1016/j.patrec.2006.06.001**.

[88] Natarajan, S.K., Ristic-Durrant, D., Leu, A., Gräser, A. (2011). Robust stereo-vision based 3D modelling of real-world objects for assistive robotic applications. *IEEE/RSJ International Conference on Intelligent Robots and Systems*, p. 786-792, **DOI:10.1109/iros.2011.6094716**.

[89] Beetz, M., Arbuckle, T., Belker, T., Cremers, A.B., Schulz, D., Bennewitz, M., Burgard, W., Hahnel, D., Fox, D., Grosskreutz, H. (2001). Integrated, plan-based control of autonomous robots in human environments. *IEEE Intelligent Systems*, vol. 16, no. 5, p. 56-65, **DOI:10.1109/mis.2001.956082**.

[90] Foka, A.F., Trahanias, P.E. (2010). Probabilistic autonomous robot navigation in dynamic environments with human motion prediction. *International Journal of Social Robotics*, vol. 2, no. 1, p. 79-94, **DOI:10.1007/s12369-009-0037-z**.

[91] Viola, P., Jones, M. (2001). Rapid object detection using a boosted cascade of simple features. *Proceedings of the 2001 IEEE Computer Society Conference on Computer Vision and Pattern Recognition*, p. I-511-I-518 vol. 511, **DOI:10.1109/cvpr.2001.990517**.

[92] Ciric, I., Cojbasic, Z., Nikolic, V., Antic, D. (2013). Computationally intelligent system for thermal vision people detection and tracking in robotic applications. *11th International Conference on Telecommunication in Modern Satellite, Cable and Broadcasting Services*, p. 587-590., **DOI:10.1109/telsks.2013.6704447**.

[93] Hu, J.S., Wang, J.J., Ho, D.M. (2014). Design of sensing system and anticipative behavior for human following of mobile robots. *IEEE Transactions on Industrial Electronics*, vol. 61, no. 4, p. 1916-1927, **DOI:10.1109/Tie.2013.2262758**.

[94] Borges, G.A., Aldon, M.-J. (2004). Line extraction in 2D range images for mobile robotics. *Journal of Intelligent and Robotic Systems*, vol. 40, no. 3, p. 267-297, **DOI:10.1023/B:JINT.0000038945.55712.65**.

[95] Comaniciu, D., Ramesh, V., Meer, P. (2003). Kernel-based object tracking. *IEEE Transactions on Pattern Analysis and Machine Intelligence*, vol. 25, no. 5, p. 564-577, **DOI:10.1109/TPAMI.2003.1195991**.

[96] Li, P., Zhang, T., Pece, A.E. (2003). Visual contour tracking based on particle filters. *Image and Vision Computing*, vol. 21, no. 1, p. 111-123, **DOI:10.1016/S0262-8856(02)00133-6**.

[97] Nakamura, K., Nakadai, K., Asano, F., Ince, G. (2011). Intelligent sound source localization and its application to multimodal human tracking. *Proceedings of the IEEE/RSJ International Conference on Intelligent Robots and Systems,* p. 143-148, **DOI:10.1109/iros.2011.6094558**.

[98] Singh, S.K., Chauhan, D., Vatsa, M., Singh, R. (2003). A robust skin color based face detection algorithm. *Tamkang Journal of Science and Engineering*, vol. 6, no. 4, p. 227-234.

[99] Bradski, G.R. (1998). Real time face and object tracking as a component of a perceptual user interface. *Proceedings of the 4th IEEE Workshop on Applications of Computer Vision*, p. 214-219, **DOI:10.1109/acv.1998.732882**.

[100] Ess, A., Leibe, B., Schindler, K., Gool, L.V. (2008). A mobile vision system for robust multi-person tracking. *IEEE Conference on Computer Vision and Pattern Recognition*, p. 1-8, **DOI:10.1109/cvpr.2008.4587581**.

[101] Ciric, I.T., Cojbasic, Z.M., Nikolic, V.D., Igic, T.S., Tursnek, B.A.J. (2014). Intelligent optimal control of thermal vision-based person-following robot platform. *Thermal Science*, vol. 18, no. 3, p. 957-966, **DOI:10.2298/Tsci1403957c**.

[102] Simončič, S., Podržaj, P. (2014). Vision-based control of a line-tracing mobile robot. *Computer Applications in Engineering Education*, vol. 22, no. 3, p. 474-480, **DOI:10.1002/cae.20573**.

[103] Lee, J.-H., Hashimoto, H. (2002). Intelligent space–concept and contents. *Advanced Robotics*, vol. 16, no. 3, p. 265-280, **DOI:10.1163/156855302760121936**.

[104] Khoshelham, K., Elberink, S.O. (2012). Accuracy and resolution of Kinect depth data for indoor mapping applications. *Sensors* (Basel), vol. 12, no. 2, p. 1437-1454, **DOI:10.3390/s120201437**.

[105] Suarez, J., Murphy, R.R. (2012). Using the Kinect for search and rescue robotics. *IEEE International Symposium on*

Safety, Security, and Rescue Robotics, p. 1-2, **DOI:10.1109/ssrr.2012.6523918**.

[106] Jin, T.-S., Lee, J.M., Tso, S. (2004). A new approach using sensor data fusion for mobile robot navigation. *Robotica*, vol. 22, no. 01, p. 51-59, **DOI:10.1017/S0263574703005381**.

[107] Huang, S.J., Liu, S., Wu, C.H. (2015). Intelligent humanoid mobile robot with embedded control and stereo visual feedback. *Journal of Mechanical Science and Technology*, vol. 29, no. 9, p. 3919-3931, **DOI:10.1007/s12206-015-0838-y**.

[108] Gross, H.-M., Scheidig, A., Debes, K., Einhorn, E., Eisenbach, M., Mueller, S., Schmiedel, T., Trinh, T.Q., Weinrich, C., Wengefeld, T., Bley, A., Martin, C. (2016). ROREAS: Robot coach for walking and orientation training in clinical post-stroke rehabilitation—prototype implementation and evaluation in field trials. *Autonomous Robots*, p. 1-20, **DOI:10.1007/s10514-016-9552-6**.

[109] Breazeal, C., Scassellati, B. (1999). How to build robots that make friends and influence people. *Proceedings of the IEEE/RSJ International Conference on Intelligent Robots and Systems*, p. 858-863, **DOI:10.1109/iros.1999.812787**.

[110] Broadbent, E., Stafford, R., MacDonald, B. (2009). Acceptance of healthcare robots for the older population: Review and future directions. *International Journal of Social Robotics*, vol. 1, no. 4, p. 319-330, **DOI:10.1007/s12369-009-0030-6**.

[111] Arras, K.O., Cerqui, D. (2005). *Do we want to share our lives and bodies with robots? A 2000 people survey*. ETH-Zürich, Zürich.

[112] Dijkers, M.P., deBear, P.C., Erlandson, R.F., Kristy, K., Geer, D.M., Nichols, A. (1991). Patient and staff acceptance of robotic technology in occupational therapy: A pilot study. *Journal of Rehabilitation Research & Development*, vol. 28, no. 2, p. 33-44, **DOI:10.1682/JRRD.1991.04.0033**.

[113] Shibata, T., Wada, K., Ikeda, Y., Sabanovic, S. (2009). Cross-cultural studies on subjective evaluation of a seal robot. *Advanced Robotics*, vol. 23, no. 4, p. 443-458, **DOI:10.1163/156855309X408826**.

[114] Hirsch, T., Forlizzi, J., Hyder, E., Goetz, J., Kurtz, C., Stroback, J. (2000). The ELDer project: Social, emotional, and environmental factors in the design of eldercare technologies. *Proceedings on the Conference on Universal Usability*, p. 72-79, **DOI:10.1145/355460.355476**.

[115] Giuliani, M.V., Scopelliti, M., Fornara, F. (2005). Elderly people at home: Technological help in everyday activities. *IEEE International Workshop on Robot and Human Interactive Communication*, p. 365-370, **DOI:10.1109/roman.2005.1513806**.

[116] Leite, I., Martinho, C., Paiva, A. (2013). Social robots for long-term interaction: A survey. *International Journal of Social Robotics*, vol. 5, no. 2, p. 291-308, **DOI:10.1007/s12369-013-0178-y**.

[117] Broekens, J., Heerink, M., Rosendal, H. (2009). Assistive social robots in elderly care: A review. *Gerontechnology*, vol. 8, no. 2, p. 94-103, **DOI:10.4017/gt.2009.08.02.002.00**.

[118] Reid, D., Samangooei, S., Chen, C., Nixon, M., Ross, A. (2013). Soft biometrics for surveillance: An overview. Rao, C.R., Govindaraju, V. (eds.), *Handbook of statistics: Machine learning: Theory and applications*, Elsevier, p. 327-352, **DOI:10.1016/B978-0-444-53859-8.00013-8**.

[119] Almudhahka, N.Y., Nixon, M.S., Hare, J.S. (2016). Unconstrained human identification using comparative facial soft biometrics. *IEEE International Conference on Biometrics Theory, Applications and Systems*, p. 1-6, **DOI:10.1109/btas.2016.7791206**.

[120] Lee, T.K.M., Belkhatir, M., Sanei, S. (2014). A comprehensive review of past and present vision-based techniques for gait recognition. *Multimedia Tools and Applications*, vol. 72, no. 3, p. 2833-2869, **DOI:10.1007/s11042-013-1574-x**.

[121] Mukai, T., Onishi, M., Odashima, T., Hirano, S., Luo, Z. (2008). Development of the tactile sensor system of a human-interactive robot. *IEEE Transactions on Robotics*, vol. 24, no. 2, p. 505-512, **DOI:10.1109/TRO.2008.917006**.

[122] Wang, H., Liu, X.P. (2011). Haptic interaction for mobile assistive robots. *IEEE Transactions on Instrumentation and Measurement*, vol. 60, no. 11, p. 3501-3509, **DOI:10.1109/TIM.2011.2161141**.

[123] Moosavian, S.A.A., Alipour, K. (2007). On the dynamic tip-over stability of wheeled mobile manipulators. *International Journal of Robotics & Automation*, vol. 22, no. 4, p. 322, **DOI:10.2316/Journal.206.2007.4.206-3036**.

[124] Toko, K., Tahara, Y., Habara, M., Kobayashi, Y., Ikezaki, H. (2016). Taste sensor: Electronic tongue with global selectivity. Nakamoto, T. (ed.), *Essentials of Machine Olfaction and Taste*, p. 87-174, **DOI:10.1002/9781118768495.ch4**.

[125] Lilienthal, A.J., Loutfi, A., Duckett, T. (2006). Airborne chemical sensing with mobile robots. *Sensors*, vol. 6, no. 11, p. 1616-1678, **DOI:10.3390/s6111616**.

[126] Redlich, C.A., Sparer, J., Cullen, M.R. (1997). Sick-building syndrome. *The Lancet*, vol. 349, no. 9057, p. 1013-1016, **DOI:10.1016/S0140-6736(96)07220-0**.

[127] Liddell, K. (1976). Smell as a diagnostic marker. *Postgraduate Medical Journal*, vol. 52, no. 605, p. 136-138, **DOI:10.1136/pgmj.52.605.136**.

[128] Whittle, C.L., Fakharzadeh, S., Eades, J., Preti, G. (2007). Human breath odors and their use in diagnosis. *Annals of the New York Academy of Sciences*, vol. 1098, p. 252-266, **DOI:10.1196/annals.1384.011**.

[129] Schiffman, S.S., Williams, C.M. (2005). Science of odor as a potential health issue. *Journal of Environmental Quality*, vol. 34, no. 1, p. 129-138.

[130] Xu, H., Gao, X.Z., Xu, Y., Wang, K., Yu, H., Li, Z., Alipour, K., Ani, O.A. (2016). Continuous mobility of mobile robots with a special ability for overcoming driving failure on rough terrain. *Robotica*, p. 1-21, **DOI:10.1017/S0263574716000606**.

[131] Xu, H., Xu, Y., Fu, H., Gao, X.Z., Alipour, K. (2014). Coordinated movement of biomimetic dual PTZ visual system and wheeled mobile robot. *Industrial Robot: An International Journal*, vol. 41, no. 6, p. 557-566, **DOI:10.1108/ir-05-2014-0345**.

[132] Thompson, P., Colebatch, J., Brown, P., Rothwell, J., Day, B., Obeso, J., Marsden, C. (1992). Voluntary stimulus-sensitive jerks and jumps mimicking myoclonus or pathological startle syndromes. *Movement Disorders*, vol. 7, no. 3, p. 257-262, **DOI:10.1002/mds.870070312**.

[133] Kidokoro, H., Kanda, T., Brščić, D., Shiomi, M. (2015). Simulation-based behavior planning to prevent congestion of pedestrians around a robot. *IEEE Transactions on Robotics*, vol. 31, no. 6, p. 1419-1431, **DOI:10.1109/TRO.2015.2492862**.

[134] Szemes, P.T., Hashimoto, H., Korondi, P. (2005). Pedestrian-behavior-based mobile agent control in intelligent space. *IEEE Transactions on Instrumentation and Measurement*, vol. 54, no. 6, p. 2250-2257, **DOI:10.1109/TIM.2005.858824**.

[135] Brščić, D., Kanda, T. (2015). Changes in usage of an indoor public space: Analysis of one year of person tracking. *IEEE Transactions on Human-Machine Systems*, vol. 45, no. 2, p. 228-237, **DOI:10.1109/THMS.2014.2374172**.

[136] Wu, P., Yi, W.J., Saniie, J. (2016). Security assessment for personal health data management system. *IEEE International Conference on Electro Information Technology*, p. 0422-0427, **DOI:10.1109/eit.2016.7535277**.

[137] Ng, E.Y.K., Kawb, G.J.L., Chang, W.M. (2004). Analysis of IR thermal imager for mass blind fever screening. *Microvascular Research*, vol. 68, no. 2, p. 104-109, **DOI:10.1016/j.mvr.2004.05.003**.

[138] Sousa, P., Felizardo, V., Oliveira, D., Couto, R., Garcia, N.M. (2015). A review of thermal methods and technologies for diabetic foot assessment. *Expert Review of Medical Devices*, vol. 12, no. 4, p. 439-448, **DOI:10.1586/17434440.2015.1032251**.

[139] Amelard, R., Scharfenberger, C., Kazemzadeh, F., Pfisterer, K.J., Lin, B.S., Clausi, D.A., Wong, A. (2015). Feasibility of long-distance heart rate monitoring using transmittance photoplethysmographic imaging (PPGI). *Scientific Reports*, vol. 5, p. 1-11, **DOI:10.1038/srep14637**.

[140] Sharma, P., Kovarik, C.L., Lipoff, J.B. (2016). Teledermatology as a means to improve access to inpatient dermatology care. *Journal of Telemedicine and Telecare*, vol. 22, no. 5, p. 304-310, **DOI:10.1177/1357633X15603298**.

[141] Rossiter, J., Hauser, H. (2016). Soft robotics - the next industrial revolution? [industrial activities]. *IEEE Robotics & Automation Magazine*, vol. 23, no. 3, p. 17-20, **DOI:10.1109/MRA.2016.2588018**.

Vsebina

Strojniški vestnik - Journal of Mechanical Engineering
letnik 63, (2017), številka 5
Ljubljana, maj 2017
ISSN 0039-2480

Izhaja mesečno

Razširjeni povzetki (extended abstracts)

Strojniški vestnik - Journal of Mechanical Engineering 63(2017)5, SI 43
© 2017 Strojniški vestnik. Vse pravice pridržane.

Prejeto v recenzijo: 2016-11-13
Prejeto popravljeno: 2017-01-22
Odobreno za objavo: 2017-02-20

Analiza kritičnih odpovedi cevi pregrevalnika kotla na premog

Gagan Kumar Gupta* – Somnath Chattopadhyaya
Indijski inštitut za tehnologijo (Indijska rudarska šola), Oddelek za strojništvo, Indija

V kotlu je več delov, ki obratujejo pod tlakom: cevi uparjalnika, ekonomajzer in pregrevalnik. Nadtlaku v pregrevalniku se ni mogoče izogniti in kakršnakoli njegova odpoved z gotovostjo povzroči popolno zaustavitev kotla oz. celotnega postrojenja, zato so nujni ukrepi za preprečitev tehnične in gospodarske izgube. Pri tem ne zadostuje le identifikacija mest odpovedi, opredeliti je treba tudi osnovne vzroke odpovedi. V kotlu na premog v podjetju Bokaro Power Supply Co. (P) Ltd. (skupno podjetje družb SAIL in DVC), Bokaro (Indija), so se ponavljale odpovedi cevi pregrevalnika – v kratkem času so zabeležili kar tri. Na samem objektu ni bilo mogoče ugotoviti pravega vzroka odpovedi in zato se je pojavila potreba po razvoju celovite metodologije za preučevanje osnovnih vzrokov odpovedi omenjenih cevi.

V članku je predstavljena posplošena metoda za preučevanje odpovedi cevi pregrevalnika pri kotlu na premog, ki omogoča določitev narave oz. vzroka odpovedi in je sestavljena iz vizualnega pregleda, identifikacije mest vzorčenja, določanja kemične sestave osnovne zlitine, preiskave mikrostrukture z optičnim mikroskopom, podrobnejše določitve strukture z vrstičnim elektronskim mikroskopom (SEM), analize trdote vzorcev, pridobljenih z različnih mest, analize loma na različnih mestih odpovedi ter rentgenske difrakcijske analize (XRD) korozijskih produktov na notranji površini cevi. Cevi kotla, ki so odpovedale, so bile izdelane iz malolegiranega Cr-Mo jekla po poljski specifikaciji ‘Steel 10H2M’.

Koncentracija glavnih kemičnih elementov je bila znotraj specificiranih vrednosti. Mikrostruktura materiala cevi je bila poligonalno feritna. Na mejah med zrni so bili najdeni praktično kroglasti zlitinski karbidi, na notranji površini cevi pa je bila ugotovljena oksidacijska korozija v plasteh (z eksfoliacijo). Material cevi ni imel perlitno-bainitne mikrostrukture, ki je značilna za tovrstna visokotemperaturna Cr-Mo jekla, kar je posledica dolgotrajne izpostavitve visokim temperaturam. Dimenzije cevi v bližini mesta zloma so bile močno spremenjene, razen velikih razpok pa je bilo najdenih tudi več skoraj popolnoma ravnih linijskih razpok v vzdolžni smeri cevi. Iz degradacije strukture je mogoče sklepati, da se je na notranji steni cevi med obratovanjem zaradi kroženja vode oblikovala oksidna plast. Oksidna plast je z debeljenjem sčasoma izstopila (eksfoliacija) in povzročila tanjšanje cevi z notranje strani, lokalno oz. po določeni dolžini. Efektivna debelina sten cevi se je s tem zmanjšala, zaradi manjše toplotne prevodnosti oksidne plasti pa je prišlo do lokalnega pregrevanja. V stanjšanem prerezu so se pojavile deformacije zaradi lezenja in zmanjšala se je nosilnost komponente. Z zmanjšanjem debeline cevi so obodne napetosti zaradi tlaka pare presegle kritično mejo ter povzročile še dodaten upad debeline sten cevi in odpoved cevi z zlomom vrste ‘ribja usta’.

Metodologijo je mogoče razširiti tudi za iskanje vzrokov odpovedi na drugih jeklenih visokotlačnih ceveh v kotlu. Predstavljeno delo je solidna osnova za ugotavljanje osnovnih vzrokov odpovedi in ključna rešitev za težave s cevmi v industrijskih kotlih. Odpovedi cevi pregrevalnika se je mogoče izogniti z omejevanjem kontaminacije z dodano neobdelano vodo ter z rednim kemičnim čiščenjem oksidov na notranjih stenah cevi.

Ključne besede: kotel na premog, korozija, lezenje, fraktografska analiza, SEM, cev pregrevalnika, XRD

---

*Naslov avtorja za dopisovanje: Indijski inštitut za tehnologijo (Indijska rudarska šola), Oddelek za strojništvo, Dhanbad, Indija, gagan_k_gupta@rediffmail.com

Strojniški vestnik - Journal of Mechanical Engineering 63(2017)5, SI 44
© 2017 Strojniški vestnik. Vse pravice pridržane.

Prejeto v recenzijo: 2016-11-25
Prejeto popravljeno: 2017-03-03
Odobreno za objavo: 2017-03-27

Vpliv kvazistacionarnih vetrnih obremenitev na utrujenostne poškodbe prenosnikov vetrnih turbin

Dong Xiang* – Li Jiang – Mengxing You – Yinhua Shen
Univerza Tsinghua, Oddelek za strojništvo, Kitajska

Kvazistatičen veter se spreminja v času in prostoru ter močno vpliva na utrujenostno trajnostno dobo prenosnikov vetrnih turbin. Spoznanja o tem, kakšen in kolikšen je ta vpliv, so zato zelo koristna – še posebej v fazi konstrukcije prenosnikov.

Prispevek preučuje problem računanja utrujenostnih poškodb prenosnikov v razmerah kvazistatičnih vetrnih obremenitev. Kvazistatično vetrno polje je opisano s srednjo hitrostjo vetra in z intenziteto turbulenc in raziskan je vpliv obeh parametrov na utrujenostno trajnostno dobo prenosnika vetrne turbine. Najprej je bila za določitev dinamičnih sil ubiranja in vrtilne hitrosti vsakega zobnika uporabljena razklopljena metoda z globalno analizo vetrne turbine in dinamično analizo prenosnika. V drugem koraku so bile na osnovi dinamičnih obremenitev in parametrov SN zobnikov izračunane utrujenostne poškodbe vsakega zobnika z upogibanjem in jamičenjem. Iz rezultatov nato sledi analiza vpliva srednje hitrosti vetra in intenzitete turbulenc na utrujenostne poškodbe prenosnikov.

Utrujenostne poškodbe prenosnika vetrne turbine so analizirane v treh korakih. Prvi korak je globalna analiza, kjer je vhodni parameter kvazistacionarno vetrno polje ter se izračunajo vhodni in izhodni parametri prenosnika. Drugi korak je analiza sistema za prenos moči, momenti in hitrosti iz globalne analize pa so uporabljeni v dinamičnem modelu ADAMS za določitev dinamičnih obremenitev in hitrosti vsakega zobnika. Tretji korak je analiza utrujenostnih poškodb. Dinamične obremenitve se najprej pretvorijo v skupine napetosti po metodi porazdelitve trajanja obremenitev (LDD), nato pa se iz skupin in parametrov SN zobnika po hipotezi linearnih poškodb Palgren-Miner izračunajo utrujenostne poškodbe.

1) Krožnični zobnik v 1. in 2. stopnji ter pastorek v 3. stopnji so najbolj izpostavljeni upogibnim utrujenostnim poškodbam, sončno kolo v 1. in 2. stopnji ter pastorek v 3. stopnji pa jamičenju.
2) Utrujenostne poškodbe so praktično konstantne pri srednjih hitrostih vetra nad 14 m/s ter pri intenziteti turbulenc nad 14 %, ko je srednja hitrost vetra večja od nazivne. Z drugimi besedami – vetrne obremenitve ne povzročajo dodatnih utrujenostnih poškodb.
3) Ko se povprečna hitrost vetra poveča nad 13 m/s, so utrujenostne poškodbe zaradi stacionarnega vetra večje od poškodb zaradi turbulenc.
4) Pastorek v 3. stopnji je najbolj občutljiv na spremenljive vetrne obremenitve.
5) Občutljivost zobnikov na hitrost vetra v zvezi z utrujenostnimi poškodbami ni odvisna od intenzitete turbulenc, vršna vrednost pa je dosežena, ko je srednja hitrost vetra enaka nazivni ali pa je zelo nizka (pod 7 m/s).

V dinamičnem modelu prenosnika je vključena samo rotacijska prostostna stopnja, za podrobnejšo analizo pa bi bilo treba uvesti še translacijo v smereh x in y. V globalni analizi prav tako ni upoštevano vrtenje ohišja vetrne turbine okrog navpične osi (smer vetra se spreminja v območju od –5 do 5°). Za realnejši globalni odziv bi bilo treba modelirati vrtenje okrog navpične smeri pri večjih spremembah smeri vetra.

1) Identificirane so komponente v vseh stopnjah prenosnika, ki so najbolj izpostavljene utrujenostnim poškodbam z jamičenjem in upogibom. To spoznanje je uporabno pri odkrivanju vzrokov napak.
2) Identificiran je zobnik, ki je najbolj občutljiv na vetrne obremenitve in mu je zato treba posvetiti največ pozornosti pri projektiranju (npr. za večjo zanesljivost).
3) Identificirane so točke, v katerih je občutljivost zobnikov na utrujenostne poškodbe zaradi hitrosti vetra in intenzitete turbulenc največja. Potrebno bi bilo zasnovati tudi sistem za krmiljenje nagiba lopatic, ki bi toleriral spremembe vetrnih obremenitev.

Ključne besede: kvazistatične vetrne obremenitve, utrujenostna trajnostna raba, prenosnik vetrne turbine, porazdelitev trajanja obremenitev (LDD), FAST, ADAMS

---

*Naslov avtorja za dopisovanje: Univerza Tsinghua, Oddelek za strojništvo, Peking, Kitajska, xd@mail.tsinghua.edu.cn

Strojniški vestnik - Journal of Mechanical Engineering 63(2017)5, SI 45

Prejeto v recenzijo: 2016-12-06
Prejeto popravljeno: 2017-03-20
Odobreno za objavo: 2017-03-27

Analiza zmogljivosti hladiva R1234yf kot enakovredne zamenjave za R134a in učinek notranjega prenosnika toplote pri avtomobilski hladilni napravi

Mehmet Direk[1,*] – Alper Kelesoglu[2] – Ahmet Akin[2]
[1] Univerza v Yalovi, Tehniška fakulteta, Turčija
[2] Univerza v Yalovi, Fakulteta za znanost in tehniko, Turčija

Globalno segrevanje zaradi povečanih izpustov toplogrednih plinov je danes eden največjih problemov človeštva. Študije omejevanja uporabe klorofluoroogljikovodikov (CFC), delno halogeniranih klorofluoroogljikovodikov (HCF) in fluoriranih ogljikovodikov (HFC) še potekajo, po Direktivah in regulativi Evropske komisije in Sveta (40/2006/ES, 206/2012/EU in 517/2014) pa bo od leta 2022 prepovedana uporaba hladiv, katerih potencial globalnega segrevanja (vrednost GWP) presega 150. Uporaba hladiva R134a (GWP = 1430) po letu 2022 zato ne bo več mogoča. Hladivo R1234yf (GWP = 4) je deležno velike pozornosti kot enakovredna zamenjava za R134a, saj ima podobne termodinamične in fizikalne lastnosti.

V predstavljeni študiji je bila opravljena analiza uporabe R1234yf kot enakovredne zamenjave za R134a v nemodificirani avtomobilski hladilni napravi. V ta namen je bila zgrajena eksperimentalna avtomobilska hladilna naprava, projektirana za hladivo R134a. Raziskan je bil tudi učinek notranjega pronosnika toplote (IHX) na delovanje sistema s hladivom R1234yf. Eksperimenti so bili opravljeni pri različnih hitrostih kompresorja in temperaturah zračnih tokov. Kompresor je deloval v območju vrtilne hitrosti 1000 vrt/min do 2000 vrt/min, temperatura zračnih tokov pa je bila v območju 27 °C do 35 °C. Primerjava zmogljivosti obeh hladiv je opravljena na osnovi parametrov kot so hladilna moč, hladilno število in temperatura na izstopu iz kompresorja. Rezultati so prikazani kot funkcija vrtilne hitrosti kompresorja in temperature zračnih tokov. Hladilna moč in hladilno število sistema, napolnjenega s hladivom R1234yf, sta bila za 13,9 % do 20,4 % oz. za 7,5 % do 16,5 % manjša kot pri hladivu R134a. Ko se v enaki meri poveča temperatura zraka na vstopu v uparjalnik in kondenzator, se hladilno število in hladilna moč zmanjšata. Zmogljivostne lastnosti hladiva R1234yf so torej slabše kot pri hladivu R134a.

Za izboljšanje zmogljivosti delovanja sistema s hladivom R1234yf je bil nato v sistem vgrajen 900 mm dolgi notranji prenosnik toplote zunanjega premera 15.875 mm in notranjega premera 9.525 mm. Nato je bil ponovljen enak eksperimentalni postopek. Hladilna moč s hladivom R1234yf pri temperaturi zračnega toka 27 °C oz. 35 °C se je izboljšala za 6,3 % do 8,6 % oz. za 6,4 % do 9,9 %. Zaradi učinka pregrevanja IHX in s tem povezanega povečanega ekvivalentnega toplotnega toka kompresorja se je povečala tudi moč kompresorja. Hladilno število sistema pri temperaturi zračnega toka 27 °C oz. 35 °C se je povečalo za 2,8 % do 7,4 % oz. za 2,4 % do 4,8 %. Razlika v hladilni kapaciteti med sredstvoma R134a in R1234yf se je zmanjšala zaradi dosežene stopnje podhladitve ob uporabi notranjega izmenjevalnika toplote pri visokih hitrostih kompresorja. Notranji izmenjevalnik toplote je pri temperaturi zračnega toka na vstopu v uparjalnik in kondenzator 27 oz. 35 °C povzročil povišanje temperature na izhodu iz kompresorja za 4,2 °C oz. 5,2 °C. Sledi sklep, da je mogoče z notranjim izmenjevalnikom toplote občutno izboljšati parametre delovanja sistema.

Ključne besede: potencial globalnega segrevanja, R134a, R1234yf, avtomobilska hladilna naprava, notranji prenosnik toplote, hladilno število

---

*Naslov avtorja za dopisovanje: Univerza v Yalovi, Tehniška fakulteta, Yalova, 77200, Turčija. mehmetdirek@hotmail.com

Strojniški vestnik - Journal of Mechanical Engineering 63(2017)5, SI 46
© 2017 Strojniški vestnik. Vse pravice pridržane.

Prejeto v recenzijo: 2016-06-30
Prejeto popravljeno: 2017-02-13
Odobreno za objavo: 2017-02-27

Izračun učinkovitosti ubiranja novega stožčastega evolventnega zobnika

Li Yu[1,3] – Guangjian Wang[1,2,*] – Shuaidong Zou[1,3]
[1] Državni laboratorij za mehanske prenose, Univerza v Chongqingu, Kitajska
[2] Kolidž za avtomobilsko tehniko, Univerza v Chongqingu, Kitajska
[3] Kolidž za strojništvo, Univerza v Chongqingu, Kitajska

Nezvezen pomik ob spremembi smeri gibanja zaradi zračnosti je eden najpomembnejših dejavnikov, ki zmanjšujejo natančnost pozicioniranja in stabilnost natančnih zobniških prenosnikov. V članku je predstavljena nova vrsta stožčastih evolventnih zobnikov, ki odpravlja omenjeno nezveznost. Rezultati študije vpliva parametrov zobnika na učinkovitost ubiranja so uporabni pri snovanju zobnikov in pri izbiri omenjenih parametrov, predstavljajo pa tudi teoretični prispevek k razvoju predlaganega zobnika.

Učinkovitost ubiranja zobnikov s poševnimi zobmi se običajno določa po postopku primerjave z enakovrednimi zobniki z ravnimi zobmi. Izračuni se osredotočajo predvsem na celotno učinkovitost ubiranja, ne prikazujejo pa variabilnosti in ne upoštevajo sprememb namestitve zob v ubiranju.

Članek predstavlja izračun učinkovitosti ubiranja predlaganega zobnika na osnovi analize procesa ubiranja in možnih stanj ubiranja ob upoštevanju drsnega trenja. Liniji stika in ubiranja sta razdeljeni na mikrosegmente, upoštevano pa je tudi spreminjajoče se število zob v ubiranju. Izračunani so spremenljiva dolžina linije stika, obremenitev in trenutna učinkovitost ubiranja ob upoštevanju modula, nagibnega kota poševnih zob in modifikacijskega količnika. Podana je tudi spremenljiva učinkovitost ubiranja pri različnih vrednostih vhodne hitrosti in izhodnega navora. Določena je spremenljiva učinkovitost v celotnem krogu ubiranja, rezultati pa se dobro ujemajo s podatki v literaturi.

Ugotovljeno je bilo, da se učinkovitost ubiranja povečuje z modulom in zmanjšuje z obremenitvijo. Večji modul torej izboljša učinkovitost ubiranja pri velikih obremenitvah. Pri večjem nagibnem kotu poševnih zob se povečajo izgube na začetku in koncu ubiranja. Z manjšim nagibnim kotom je tako mogoče zmanjšati torne izgube ter izpolniti zahtevo po zmanjšanju nezveznega pomika ob spremembi smeri gibanja zaradi zračnosti. Zaradi pozitivne ali negativne modifikacije se lahko poveča relativni zdrs na začetku in koncu ubiranja, zato mora biti modifikacija čim manjša. Visoka vhodna hitrost ugodno vpliva na učinkovitost ubiranja. Rezultati izračunov bodo koristni pri konstruiranju in pri izbiri parametrov predlaganega zobnika.

Izračun učinkovitosti ubiranja v članku se nanaša na novi stožčasti evolventni zobnik. Proces ubiranja pri zobniku s poševnimi zobmi je podoben, zato so predstavljeni izračuni uporabni tudi pri določanju učinkovitosti ubiranja zob s poševnimi zobmi, če ne upoštevamo vpliva deformacij zob na obremenitve. Vpliv napak v montaži in izdelavi na učinkovitost zobniškega prenosa je bil zanemarjen.

V nadaljnjih raziskavah bi bilo treba upoštevati tudi deformacije zob in spremenljivo mazanje pri majhni nezveznosti ob spremembi smeri gibanja.

Ključne besede: stožčasti evolventni zobnik, zobniški prenosnik, tangencialna modifikacija, učinkovitost ubiranja, mikrosegmenti, izgube zaradi drsnega trenja

---

*Naslov avtorja za dopisovanje: Državni laboratorij za mehanske prenose, Univerza v Chongqingu, Kitajska, r7mars@163.com

Strojniški vestnik - Journal of Mechanical Engineering 63(2017)5, SI 47

Prejeto v recenzijo: 2017-01-13
Prejeto popravljeno: 2017-03-24
Odobreno za objavo: 2017-04-05

Mobilni roboti v stiku s človekom na osnovi strojnega vida – pregled

Miha Finžgar* – Primož Podržaj
Univerza v Ljubljani, Fakulteta za strojništvo, Slovenija

Mobilna robotika postaja vedno bolj razširjeno področje raziskav. Zmožnost gibanja mobilnih robotov v realnem okolju in opravljanja določenih nalog namreč omogočata uporabo teh robotov na številnih področjih. Posebna pozornost se namenja mobilnim robotom v stiku s človekom, tj. robotom, katerih opravljanje nalog je neposredno povezano s človekom. Eno izmed najbolj perspektivnih področij uporabe predstavlja zdravstvo. Z naraščajočim deležem starajočega se prebivalstva in kroničnih bolnikov se pojavlja potreba po nadzoru in spremljanju teh ljudi z namenom izboljšanja njihove kakovosti življenja ter zmanjšanja stroškov povezanih z zdravstvom. Uporaba mobilnih robotov, ki bi omogočali določeno zdravstveno oskrbo in nadzorovali zdravstveno stanje uporabnika, bi tako prinesla številne pozitivne posledice.

Z namenom seznanitve z različnimi rešitvami smo pregledali stanje obstoječih raziskav s področja mobilnih robotov v stiku s človekom na osnovi strojnega vida. Strojni vid predstavlja ključni mehanizem za uspešno interakcijo mobilnega robota z njegovim uporabnikom, saj omogoča prepoznavo človeka. Le-ta sestoji iz treh delov: zaznave, sledenja ter identifikacije človeka. V članku je predstavljen vsak izmed navedenih delov, pri čemer je posebna pozornost namenjena identifikaciji. Slednja je izredno pomembna pri uporabi mobilnih robotov v zdravstvu, kjer mora biti identiteta uporabnika znana. Poleg prepoznave človeka je za uspešno interakcijo pomembna tudi uporabnikova percepcija robotov. Percepcija ni odvisna samo od starosti uporabnika in njegovega zdravstvenega stanja, ampak zavisi od številnih drugih dejavnikov tako na strani človeka-uporabnika, kot na strani mobilnega robota.

V članku so predstavljene tudi različne izvedbe mobilnih robotov v stiku s človekom na osnovi strojnega vida, tako z vidika strojne kot programske opreme. Kvantitativno je ocenjena učinkovitost njihovega delovanja pri opravljanju začrtanih nalog. Rešitve s področja strojnega vida vključujejo uporabo digitalnih kamer, termokamer ali kombinacijo obeh sistemov. Pri uporabi digitalnih kamer gre lahko za eno konvencionalno digitalno kamero, stereo sistem ali za vsesmerno kamero. Prednost digitalnih kamer je robustnost na geometrijsko popačenje, slabost pa občutljivost na spremembe intenzitete svetlobe. Slednje se lahko izboljša z uporabo alternativnih barvnih prostorov. Glavna prednost termovizije je v tem, da ima človeško telo značilno temperaturno polje, ki omogoča enostavnejšo, od svetlobnih pogojev neodvisno, zaznavo človeka na zajetih slikah. Pomembni slabosti te metode sta nezmožnost identifikacije človeka in oteženo sledenje več osebam hkrati v primeru njihove medsebojne interakcije. Ne glede na izbiro vrste kamere, so najboljši rezultati prepoznave človeka doseženi z multimodalnimi sistemi, tj. sistemi, ki poleg vizualne informacije vključuje še druge signale, pridobljene npr. z laserskimi merilniki razdalje, mikrofoni, ultrazvočnimi zaznavali itd. Prednost multimodalnih sistemov je ta, da lahko kombinacija različnih informacij vpliva na zanesljivejšo prepoznavo človeka. Njihove slabosti pa so daljši računski čas (ob enaki računski moči), višja cena mobilnega robota ter možen zajem odvečnih informacij.

Članek na koncu vključuje pregled različnih aplikacij mobilnih robotov v stiku s človekom na osnovi strojnega vida skupaj z izzivi, ki jih prinaša njihova potencialna uporaba v aplikacijah povezanih z zdravstvom. Trenutni trend razvoja robotov gre v smer mehke robotike (ang. *soft robotics*), ki bo pomembno zastopano tudi v zdravstvenih aplikacijah. Mehki roboti so namreč sestavljeni iz mehkih materialov in zaznaval, ki omogočajo izvedbo zelo naravnega fizičnega stika med človekom in robotom.

V splošnem bosta, za razširjeno uporabo mobilnih robotov v stiku s človekom na osnovi strojnega vida v zdravstvenih aplikacijah, ključni uspešna interakcija med človekom in robotom ter zanesljivost izvedbe želenih nalog s strani mobilnega robota. Drugi konkretni izzivi vključujejo uporabo dodatnih zaznaval (npr. za zaznavo vonja, okusa in dotika), zagotavljanje nemotene mobilnosti mobilnih robotov, opravljanje nalog v realnem času, varnost zajetih podatkov o uporabniku idr.

Ključne besede: mobilni robot, strojni vid, prepoznava človeka, algoritmi obdelave slik, medicinske aplikacije, pregled

---

*Naslov avtorja za dopisovanje: Univerza v Ljubljani, Fakulteta za strojništvo, Aškerčeva 6, 1000 Ljubljana, Slovenija, miha.finzgar@fs.uni-lj.si

Information for Authors

All manuscripts must be in English. Pages should be numbered sequentially. The manuscript should be composed in accordance with the Article Template given above. The maximum length of contributions is 10 pages. Longer contributions will only be accepted if authors provide juastification in a cover letter. For full instructions see the Information for Authors section on the journal's website: http://en.sv-jme.eu .

SUBMISSION:

Submission to SV-JME is made with the implicit understanding that neither the manuscript nor the essence of its content has been published previously either in whole or in part and that it is not being considered for publication elsewhere. All the listed authors should have agreed on the content and the corresponding (submitting) author is responsible for having ensured that this agreement has been reached. The acceptance of an article is based entirely on its scientific merit, as judged by peer review. Scientific articles comprising simulations only will not be accepted for publication; simulations must be accompanied by experimental results carried out to confirm or deny the accuracy of the simulation. Every manuscript submitted to the SV-JME undergoes a peer-review process.

The authors are kindly invited to submit the paper through our web site: http://ojs.sv-jme.eu. The Author is able to track the submission through the editorial process - as well as participate in the copyediting and proofreading of submissions accepted for publication - by logging in, and using the username and password provided.

SUBMISSION CONTENT:

The typical submission material consists of:

- A **manuscript** (A PDF file, with title, all authors with affiliations, abstract, keywords, highlights, inserted figures and tables and references),
- Supplementary files:
  - a **manuscript** in a WORD file format
  - a **cover letter** (please see instructions for composing the cover letter)
  - a ZIP file containing **figures** in high resolution in one of the graphical formats (please see instructions for preparing the figure files)
  - possible **appendicies** (optional), cover materials, video materials, etc.

Incomplete or improperly prepared submissions will be rejected with explanatory comments provided. In this case we will kindly ask the authors to carefully read the Information for Authors and to resubmit their manuscripts taking into consideration our comments.

COVER LETTER INSTRUCTIONS:

Please add a **cover letter** stating the following information about the submitted paper:

1. Paper **title**, list of **authors** and their **affiliations**.
2. **Type of paper**: original scientific paper (1.01), review scientific paper (1.02) or short scientific paper (1.03).
3. A **declaration** that neither the manuscript nor the essence of its content has been published in whole or in part previously and that it is not being considered for publication elsewhere.
4. State the **value of the paper** or its practical, theoretical and scientific implications. What is new in the paper with respect to the state-of-the-art in the published papers? Do not repeat the content of your abstract for this purpose.
5. We kindly ask you to suggest at least two **reviewers** for your paper and give us their names, their full affiliation and contact information, and their scientific research interest. The suggested reviewers should have at least two relevant references (with an impact factor) to the scientific field concerned; they should not be from the same country as the authors and should have no close connection with the authors.

FORMAT OF THE MANUSCRIPT:

The manuscript should be composed in accordance with the Article Template. The manuscript should be written in the following format:

- A **Title** that adequately describes the content of the manuscript.
- A list of **Authors** and their **affiliations**.
- An **Abstract** that should not exceed 250 words. The Abstract should state the principal objectives and the scope of the investigation, as well as the methodology employed. It should summarize the results and state the principal conclusions.
- 4 to 6 significant **key words** should follow the abstract to aid indexing.
- 4 to 6 **highlights;** a short collection of bullet points that convey the core findings and provide readers with a quick textual overview of the article. These four to six bullet points should describe the essence of the research (e.g. results or conclusions) and highlight what is distinctive about it.
- An **Introduction** that should provide a review of recent literature and sufficient background information to allow the results of the article to be understood and evaluated.
- A **Methods** section detailing the theoretical or experimental methods used.
- An **Experimental section** that should provide details of the experimental set-up and the methods used to obtain the results.
- A **Results** section that should clearly and concisely present the data, using figures and tables where appropriate.
- A **Discussion** section that should describe the relationships and generalizations shown by the results and discuss the significance of the results, making comparisons with previously published work. (It may be appropriate to combine the Results and Discussion sections into a single section to improve clarity.)
- A **Conclusions** section that should present one or more conclusions drawn from the results and subsequent discussion and should not duplicate the Abstract.
- **Acknowledgement** (optional) of collaboration or preparation assistance may be included. Please note the source of funding for the research.
- **Nomenclature** (optional). Papers with many symbols should have a nomenclature that defines all symbols with units, inserted above the references. If one is used, it must contain all the symbols used in the manuscript and the definitions should not be repeated in the text. In all cases, identify the symbols used if they are not widely recognized in the profession. Define acronyms in the text, not in the nomenclature.
- **References** must be cited consecutively in the text using square brackets [1] and collected together in a reference list at the end of the manuscript.
- **Appendix(-icies)** if any.

SPECIAL NOTES

Units: The SI system of units for nomenclature, symbols and abbreviations should be followed closely. Symbols for physical quantities in the text should be written in italics (e.g. *v*, *T*, *n*, etc.). Symbols for units that consist of letters should be in plain text (e.g. $\mathrm{ms^{-1}}$, K, min, mm, etc.). Please also see: http://physics.nist.gov/cuu/pdf/sp811.pdf .

Abbreviations should be spelt out in full on first appearance followed by the abbreviation in parentheses, e.g. variable time geometry (VTG). The meaning of symbols and units belonging to symbols should be explained in each case or cited in a **nomenclature** section at the end of the manuscript before the References.

Figures (figures, graphs, illustrations digital images, photographs) must be cited in consecutive numerical order in the text and referred to in both the text and the captions as Fig. 1, Fig. 2, etc. Figures should be prepared without borders and on white grounding and should be sent separately in their original formats. If a figure is composed of several parts, please mark each part with a), b), c), etc. and provide an explanation for each part in Figure caption. The caption should be self-explanatory. Letters and numbers should be readable (Arial or Times New Roman, min 6 pt with equal sizes and fonts in all figures). Graphics (submitted as supplementary files) may be exported in resolution good enough for printing (min. 300 dpi) in any common format, e.g. TIFF, BMP or JPG, PDF and should be named Fig1.jpg, Fig2.tif, etc. However, graphs and line drawings should be prepared as vector images, e.g. CDR, AI. Multi-curve graphs should have individual curves marked with a symbol or otherwise provide distinguishing differences using, for example, different thicknesses or dashing.

Tables should carry separate titles and must be numbered in consecutive numerical order in the text and referred to in both the text and the captions as Table 1, Table 2, etc. In addition to the physical quantities, such as *t* (in italics), the units [s] (normal text) should be added in square brackets. Tables should not duplicate data found elsewhere in the manuscript. Tables should be prepared using a table editor and not inserted as a graphic.

REFERENCES:

A reference list must be included using the following information as a guide. Only cited text references are to be included. Each reference is to be referred to in the text by a number enclosed in a square bracket (i.e. [3] or [2] to [4] for more references; do not combine more than 3 references, explain each). No reference to the author is necessary.

References must be numbered and ordered according to where they are first mentioned in the paper, not alphabetically. All references must be complete and accurate. Please add DOI code when available. Examples follow.

Journal Papers:

Surname 1, Initials, Surname 2, Initials (year). Title. Journal, volume, number, pages, DOI code.

[1] Hackenschmidt, R., Alber-Laukant, B., Rieg, F. (2010). Simulating nonlinear materials under centrifugal forces by using intelligent cross-linked simulations. *Strojniški vestnik - Journal of Mechanical Engineering,* vol. 57, no. 7-8, p. 531-538, DOI:10.5545/sv-jme.2011.013.

Journal titles should not be abbreviated. Note that journal title is set in italics.

Books:

Surname 1, Initials, Surname 2, Initials (year). Title. Publisher, place of publication.

[2] Groover, M.P. (2007). *Fundamentals of Modern Manufacturing*. John Wiley & Sons, Hoboken.

Note that the title of the book is italicized.

Chapters in Books:

Surname 1, Initials, Surname 2, Initials (year). Chapter title. Editor(s) of book, book title. Publisher, place of publication, pages.

[3] Carbone, G., Ceccarelli, M. (2005). Legged robotic systems. Kordić, V., Lazinica, A., Merdan, M. (Eds.), Cutting Edge Robotics. Pro literatur Verlag, Mammendorf, p. 553-576.

Proceedings Papers:

Surname 1, Initials, Surname 2, Initials (year). Paper title. Proceedings title, pages.

[4] Štefanić, N., Martinčević-Mikić, S., Tošanović, N. (2009). Applied lean system in process industry. *MOTSP Conference Proceedings*, p. 422-427.

Standards:

Standard-Code (year). Title. Organisation. Place.

[5] ISO/DIS 16000-6.2:2002. *Indoor Air – Part 6: Determination of Volatile Organic Compounds in Indoor and Chamber Air by Active Sampling on TENAX TA Sorbent, Thermal Desorption and Gas Chromatography using MSD/FID.* International Organization for Standardization. Geneva.

WWW pages:

Surname, Initials or Company name. Title, from http://address, date of access.

[6] Rockwell Automation. Arena, from *http://www.arenasimulation.com,* accessed on 2009-09-07.

EXTENDED ABSTRACT:

When the paper is accepted for publishing, the authors will be requested to send an **extended abstract** (approx. one A4 page or 3500 to 4000 characters). The instruction for composing the extended abstract are published on-line: http://www.sv-jme.eu/information-for-authors/ .

COPYRIGHT:

Authors submitting a manuscript do so on the understanding that the work has not been published before, is not being considered for publication elsewhere and has been read and approved by all authors. The submission of the manuscript by the authors means that the authors automatically agree to transfer copyright to SV-JME when the manuscript is accepted for publication. All accepted manuscripts must be accompanied by a Copyright Transfer Agreement, which should be sent to the editor. The work should be original work by the authors and not be published elsewhere in any language without the written consent of the publisher. The proof will be sent to the author showing the final layout of the article. Proof correction must be minimal and executed quickly. Thus it is essential that manuscripts are accurate when submitted. Authors can track the status of their accepted articles on http://en.sv-jme.eu/.

PUBLICATION FEE:

Authors will be asked to pay a publication fee for each article prior to the article appearing in the journal. However, this fee only needs to be paid after the article has been accepted for publishing. The fee is 240.00 EUR (for articles with maximum of 6 pages), 300.00 EUR (for articles with maximum of 10 pages), plus 30.00 EUR for each additional page. The additional cost for a color page is 90.00 EUR. These fees do not include tax.

Strojniški vestnik -Journal of Mechanical Engineering
Aškerčeva 6, 1000 Ljubljana, Slovenia,
e-mail: info@sv-jme.eu

ISSN 0039-2480

http://www.sv-jme.eu

Contents

Papers